NATIONAL AND KAPODISTRIAN UNIVERSITY OF ATHENS

MASTER'S THESIS

Estimation and mechanistic interpretation of wind-wave interactions in *in situ* and satellite altimetry data in the Southern New England Region.

Author:
Panagiotis Mitsopoulos

Supervisor:
Sarantis Sofianos
Advisory Committe:
Helena Floca, Malaquias Peña

A thesis submitted in fulfillment of the requirements
for the degree of Master of Science

in the

Oceanography and Management of the Marine Environment MSc
Ocean Physics And Modelling Group

December 11, 2020

Declaration of Authorship

I, Panagiotis Mitsopoulos, declare that this thesis titled, "Estimation and mechanistic interpretation of wind-wave interactions in *in situ* and satellite altimetry data in the Southern New England Region." and the work presented in it are my own. I confirm that:

- This work was done wholly or mainly while in candidature for a research degree at this University.

- Where any part of this thesis has previously been submitted for a degree or any other qualification at this University or any other institution, this has been clearly stated.

- Where I have consulted the published work of others, this is always clearly attributed.

- Where I have quoted from the work of others, the source is always given. With the exception of such quotations, this thesis is entirely my own work.

- I have acknowledged all main sources of help.

- Where the thesis is based on work done by myself jointly with others, I have made clear exactly what was done by others and what I have contributed myself.

Signed:

_____

Date:

_____

NATIONAL AND KAPODISTRIAN UNIVERSITY OF ATHENS

Abstract

Sarantis Sofianos
Oceanography and Management of the Marine Environment MSc

Master of Science

Estimation and mechanistic interpretation of wind-wave interactions in *in situ* and satellite altimetry data in the Southern New England Region.

by Panagiotis Mitsopoulos

Accurate estimation of wind and wave conditions is an essential information resource for ship routing, coastal engineering, and several other coastal activities. The developing offshore wind energy industry needs these estimations for prospecting and ensuring the optimal siting of wind farms. Wind farms' construction, operation, and decommission need real-time monitoring of wind and waves for decision making. Additionally, special attention to extremes and transient events must be paid for the aforementioned applications since they have the most considerable impact and must be well captured in numerical models. While a sprawl of data from various remote sensing capabilities, including the next generation of satellite altimeter data, is growing, their use is more effective when combined with traditional, longer-record, in situ observations from buoys, which serve as ground truth reference. This study focuses on the independent use of the two data sources and properly combining them so that the final analysis is physically consistent. Statistical analysis and optimal interpolation, merging multiple sensor's data, are performed to improve the offshore marine conditions' estimations and to identify dominant mesoscale and local mechanisms that contribute to their variability. The scope of this research is focused on the observations taken on the Southern New England region in the United States, where new offshore wind energy developments are taking place.

Main research results:

- An updated wind and wave climatology of the domain with a focus on climate variability in multiple timescales (diurnal, seasonal, interannual).

- The directional distribution of near-surface wind and wave height.

- The wind speed and significant wave height relationship based on theoretical formulae and ocean waves classification based on their growth rate.

- The wind speed probability density functions which provide the best fit to the wind speed distribution.

- A case study of extreme events.

- The validation of satellite altimeter with in situ observations in the Southern New England region.

- Maps of interpolated wind speed and significant wave height fields using observations from multiple satellite altimeters.

ΕΘΝΙΚΟ ΚΑΙ ΚΑΠΟΔΙΣΤΡΙΑΚΟ ΠΑΝΕΠΙΣΤΗΜΙΟ ΑΘΗΝΩΝ

Περίληψη

Εκτίμηση και ερμηνεία των φυσικών μηχανισμών αλληλεπίδρασης θάλασσας-ατμόσφαιρας, μέσω δεδομένων ανέμου και ύψους κύματος, από πλωτούς σταθμούς μέτρησης και δορυφόρους νέας γενιάς στην περιοχή της Νότιας Νέας Αγγλίας.

από τον Παναγιώτη Μητσόπουλο

Η ακριβής εκτίμηση των συνθηκών ανέμου και κύματος αποτελεί απαραίτητη πληροφορία για την πορεία των πλοίων, την παράκτια μηχανική και πολλών ακόμη δραστηριοτήτων που λαμβάνουν χώρα στη παράκτια ζώνη. Η αναπτυσσόμενη βιομηχανία της υπεράκτιας αιολικής ενέργειας χρειάζεται αυτές τις εκτιμήσεις για την έρευνα και εξασφάλιση της βέλτιστης τοποθεσίας των αιολικών πάρκων. Η παρακολούθηση σε πραγματικό χρόνο του ανέμου και του κύματος για την λήψη αποφάσεων είναι απαραίτητη κατά τις περιόδους κατασκευής, λειτουργίας αλλά και απόσυρσης των αιολικών πάρκων. Επιπροσθέτως, ιδιαίτερη σημασία πρέπει να δίδεται και στα ακραία και παροδικά φαινόμενα καθώς έχουν τις σημαντικότερες επιπτώσεις και πρέπει να αποτυπώνονται ρεαλιστικά από τα αριθμητικά μοντέλα. Καθώς η διαθεσιμότητα των δεδομένων τηλεπισκόπισης, συμπεριλαμβανωμένων και των δορυφόρων αλτιμετρίας νέας γενιάς, ολοένα και αναπτύσσεται, η χρήση τους είναι πιο αποτελεσματική όταν συνδυάζεται με επιτόπιες παρατηρήσεις από τους πιο παραδοσιακούς, πλωτούς σταθμούς μέτρησης, οι οποίοι συλλέγουν δεδομένα για μεγάλο χρονικό διάστημα και θεωρούνται ως παρατηρήσεις αναφοράς. Η συγκεκριμένη εργασία εστιάζεται στην ανεξάρτητη ανάλυση των δύο πηγών δεδομένων αλλά και στον κατάλληλο συνδυασμό τους ώστε τα τελικά αποτελέσματα να εμφανίζουν συνέπεια. Η στατιστική ανάλυση επιτόπιων παρατηρήσεων αλλά και η εφαρμογή σχήματος βέλτιστης παρεμβολής για την συγχώνευση δεδομένων από διαφορετικούς δορυφόρους, βοηθούν στην βελτίωση της εκτίμησης των υπεράκτιων θαλάσσιων συνθηκών αλλά και στην αναγνώριση των κυρίαρχων τοπικών μηχανισμών και μέσης κλίμακας που συμβάλλουν στην μεταβλητότητα τους. Η μελέτη εστιάζεται στην περιοχή της Νότιας Νέας Αγγλίας των Ηνωμένων Πολιτειών της Αμερικής, στην οποία λαμβάνει χώρα η ανάπτυξη της υπεράκτιας αιολικής ενέργειας.

Acknowledgements

Looking back at the year that I spent working on my thesis, I would like to thank the people who contributed to its realization, both academically and personally.

First and foremost, my deepest gratitude goes to my supervisor, Professor Sarantis Sofianos, to support my willingness to work on this thesis and his guidance, encouragement, and thoughtful comments.

I would also like to express my great appreciation to Professor Malaquias Peña. His experience and expertise were critical from the foundation of this thesis to its completion. It was a pleasure to collaborate and share my ideas with him during the past year.

My sincere appreciation goes to Professor Helena Floca. She was always present and helpful when I needed her support as a member of the advisory committee and one of the Oceanography and Management of the Marine Environment faculty members.

I cannot omit to thank John Karagiorgos and all members of the Ocean Physics and Modelling Group, of which I spent one memorable year as a member. They provided me with insight into technical matters, were there to discuss, encouraged me, and assisted me as a friend and colleague.

I am also thankful to Randolph Bucciarelli and the CDIP research team for their cooperation and effort to provide me with valuable information and data. Stylianos Flampouris of NOAA-NCEP-EMC was kind enough to share his ocean waves' expertise and correspond to my inquiries.

On a personal level, I would like to express my gratitude to my parents for their support and belief in my aspirations. Last but not least, a heartfelt thank you goes to Viky K. for her patience, understanding and sharing a challenging but rewarding year.

Contents

List of Figures

List of Tables

List of Abbreviations

SWH	**S**ignificant **W**ave **H**eight
WS	**W**ind **S**peed
SSH	**S**ea **S**urface **H**eight
SST	**S**ea **S**urface **T**emperature
SNE	**S**outhern **N**ew **E**ngland
NDBC	**N**ational **D**ata **B**uoy **C**enter
CDIP	**C**oastal **D**ata **I**nformation **P**rogram
OERG	**O**cean **E**ngineering **R**esearch **G**roup
IOD	**I**ntegrative **O**ceanography **D**ivision
SIO	**S**cripps **I**nstitution of **O**ceanography
LISICOS	**L**ong **I**sland **S**ound **I**ntegrated **C**oastal **O**bserving **S**ystem
UConn	**U**niversity of **Conn**ecticut
NOAA	**N**ational **O**ceanic and **A**tmospheric **A**dministration
THREDDS	**TH**ematic **R**eal-time **E**nvironmental **D**istributed **D**ata **S**ervices
TDS	**T**hredds **D**ata **S**erver
NetCDF	**Net**work **C**ommon **D**ata **F**orm
BOEM	**B**ureau of **O**cean **E**nergy **M**anagement
CNES	**C**entre **N**ational d'**E**tudes **S**patiales
ISRO	**I**ndian **S**pace and **R**esearch **O**rganization
NASA	**N**ational **A**eronautics and **S**pace **A**dministration
EUMETSAT	**EU**ropean Organization for the exploitation of **MET**eorological **SAT**ellites
ESA	**E**uropean **S**pace **A**gency
LRM	**L**ow **R**esolution **M**ode
PLRM	**P**seudo **L**ow **R**esolution **M**ode
SAR	**S**ynthetic **A**perture **R**adar
SARIn	**S**ynthetic **A**perture **R**adar **Interferometry**
AMR	**A**dvanced **M**icrowave **R**adiometer
LRA	**L**aser **R**eflector **A**rray
GPSP	**G**lobal **P**ositioning **S**ystem **P**ayload
NRT	**N**ear **R**eal **T**ime
GDR	**G**eophysical **D**ata **R**ecords
OGDR	**O**perational **G**eophysical **D**ata **R**ecords
IGDR	**I**nterim **G**eophysical **D**ata **R**ecords
STC	**S**hort **T**ime **C**ritical
NTC	**N**on **T**ime **C**ritical
GOP	**G**eophysical **O**cean **P**roduct
CUT	**C**ryosat **U**ser **T**ool
WPC	**W**eather **P**rediction **C**enter

Chapter 1

Introduction

1.1 Objective

This study's motivation originates from the wealth of offshore wind developments in the United States (US) East Coast during recent years. The Bureau of Offshore Energy Management (BOEM) has already leased several areas between the coastal and continental shelf limits that correspond to multiple projects to construct and manage offshore wind farms. BOEM has recently released a guideline addressing the oceanographic and meteorological conditions that need to be characterized to support the offshore wind farms' infrastructure development [22]. Wind and wave conditions are two of the leading environmental factors connected to offshore wind. Their accurate estimation is crucial for the design, the operation, and the energy yield of an offshore wind facility.

There is a need for long-term and reliable data records to estimate the wind and wave conditions. Numerical models and observations support offshore wind energy with the characterization of these conditions. There are two primary objectives of good quality observations. On the one hand, they are an independent source of knowledge that we use to study the environmental conditions and climate. On the other hand, observations are used to enhance the robustness of numerical models through data assimilation. This study focuses on the Southern New England (SNE) wind and wave regime's characterization using in situ observations from buoy stations that are moored in the domain and from satellite altimeters. We take advantage of the National Data Buoy Center (NDBC) and Coastal Data Information Program (CDIP) extended network of stations for the in situ data. These observations are closer to the ground truth, but the sensors' measurements onboard buoys contain inherent sources of errors. The advantage of in situ stations is that they provide a long-term, reliable, and quality controlled time-series record. Therefore, they are suitable for the accurate estimation of the normal conditions in our area of interest. However, they represent measurements in point locations; hence, there are spatial gaps in our estimates. Observations from multiple satellite altimeters can partly fill these spatial gaps; thus, first, we aim to compare and validate altimeters with in situ data and then provide maps of the wind and sea state primary measures. The satellite altimeters' disadvantage is the low temporal resolution, as it depends on each satellite's cycle, the period that elapses until it passes again over the same region.

1.2 Study Area

The area of interest is located in the western part of the North Atlantic ocean or the East Coast of the continental United States. The region we focus on is geographically defined by the coastal Southern New England states of Connecticut (CT), Rhode Island (RI), Massachusetts (MA) on the east, and the New York/New Jersey bight, including Long Island on the west.
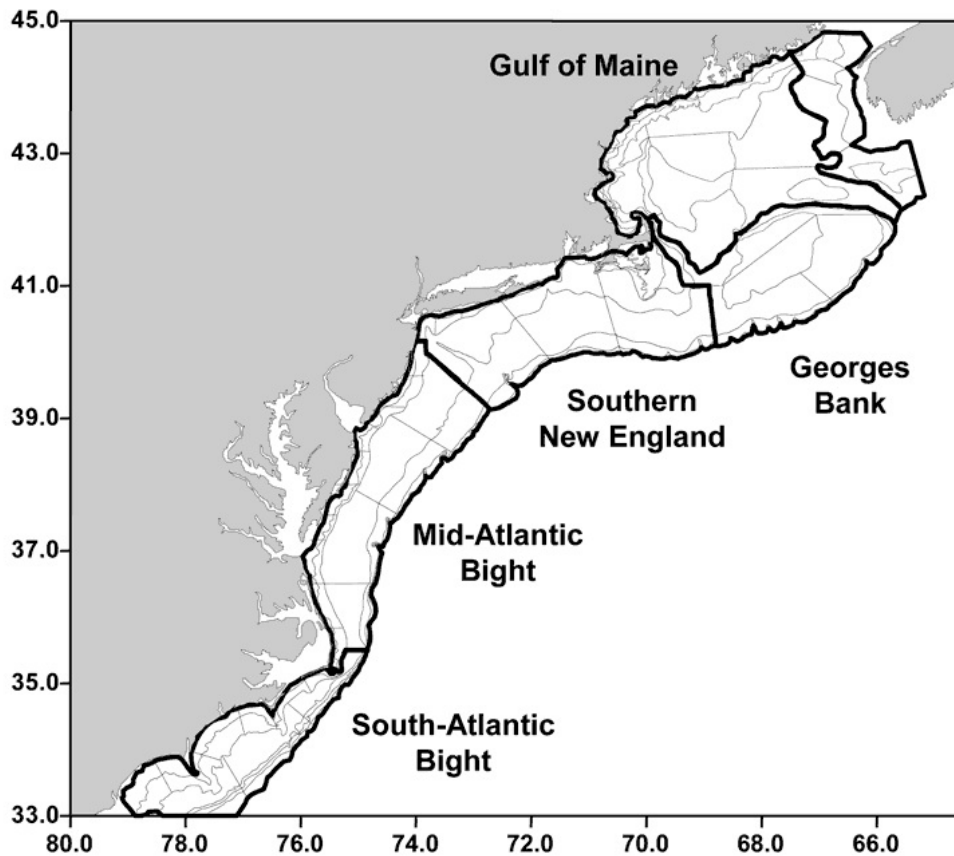
FIGURE 1.1: US coastal regions of the Northwest Atlantic.

Specifically, the domain of interest is limited between 74°W and 69°W longitude and 39°N and 42°N latitude. Besides, it extends about 200 kilometers offshore, on the limits of the US continental shelf. The whole domain is referenced herein as Southern New England (SNE) for reader's convenience, even though it contains parts of New York and New Jersey, and it is shown in Figure 1.1.

SNE is also the birthplace of offshore wind in the United States, with Block Island wind farm being the first constructed and operating in US coastal waters [73]. This region is strongly connected with offshore wind energy as many promising projects currently exist, and multiple areas shown in Figure 1.2 have already been leased. Similar developments will also occur in the region's central and western parts soon, as BOEM has also recommended several lease areas.

The strong presence and increased frequency of extratropical storms also characterize SNE's coastal zone [101]. These low-pressure systems are noticeable primarily during the fall, winter, and spring seasons. They develop in Southern latitudes, and the maximum of their intensity is often attained in the New England region. They are called Nor'easters due to the coastal wind's direction during their passing. Their impact on the coastal zone is significant as they cause high winds, extreme waves, storm surges, and coastal flooding. The maximum Wind Speed (WS) values during Nor'easters do not approach those during the passing of hurricanes. However, they are frequent over New England, and the coupling of high waves and long duration may have a minimal to a catastrophic impact on the whole region [23]. Coastal fronts are also a common feature of late fall, early winter New England weather. Their genesis and formation close to the coast due to land-ocean differential heating or inland due to differential heating connected with the uplifting of moist air when approaching the Appalachian mountains is documented in detail in the literature [76].
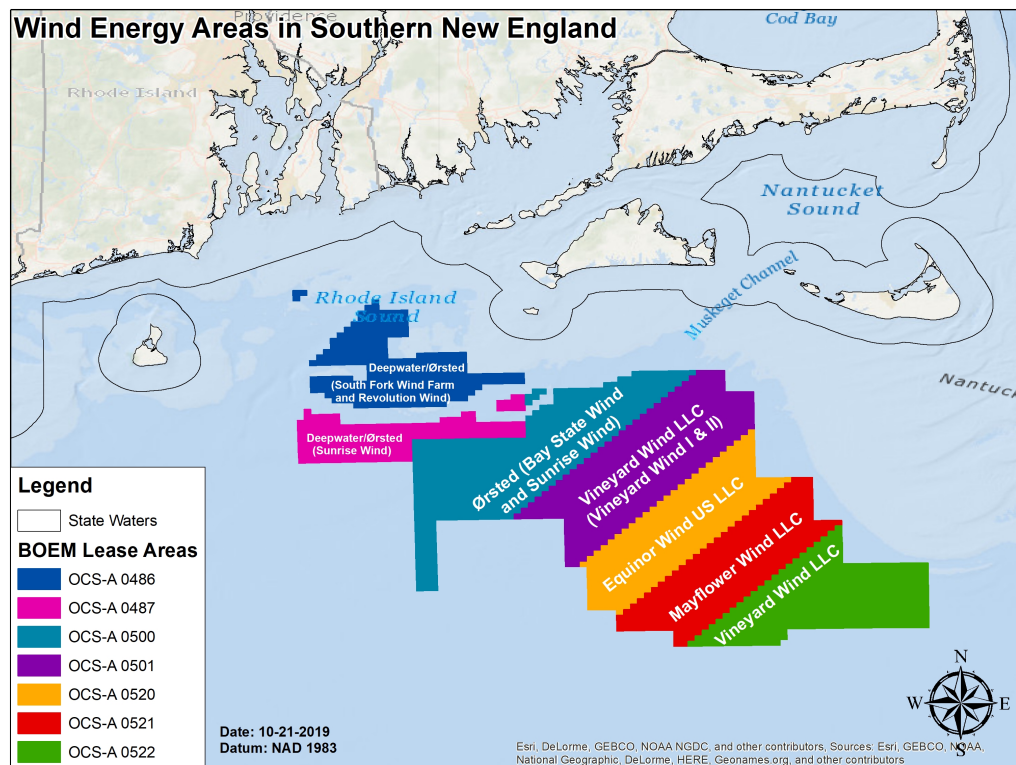
FIGURE 1.2: BOEM Offshore Wind lease areas in SNE. Source: RI Department of Environmental Management (DEM)

1.3 Outline

Chapter 2 provides the theoretical background of this study. First of all, we define the wave parameters reported from in situ and remote sensing observations. One of the common parameters often used to characterize the sea state is the Significant Wave Height (SWH). We examine how it is connected with the directional wave spectra and how it is derived from it. One of the several ways to take advantage of the directional spectrum of waves leads us to review the different ways to separate the sea states, a process called spectral decomposition. An alternative way to empirically separate the sea states based on their growth stage is by considering their wave age, which connects the wave speed of propagation with the WS. Besides, a literature review of the bulk formulas used historically to connect the WS, and SWH is provided, examining their limitations. Bulk formulas are also used to estimate the waves' interaction with the wind over the ocean. The unavailability of multiple parameters required for the accurate description of the boundary layer's stability is often a limitation. Therefore, due to these restrictions, we often use the wind speed profile over the ocean and the governing laws of air-sea interaction with assumptions of the conditions near the sea surface. The wind speed probability density functions (PDFs) are essential to estimate the mean wind power density close to the offshore wind planned area. Studies connected with offshore wind research include estimating the PDF parameters and searching for innovative ways to select the optimal PDF to characterize the wind speed distribution. We provide the four distributions and their theoretical PDFs with the best fit for the SNE region's data. Finally, data from satellite altimeters are measured with entirely different methodologies than those used for in situ observations. They also represent different spatial and temporal

scales of the wind and wave conditions. Therefore, the principles of satellite altimetry are described to explain these differences.

Chapter 3 includes a detailed description of the methodologies used to derive our results. An integral part of all the studies that include observations is data preprocessing. It consists of the collection, organization, and description of the various datasets used. The accuracy of the measurements and the detection of error sources are also essential to filter out erroneous data. All the above are provided both for the buoy and the satellite altimeter observations. A spatiotemporal collocation methodology is required to validate altimeter observations' consistency with respect to in situ, which are considered the ground truth reference. A description of the limitations of such comparisons is also provided. After validating the satellite altimeter observations, variogram modeling is used to describe the observations' spatial correlation. This process is critical for interpolation to create maps of the WS and SWH spatial variability and estimate the predictions' uncertainty.

Chapter 4 contains all the results. The first section is about the wind and wave climatology of the SNE based on buoy data. We examine different temporal scales of variability, including the diurnal, seasonal, and interannual, for each buoy with an available long-term record. The goal is to define the normal wind and wave conditions in SNE. The wind and wave directional characteristics are also of high importance. Hence, we provide and visualize the directional distribution of WS and SWH. We also emphasize the benefits of considering the directional wave spectra for a detailed description of the wave climate. The WS and SWH relationships are estimated using polynomial regression analysis. The differences between these relationships with respect to wind direction are also examined for each location. The classification of waves is performed based on their inverse wave age. An extreme event is analyzed and described as a case study. The parameters of WS PDFs that best fit the data from individual stations are estimated and evaluated. Validation of the data from multiple satellite altimeter missions is performed using buoy observations as a reference. An evaluation of their performance is also included. Satellite altimeter data are interpolated for recent winter and summer seasons to estimate the wind and wave spatial distribution in the SNE region. The limitations of this process are discussed. The impact of including data from multiple satellite altimeters on the estimation errors is also assessed.

Finally, Chapter 5 summarizes the results, including the scientific questions raised from this study to motivate future related research.

Chapter 2

Theoretical Background

2.1 Significant Wave Height and Wave Spectra

Historically, the study of wave growth and the interest in its prediction have their origins in the Second World War when it was critical for landing operations. Munk [69] classified ocean waves according to their propagation period and documented the need for further comprehension of the wave spectrum. The band of the range of ocean waves that we are focusing on in this study is the ordinary gravity waves, as shown in Figure 2.1. Wave characteristics that describe what we call sea state were first observed visually and empirically defined. Since then, a better understanding of the generation of waves and the need for reliable and continuous observations led to what we perceive as the SWH and wave spectrum nowadays.
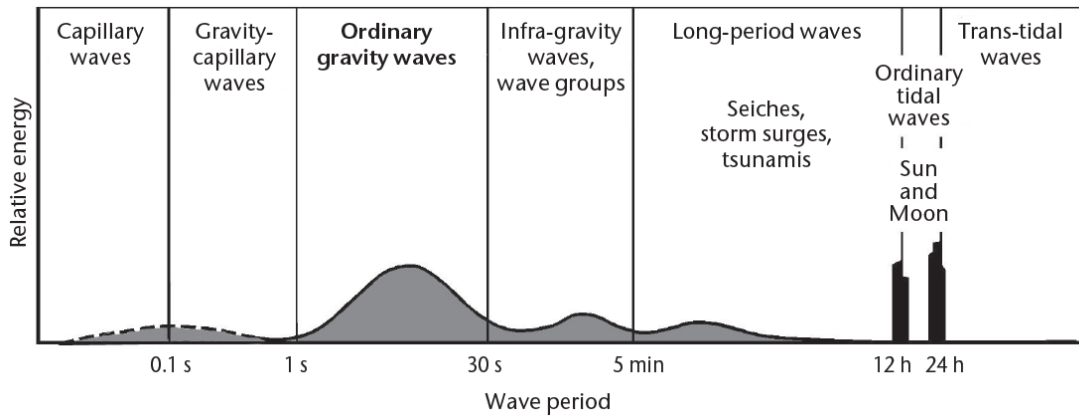
FIGURE 2.1: The classification of ocean waves depending on their period according to Munk [69]. Reprinted from: [77]

First, we need to define the linear waves' fundamental parameters. The wavelength λ is the horizontal distance between two consecutive crests of a wave in meters, and it is connected with the wavenumber k, the number of crests per unit distance:

$$k = \frac{2\pi}{\lambda} \tag{2.1}$$

Wave frequency f is equal to the number of crests that pass from a point every second. Wave period T is the time interval in seconds between the passage of successive crests from a fixed location. They are both related with the angular frequency ω in radians per second:

$$\omega = \frac{2\pi}{T} = 2\pi f \tag{2.2}$$

The wavenumber and wave frequency are connected with the dispersion relation, which characterizes wave propagation variation. The dispersion relation of ordinary gravity waves for specific depth h is given by:

$$\omega^2 = gk \tanh kh \tag{2.3}$$

Other important parameters, especially for navigation and offshore installations, include the amplitude α, which is the maximum displacement from the mean or zero sea level, and the wave height H, which is the vertical distance of the successive troughs and crests, both measured in meters. Finally, we need to know the wave direction in degrees from which the waves propagate to characterize the sea state.

The definition of random ocean waves rests on the assumption that they are a superposition of an infinite number of components. Each wave component is characterized by a unique combination of frequency and propagation direction. The vertical displacement of waves in 2-dimensional space and time is given by the sum of the components' surface elevation [38]:

$$\eta\left(x,y,t\right) = \sum_{n=1}^{\infty} \alpha_n \cos\left(k_n x \cos\theta_n + k_n y \sin\theta_n - 2\pi f_n t + \epsilon_n\right) \tag{2.4}$$

Each wave component has a different phase angle ϵ_n between 0 and 2π. The sum of the squared amplitudes of the wave components has a unique value:

$$\sum_{f}^{f+df} \sum_{\theta}^{\theta+d\theta} \frac{1}{2}\alpha_n^2 = S\left(f,\theta\right) df d\theta \tag{2.5}$$

The function $S\left(f,\theta\right)$ is the directional wave spectrum, and it represents the wave energy distribution with respect to the different frequencies and directions of ocean waves because the squared amplitudes are also present at the wave energy equation:

$$E = \frac{\rho_w g H^2}{8} = \frac{\rho_w g \alpha^2}{2} \tag{2.6}$$

Where p_w is the water density and g is the gravitational acceleration constant. Therefore, a transformation of $S(f,\theta)$ to $p_w g S(f,\theta)$ is necessary first to be consistent with the energy spectrum term. The total wave energy is represented by m_0 which is the zeroth-moment of the spectrum [5], and it is calculated by the integral of the $S(f,\theta)$ function in all frequencies and directions:

$$m_0 = \int_0^{\infty} \int_0^{2\pi} S(f,\theta) df d\theta \tag{2.7}$$

This integral is by definition equal to the surface elevation variance $\overline{\eta^2}$. Thus, wave elevation variance is a more accurate term than wave energy. SWH is defined as four times the Root-Mean-Square (RMS) of the elevation variance, and it is denoted as H_s or H_{m0}.

$$H_s = 4\sqrt{m_0} \tag{2.8}$$

When directional information is unavailable, we can obtain the wave spectrum as a function only of the frequencies. It becomes the frequency spectrum, an example of which is shown in Figure 2.2 using buoy observations. The infinite number of wave frequencies are represented on the x-axis. In reality, sensors onboard buoys divide the whole spectrum into frequency bands with an $f+df$ size. NDBC uses frequency bands of 0.01 Hz size with a cut-in frequency of 0.03 Hz and a cut-off frequency of 0.4 Hz. On the other hand, CDIP uses

narrower frequency bands of 0.005 Hz for a more extended spectrum with a cut-in frequency of 0.025 Hz and a cut-off frequency of 0.58 Hz. The elevation variances or the wave energies are plotted on the y-axis in m^2s or m^2/Hz.
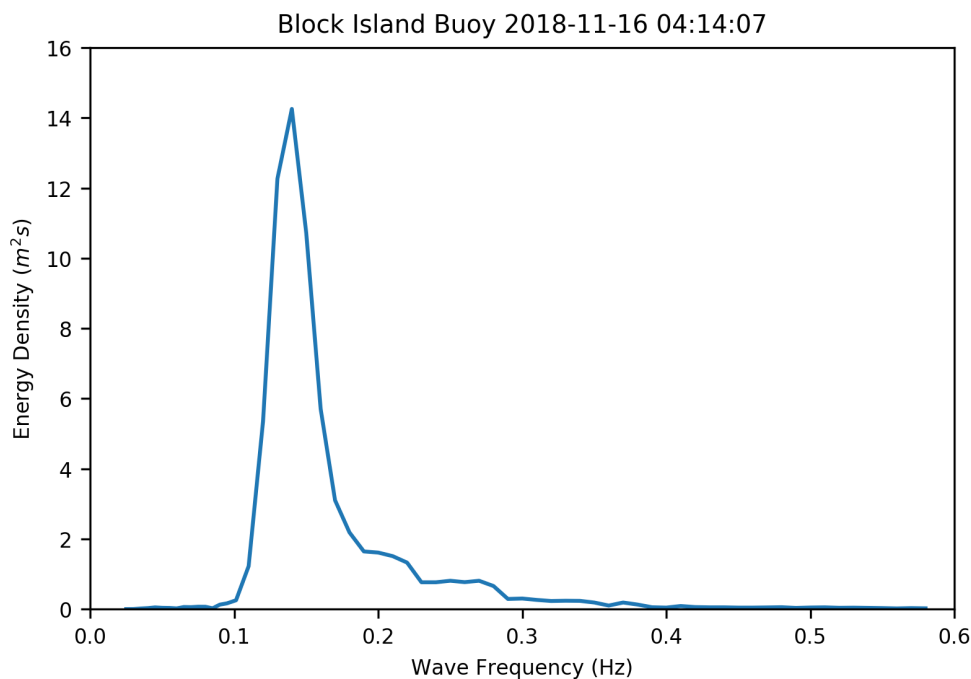
FIGURE 2.2: An example of a wave frequency spectrum. Data presented were reported from Block Island buoy 44097 on October 27 2018.

From the frequency spectrum, we can derive two primary parameters for our study, the SWH and the peak or dominant period T_p. The integral of the spectrum that represents the volume of the area under its continuous curve in Figure 2.2 is equal to the zeroth-moment of the spectrum m_0, and it is the representative value of the total wave energy as defined in 2.7. Therefore, SWH is expressed as four times the square root of this integral. From the frequency spectrum, we can also derive the peak frequency f_p, which is the wave frequency of the spectrum's peak band. The wave dominant period T_p corresponds to the peak frequency band.

To estimate SWH and T_p from the wave spectrum accurately, observations are assumed to represent statistically stationary random processes. The aim is to prevent scattering of the observation values; hence, we need a relatively large wave measurement record [77]. To satisfy both conditions, NDBC and CDIP stations record raw 1 Hz observations for 20 minutes (see 3.1.1).

The directional wave spectrum $S(f,\theta)$ is the distribution of the elevation variance or the wave energy both in the frequency domain and the wave components' direction. An example of the directional wave spectrum from buoy observations is shown in 2.3 and the wave energy density is reported in m^2s/deg or m^2s/rad.

Except for the SWH and T_p, we also need information relative to the ocean waves' direction to obtain a complete picture of the sea state. Except for the surface elevation, buoys contain directional wave sensors measuring the slope vector, and they are included in their raw time series. These measuring systems are called heave pitch and roll, and the slope time series are measured in the east-west, and north-south direction using buoy azimuth [92].

The directional wave spectrum is also expressed as:

$$S(f,\theta) = S(f)D(f,\theta) \tag{2.9}$$

where $D(f,\theta)$ is the directional spreading function:

$$\int_{-\pi}^{\pi} D(f,\theta)d\theta = 1 \tag{2.10}$$

D(f,θ) describes how the wave energy density is spread in all directions. Longuet-Higgins [61], estimated the wave spectrum using the Fourier series methodology and proved that the first four coefficients are needed to describe the spectrum, including its directional parameters. The four Fourier coefficients are calculated by applying cross-spectral analysis to the wave elevation and the buoys' slope time series. This process is extensively described in [20, 27, 28, 56].
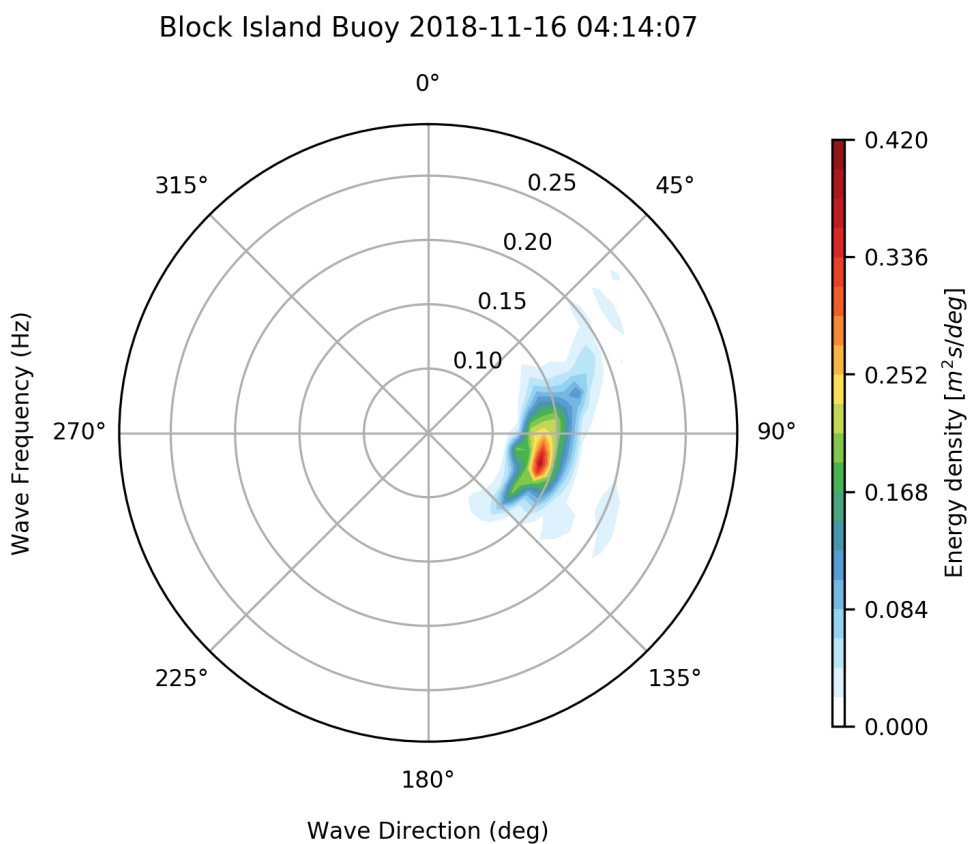
FIGURE 2.3: An example of a wave directional spectrum. Data presented were reported from Block Island buoy 44097 for October 27 2018.

The challenge is to reconstruct the directional spreading function from the estimated Fourier coefficients and create the directional spectra. It is worth mentioning that NDBC buoys, using the Datawell Hippy 40 sensor, measure and then disseminate the frequency spectrum and the four Fourier coefficient time series [92]. Still, the final two-dimensional spectra are not provided. CDIP provides only recent directional spectra online. There are several methods to reconstruct the two-dimensional, directional spectra. The Maximum Entropy Method (MEM) [62], is considered the most reliable [5]. CDIP also uses this method to reconstruct the directional spectra. Its disadvantage is that often the spectrum's shape contains artificial double-peaks. An extended discussion of the various methods to reconstruct the directional spectrum is available in [28, 39, 106].

2.2 Wave Age and Spectral Decomposition

In the previous section, we discussed the importance of the directional wave spectra to describe the ocean wave conditions. We also emphasized that the waves contributing to the wave spectrum have various frequencies, directions, heights, and periods. This leads us to study waves according to their unique characteristics and influence on the wave climate.

Waves can be classified according to their growth status. Local waves that owe their development to the increasing momentum input from the wind are called wind waves or wind sea. When the wind speed is reduced, and the wind's relative direction with the waves is increased over 30 degrees, or when remotely-generated waves due to a distant storm arrive, they are called swell [77]. Wind waves are strongly correlated with the wind, and they have a notable presence during extreme events, in enclosed basins, and coastal regions. An empirical method often used is to classify waves as wind sea when their dominant period has a duration of fewer than 10 seconds. In contrast, swells are not coupled with the wind, and they do not owe their development to a local wind momentum input. Besides, swell waves are different visually, as they appear as more organized groups of waves with smoother crests. In this study, we will focus on two methods of ocean wave classification.

The first method is based on ocean waves' growth using the inverse wave age criterion [45]. Wave age $c_p/U_{10}\cos\theta_d$ represents the wind's potential to transfer energy to the waves [108]. c_p is the wave phase speed at the peak of their spectrum and it is equal to λ_p/T_p or ω_p/k_p. Once wind-waves are generated, the wind is faster than the waves. As the energy is provided to the wind waves, their celerity increases until they reach the wind-wave equilibrium, at which the sea is considered mature or fully developed:

$$\frac{c_p}{U_{10}\cos\theta_d} = 1.2 \tag{2.11}$$

u_{10} is the wind speed at 10 meters height, which is discussed in the next Section 2.3 and θ_d is the relative angle between the wind direction and the mean wave direction. If we combine c_p with the dispersion relation for deep water waves $\omega^2 = gk$ and 2.2, the result is a relationship which connects the peak propagation speed with the dominant period [45]:

$$c_p = \frac{gT_p}{2\pi} \tag{2.12}$$

The inverse wave criterion is used to classify waves from buoy time series as in similar studies [33, 45]. We classify wind waves according to the following condition:

$$\frac{U_{10}\cos\theta_d}{c_p} > 0.83 \tag{2.13}$$

The remaining waves are considered swell or mixed seas. An advantage of current sensors onboard boys is that both wind and mean wave direction are measured. Therefore, we can add an intermediate range for mixed sea states $0.15 < U_{10}cos\theta_d/c_p < 0.83$ [45]. It is worth mentioning that these are not hard limits, though.

The second way to classify ocean waves is more advanced and relies on the wave directional spectra. This method is called spectral partitioning, and it is implemented for the spectral decomposition of waves to wind sea and swell partitions. An example of a directional spectrum is shown in 2.3. This figure shows a single system describing the sea state. A common condition, especially in the open ocean, is to have multiple systems with unique frequencies coming from diverse directions. One of the main benefits of spectral partitioning is to decompose the different systems into wind waves and swells operationally in numerical models [77]. NDBC does not disseminate historical partitioned data for wind waves

and swells. It recommends empirical methods [36] that rely on the determination of the separation frequency f_s, which separates the different wave systems.

For this study, we use a Matlab algorithm [24] to partition wind wave and swell systems during extreme events (see 4). This algorithm is mainly based on the *watershed* methodology described in [46]. With this method, the different watershed regions are identified from the input directional spectrum matrix, and then they are assigned a number that differentiates each system from the other. A similar algorithm is used operationally for the spectral partitioning in the *Wavewatch III* (WW3) model [94]. There are also other spectral partitioning methods. Wang and Hwang [102] use a spectral steepness method which utilizes the peak frequency to calculate the separation frequency without taking into account the wave direction. Portilla et al. [81] propose a different methodology also based on the watershed algorithm.

2.3   Sea surface roughness and the wind speed profile over the ocean

To quantify the interaction between the atmosphere and the ocean, we need to measure the exchange of momentum at the sea surface. This exchange's direct measurement is not an easy task, though; therefore, oceanographers and meteorologists estimate it through bulk formulas. Precisely, the flux of momentum is quantified by the wind stress on the ocean surface:

$$\tau = \rho_a u_*^2 = \rho_a C_D U_r^2 \tag{2.14}$$

where ρ_a is the density of air, U_r is the wind speed relative to the speed of the water and C_D is the drag coefficient [29]. u_* is the friction velocity. While ρ and U_r can be directly measured, C_D is a subject of many theoretical and experimental parameterizations. The theoretical parameterization of the drag coefficient is derived from the Monin-Obukhov similarity theory:

$$C_D = \left(\frac{k}{\ln z/z_0 - \psi_m(z/L)} \right)^2 \tag{2.15}$$

where $k = 0.4$ is the Von Karman constant, z_0 is the roughness length, ψ_m is a dimensionless function that controls the stability of the atmosphere. Besides, z is the reference height where we want to estimate the drag coefficient, and L is the Monin-Obukhov length. A thorough description of the drag coefficient's dependency on atmospheric stability is available in [89], including examples for different conditions.

For an accurate estimation of C_D, it is necessary to obtain observations of WS, air and water temperature, and humidity, among other parameters. In practice, as is the case for NDBC buoy observations, all these parameters are not always available because they are measured from different sensors. Hence, only dedicated experiments on air-sea interaction provide all the necessary information to assess the air-sea coupling. For this reason, the stability function is often eliminated, and we assume neutral stability of the atmospheric boundary layer over the ocean. A quantification of the errors that this assumption creates is presented in 2.4. Under neutral boundary layer conditions, the wind speed logarithmic profile over the ocean is described by:

$$u_z = \frac{u_*}{k} \ln \left(\frac{z}{z_0} \right) \tag{2.16}$$

Combining the latter equation and 2.14, we can estimate the wind speed at the reference height of 10 meters (u_{10}) given the wind speed at a different height, the drag coefficient and the roughness length [105].

$$u_{10} = u_z \frac{k}{\sqrt{C_{DN}}} \ln^{-1}\left(\frac{z}{z_0}\right) \tag{2.17}$$

NDBC does not report the wind speed at 10 meters, though. It suggests two different ways of adjusting the WS at a reference height [52, 58]. The latter method is based on the power-law wind profile mainly used for the WS adjustment over land, and offshore wind design [55]. A comparison of the logarithmic and the power-law [30] has shown that for values of the wind shear coefficient that approach the ocean surface conditions, the difference between them is minimal and gets even smaller as we go higher in the atmosphere and inside the surface layer (80-100 meters).
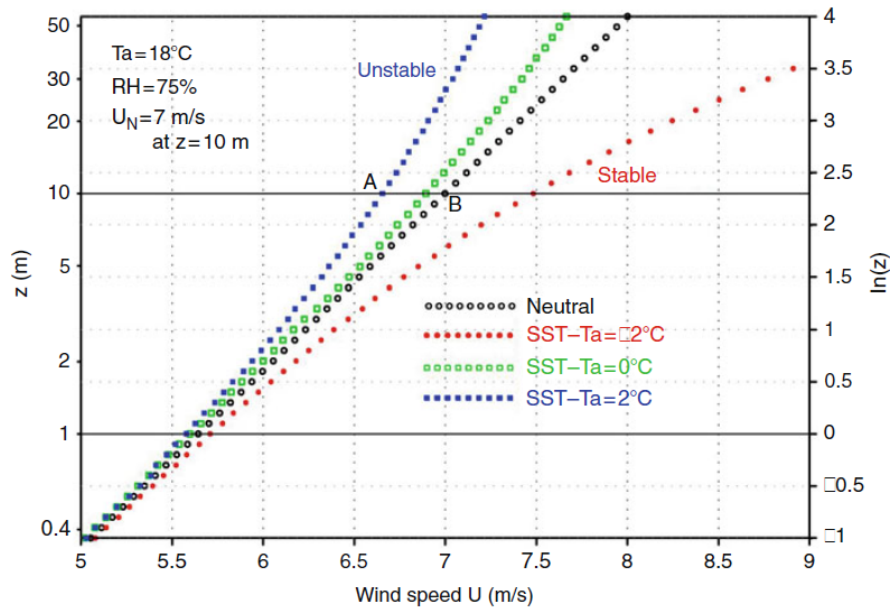
FIGURE 2.4: The influence of the neutral stability assumption in various conditions and heights near the sea surface. Point B represents the wind speed at 10 meters under neutrally stable conditions and A the measured value. Derived from: [59]

We also define the drag coefficient at 10 meters height for a neutrally stable atmospheric boundary layer using 2.15:

$$C_{DN10} = \left(\frac{k}{\ln\left(10/z_0\right)}\right)^2 \tag{2.18}$$

In this case, it is evident that estimating C_D means that we can estimate the z_0. The roughness length over the ocean is not constant and dependent on the sea state. There are proposed methodologies to predict the roughness length from the wave age and SWH [93]. An extensive literature review of the most popular drag coefficient and roughness length parameterizations is available in the literature [13, 108]. The latter also explores the parameterization of C_D and z_0 using the wave age and the wave steepness (H/λ). As the surface wind increases until the ocean surface gets fully rough, the wind stress strengthens its impact, and C_D has higher values. Although it is true for moderate to high winds, it has been proven that the linear increase of the drag coefficient with increased wind speed does

not apply for low wind speeds. During conditions of very low winds ($u_{10} < 4m/s$) and the presence of aligned with the wind direction swells, the momentum flux reserves its sign from positive to negative, and the assumption of a neutrally stable, logarithmic profile over the sea surface is no longer valid [29, 42, 44].

From the number of available parameterizations, it is evident that the task to describe the air-sea interactions sufficiently is multi-faceted. This study uses a specific parameterization while considering the errors therein and the possible deviations from the truth. Specifically, we use equation 2.17 to adjust the reported wind speed observations from the buoys to the reference height of 10 meters. Representative values of $C_D = 1.2 \times 10^{-3}$ and the corresponding $z_0 = 9.7 \times 10^{-5}m$ derived from 2.18 are also used in similar studies [86, 107]. Anemometers onboard buoys are placed on various heights (3.5 to 4.5 meters) depending on the buoy type. Hence, adjusting to a reference height is also beneficial for consistent comparisons.

2.4 Literature review of bulk formulae for wind-wave relationships

In the first section of this Chapter 2.1, we showed that SWH is estimated from the frequency spectrum and it is equal to four times the integral of the area under the continuous line of the spectrum, or the RMS elevation.

Historically, WS and SWH relationships are synonymous to the wave spectrum. Pierson's spectrum approach to ocean waves [80] was transcedental as he developed the theoretical background and the statistics of ocean wave spectra. Neumann implemented Pierson's theory and created the first wave spectrum using visual wave observations from ships. The Neumann spectrum was the first to connect the WS at the height of the anemometer as a driving force for the waves with the frequency spectrum. The fully developed or fully aroused sea was then defined as the sea state with a spectrum of all frequency components with the maximum energy under a specific value of WS forcing. This led to the SWH definition and the first relationships of SWH and WS based on the wave spectrum of a fully developed sea. The first three relationships came from the Pierson-Neumann system of equations 2.19, the Sverdrup-Munk-Bretschneider wave forecasting method 2.20 and the Darbyshire spectrum 2.21.

$$H_s = 7.065 \times 10^{-6} u^{2.5} \tag{2.19}$$

$$H_s = 2.667 \times 10^{-4} u^2 \tag{2.20}$$

$$H_s = 1.39 \times 10^{-4} u^2 \tag{2.21}$$

A comparison of theoretical spectra and their corresponding wind-wave relationships is available in [75].

Kitagorodskii based on the Pierson-Moskowitz spectrum [79], proposed similar empirical laws for the fully-developed sea. One of Kitagorodskii's empirical formulas is also the wave age wind-wave equilibrium equation 2.11. For the fully-developed sea, he connected u_{10} with H_s [19]:

$$H_s = \frac{0.2}{g} u_{10}^2 \tag{2.22}$$

A few years later, Carter [14] reviewed the JONSWAP spectrum [49] and proposed the following relationship:

$$H_s = 0.02466u_{10}^2 \tag{2.23}$$

This relationship is also used as a reference in similar and contemporary studies [4]. Carter also proposed equations for the duration and fetch-limited seas:

$$H_s = 0.0163X^{0.5}u_{10} \tag{2.24}$$

$$H_s = 0.0146D^{5/7}u_{10}^{9/7} \tag{2.25}$$

The sea is considered duration-limited when:

$$D > 1.167X^{0.7}u_{10}^{-0.4} \tag{2.26}$$

X is the fetch, the perpendicular distance to the upwind coast in kilometers and D is the duration in hours. In this study, fetch is not included directly in the estimations. However, we examine the relationships for each of the main wind directions to indirectly connect them with the variation of the fetch in coastal regions.

WMO [77] suggests a similar empirical relationship for the estimation of SWH when u_{10} is given.

$$H_s = \left(\frac{u_{10}}{12.5}\right)^2 \tag{2.27}$$

Finally, other studies incorporate wind-wave relationships from wave models for classification of the sea state into wind-waves and swells using altimeter data [16].

All the relationships mentioned above are valid under the assumptions of deep water waves and fully developed seas. Consequently, SWH cannot be accurately estimated from u_{10} in all other growth stages or with presence of swells.

2.5 Wind Speed Probability Density Functions

This section is about the statistical interpretation of the long-term time series from the buoys. Specifically, the ultimate goal is to indicate the Probability Density Functions (PDF) that describe the u_{10} distribution as it is estimated from the buoy records for each location.

Wind PDFs are required for design assessment at the offshore wind farm site before its installation [55]. They are an integral part of the wind data analysis, and they are usually combined with the wind roses that provide the directional distribution of the wind speed [22]. The average wind turbine power is also associated with the PDF estimation [68]. For the wind PDF estimation, the suggested buoy dataset is the 10-minute average U_{10}. Although the modern wind turbine hub heights are greater than or equal to 100 meters, an extrapolation of the surface WS to such height would result in high uncertainty [8]. Therefore, a reference height of 10 meters is selected for this study. The results would also prove useful as a reference to a similar estimation of the PDFs from wind lidar buoy and offshore wind tower observations in a later stage.

The standard and most widely-accepted wind speed distribution is the Weibull:

$$f(x) = \alpha x^{\alpha-1} exp\left(-x^\alpha\right) \tag{2.28}$$

Where $\alpha > 0$ is the shape parameter. The best fit to our data is the 3-parameter Weibull though, for $y = (x - \gamma)/\eta$, where η is the scale and γ is the location parameter. Special cases of the Weibull are the Exponential ($\beta = 1$) and the Rayleigh ($\alpha = 2$) distributions.

There also regional characteristics of the wind speed distribution. Previous studies using buoy data have proved that the Weibull distribution is adequate for estimating the surface wind PDFs only for specific regions [68]. They propose that universal models should be a mixture of multiple distributions with different assigned weights for each distribution, depending on the domain. There are also studies suggesting that the Johnson S_B [90, 91] distribution can be accepted as an alternative PDF and the best fit for certain regions. As described in the results, we identify and evaluate four distribution with the best fit for the WS data in SNE. Two of them, Weibull and Rayleigh are already referenced above. Besides, the Beta and Johnson S_B distributions are also suggested to describe the long-term WS distribution at SNE:

$$f(x) = \frac{\Gamma\left(\alpha + \beta\right)}{\Gamma(\alpha)\Gamma(\beta)} x^{\alpha-1}(1-x)^{\beta-1} \tag{2.29}$$

This is the Beta 2P distribution where Γ is the Gamma function and $\alpha > 0$, $\beta > 0$ are the shape parameters. We evaluate the 4P Beta PDF by adding scale and location parameters for $y = (x - \gamma)/\eta$, where η is the scale and γ is the location parameter respectively.

$$f(x) = \frac{b}{x(1-x)} \phi \left(\alpha + \beta \log \frac{x}{1-x} \right) \tag{2.30}$$

This is the Johnson S_B 2P distribution where $\alpha > 0$, $\beta > 0$ are the shape parameters and ϕ is the normal distribution PDF. We evaluate the 4P Johnson S_B PDF by adding a scale and location parameters for $y = (x - \gamma)/\eta$, where η is the scale and γ is the location parameter respectively.

We identify the single, univariate distributions of best fit to the long-term u_{10} time series using the extended *SciPy* library of PDFs for each buoy location. This library utilizes the Maximum Likelihood Estimation (MLE) methodology for fitting to the theoretical distributions and the estimation of the distribution parameters.

2.6 Principles of Satellite Altimetry

The Radar altimeter is an active, nadir looking microwave instrument that emits its impulses to the earth's surface. Once it receives them back, it measures the travel time, the magnitude, and the shape of each return signal.

The average of hundreds of pulses shape the mean returned signal. Specifically, the signals tracked originally by the altimeter are convolved to a single waveform after being fitted to a mathematical model. These function fitting methods are evolving through the years and are described in [40]. The process is fundamental for satellite altimetry and constitutes the retracking model. The mathematical model used for the fitting of the retracking algorithm is the Brown-Hayne model [12, 50] for the Low-Resolution Mode (LRM) and the SAMOSA model for the Synthetic Aperture Radar (SAR) altimetry [84]. As a result, a typical waveform in the open ocean has three distinct areas, as presented in Figure 2.5. The first one is the area of low, close to zero power. The second is the leading edge, which contains the area from the time that the waveform's power begins to increase until its peak. The third is the trailing edge, which is the area of decaying power of the waveform.

Except for the impulses' signal, an accurate determination of the earth's orbit is critical, especially the radial component. In addition, the target accuracy of the distance between the satellite and the sea level is on the order of 1 centimeter. Therefore, corrections due to the

errors caused by the signal's delay as it travels through the ionosphere and the atmosphere have to be applied. The ionospheric corrections are essential to measuring the delay of the altimeter signal's travel time caused by the ionosphere's free electrons. It is also one reasons why a dual-frequency (Ku or Ka and C band) altimeter instrument is needed onboard the satellite. Besides, there are two kinds of atmospheric corrections: the dry tropospheric and the wet tropospheric correction. For the latter, the microwave radiometer instrument is used to measure the water vapor in the atmosphere. A significant challenge for coastal altimetry is that the microwave radiometer footprint radius is close to 50 kilometers. Therefore, the brightness temperature of the land contaminates the measurement in coastal areas. The wet troposphere correction is also very challenging due to the spatiotemporal variability of water vapor in the atmosphere. For these reasons, the uncontaminated signal in the open ocean is used in conjunction with in situ observations, when and where available, to correct the wet troposphere delay. Furthermore, there is uncertainty also at the surface of the ocean. Specifically, geophysical adjustments have to be applied to estimate parameters such as the earth and ocean tides, the sea state bias, and a dynamic atmosphere correction.

In coastal altimetry, the retracking model's fitting to get the final waveform has additional challenges as we get closer to the coast. Due to the extended radius of the altimeter footprint, land intrudes in the received signal, and there is land contamination of the waveform [43]. Hence, the final waveform can be corrupted, especially in high sea state conditions. Secondly, as we get closer to the coast, the footprint's backscatter is different from the one in the open ocean. Indeed, in coastal areas, the altimeter footprint may cover both a windy area with considerable sea surface roughness and an area of calm sea state with an almost flat surface "shaded" by the wind. As a result of the limitations mentioned above, the final waveform shows unusually higher power peaks in the trailing edge, a part of the waveform that we should otherwise not consider when fitting to the model to estimate the geophysical parameters.
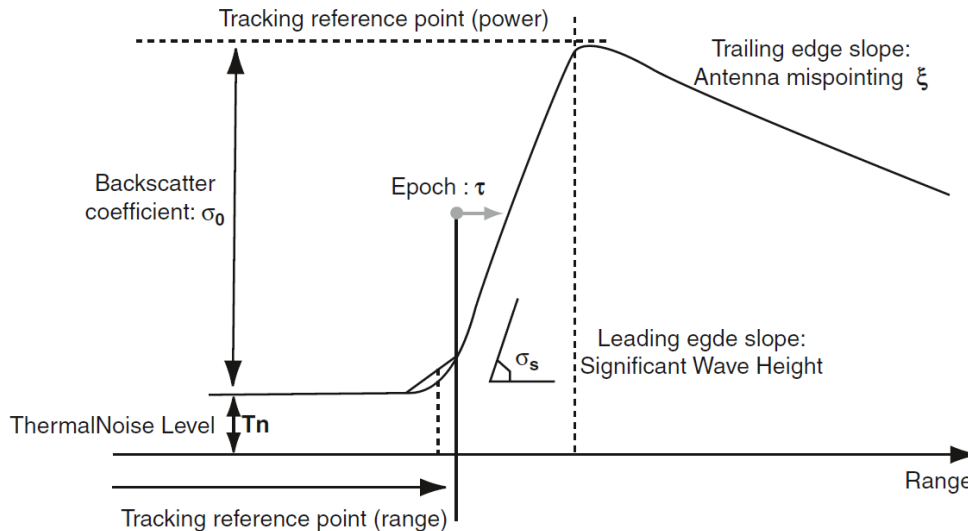
FIGURE 2.5: The Brown theoretical retracking model for LRM altimetry and the derived parameters. Derived from: [40].

These limitations are evident when we consider the pulse-limited signal of the LRM altimeters. The effective footprint of the LRM altimeter is given by:

$$f = \frac{\pi R_0 (c\tau + 2H_s)}{1 + R_0/R_E} \tag{2.31}$$

Where c is the speed of light, τ is the pulse length, H_s the SWH, R_0 the altitude of the satellite and R_E the Earth's radius.

When the sea is calm, the altimeter's footprint is approximately a 2-kilometer radius in both directions, the along-track and the across-track. In contrast, during a storm or high sea state, the effective footprint can extend to over 7 kilometers. The principles of pulse-limited altimetry are extensively described in [15]. SAR or delay-Doppler altimetry using the Ray et al. [84] model, revolutionized how the signal's power is used. On the one hand, it considers both the leading and the trailing edge of the retracked waveform instead of the smaller area of the leading edge considered for the LRM. The finer resolution on the along-track and the waveform's reduced noise are the main aspects of the evolution of SAR altimetry [83]. Its Pulse-Doppler-limited footprint's resolution can be constrained to approximately 300 meters only on the along-track. On the across-track, though, the resolution remains similar to the pulse-limited LRM. The effective footprint of SAR looks like slices of the LRM circular footprint as in Figure 2.6. The SAR altimetry pioneer is Cryosat 2 satellite, as it is equipped with the SIRAL instrument that operates in both modes (see 3.1.2). Raynal et al. [85] demonstrates the increased accuracy of the SAR's higher spatial resolution over different areas worldwide. The European Space Agency (ESA) Sentinel 3 twin satellites, A and B, are the first missions that use the SAR altimetry mode exclusively. Currently, the remaining altimeters in orbit are operating in LRM mode. On the other hand, SARAL-AltiKa is the only LRM altimeter that emits its impulses in higher frequency using the Ka-band, which increases the accuracy of the measured parameters and reduces the noise of the final waveform.
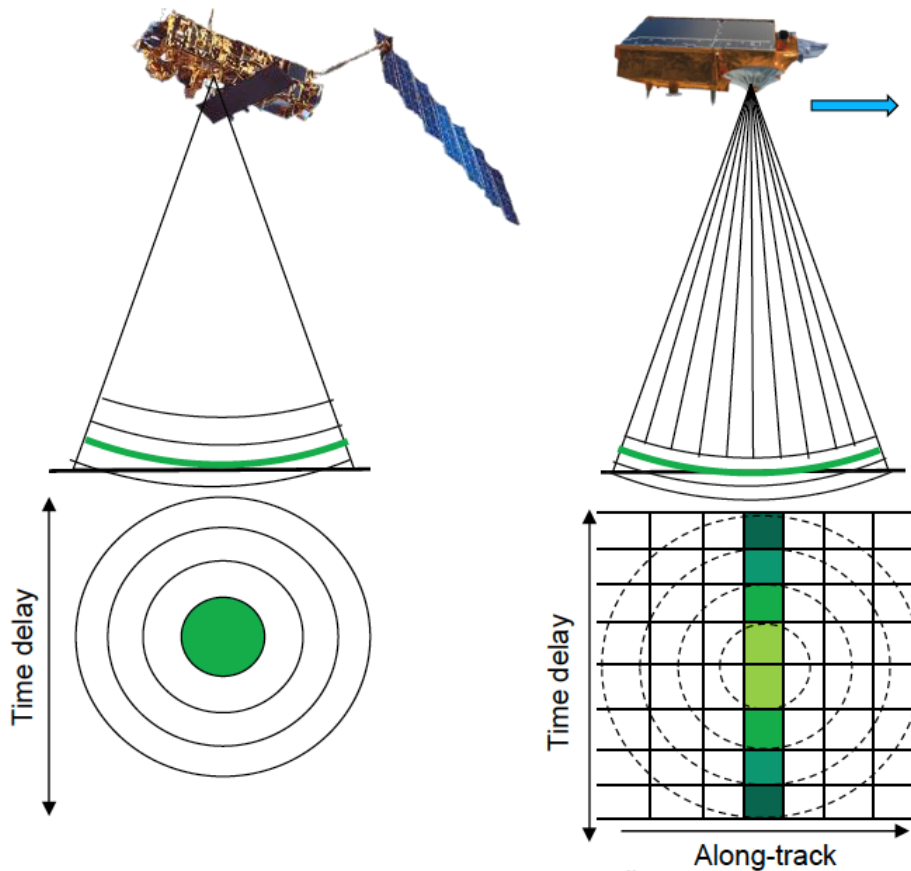
FIGURE 2.6: A representation of the LRM and SAR altimeter footprint.

We can determine at least three essential parameters from the retracked waveform 2.5. The first one is the epoch. We can then estimate the range from the epoch, which is the

signal's travel time, until it reaches back the satellite and is connected with the Sea Surface Height (SSH). The second important parameter of the waveform is the slope of the leading edge (or width or rising time of the leading edge), which is connected to the estimation of the SWH. The third essential parameter is the backscatter coefficient derived by the received signal's power and is associated with the surface WS. For this study, the focus is on two of the three aforementioned geophysical parameters and their corresponding estimates, namely the SWH and the WS.

As previously discussed, the estimation of the SWH is connected with the slope of the leading edge. Specifically, the slope is a function of the root mean square error of the SWH. A steep leading edge represents a small value of the SWH. In contrast, for higher values of SWH, for example, during a storm, the return signal starts to rise earlier until it reaches its peak power, and also, the shape of the echo is different [6]. The difference between the two resulting waveforms, one during a calm sea and one for a rougher sea surface, is shown in Figure 2.7(b). It is evident that SWH from altimeters is derived with an entirely different measurement method with respect to buoys described in Chapter 2.1.

The radar altimeter also measures the backscatter signal's strength. This value is inversely proportional to the sea surface Mean Square Slope (MSS) [17] which is related to the sea surface roughness induced by the wind. Therefore, the estimated WS increases as the surface MSS gets higher and the backscatter becomes smaller. The main source of errors in the altimeter estimation of the WS is the empirical nature of the corresponding algorithms that do not consider the impact of the sea state growth, primarily due to swells [1, 37]. The retracking of hundreds of noisy signals and the need for reliable atmospheric corrections, notably close to the coast, makes the task even more challenging.
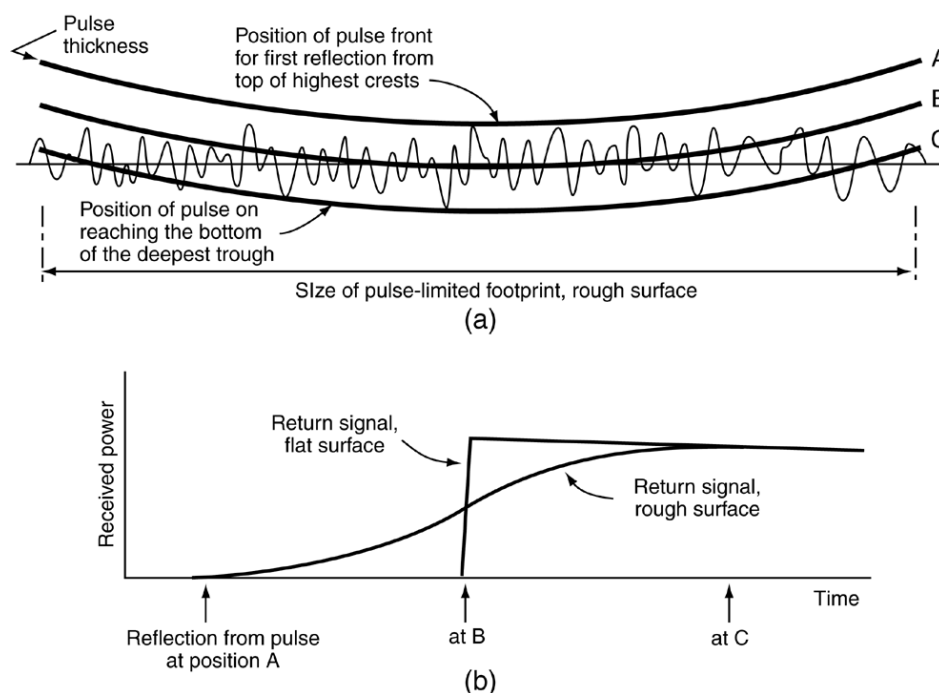
FIGURE 2.7: (a) Illuminated surface geometry. (b) The resulting shape of the reflected pulse. Derived from: [87]

Chapter 3

Methodology

3.1 Data preprocessing

This study is based on the interpretation of wind and wave conditions using in situ and remote sensing observations from buoys and altimeters. There are fundamental differences in how in situ platforms measure and report the geophysical parameters compared to observations from satellite altimeters. On the one hand, buoys' measurements are considered the "ground truth", owing to their ability to provide a reliable, long-term, and continuous time-series record of temporally processed oceanographic and meteorological parameters from the raw data for a specific location. On the other hand, altimeters provide instantaneous measurements representing their sea surface footprint with a low temporal resolution. A description of satellite coastal altimetry challenges is available in 2.6.

This chapter aims to provide an outline of the collection and preprocess of the different data types. This step is essential because both datasets contain inherent and unique sources of error [37, 67, 109], and they need to be quality controlled before the analysis. The next step is to accurately describe the methodology that was implemented to achieve our final results.

3.1.1 Buoy Data Collection and Organization

The importance of an extended and well-preserved network of buoys in the United States of America is well documented in [72]. This study utilizes all the wind and wave geophysical parameters reported by multiple stations of the NDBC and CDIP. CDIP is operated by the Ocean Engineering Research Group (OERG), part of the Integrative Oceanography Division (IOD) at Scripps Institution of Oceanography (SIO), and it is responsible for the operation and maintenance of buoys 44097 and 44091. Buoy 44039 is part of the Long Island Sound Integrated Coastal Observing System (LISICOS), and it is operated and maintained by the University of Connecticut (UConn) Marine Sciences Department. The remaining buoys are operated and maintained by NDBC.

Information about all stations' location characteristics and their data availability are included in Tables 3.1 and 3.2 respectively. The anemometer height is 4.1 meters for all buoys with available wind measurements except buoys 44020 (3.8 meters) and 44039 (3.5 meters). When is needed, wind speed is adjusted at 10 meters height, assuming neutral stability of the atmospheric boundary layer, as described in 2.3.

Data are available at the NDBC and CDIP websites. Directional wave spectra for buoy 44097 were downloaded from CDIP archive at THREDDS Data Server (TDS) in NetCDF format. All other geophysical parameters were downloaded from the NDBC website as *.txt* files. NDBC provides an extensive description of the measurement process, the statistical analysis and quality control of the raw data, and the various error sources in [71]. The buoy anemometers' reported accuracy is $\pm 1 m/s$ with a resolution of $0.1 m/s$. The corresponding

(A) Buoy 44025 (Long Island)

(B) CDIP Datawell Waverider Buoy
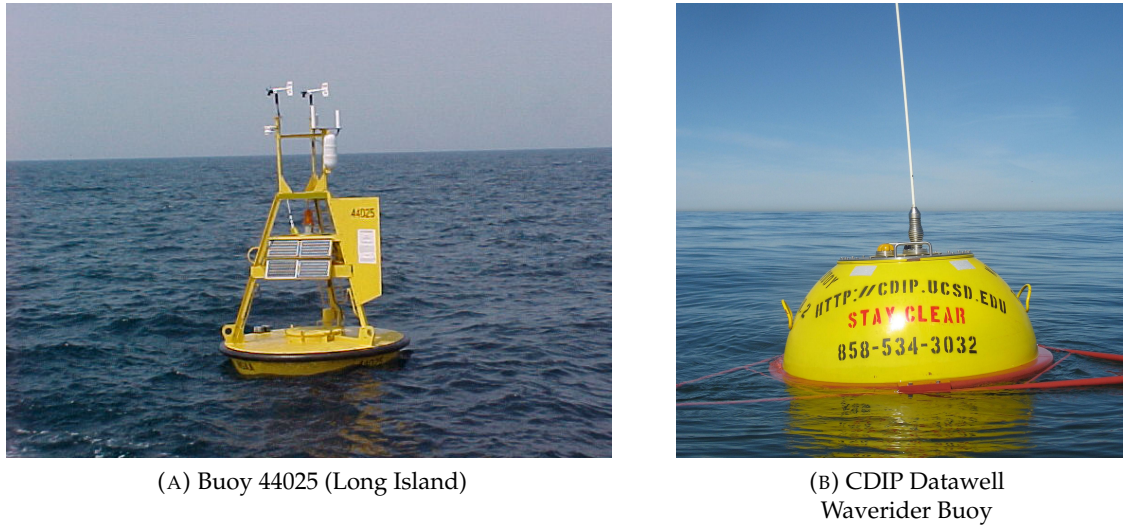
FIGURE 3.1: The two types of buoy stations moored in SNE.

accuracy of the SWH measurements is $\pm 0.2m$ with a $0.1m$ resolution. After careful examination of the quality-controlled time series, additional filtering criteria were implemented to eliminate erroneous data.

Buoy #	Location	Lon. (deg. W)	Lat. (deg. N)	Water Depth (m)
44097	Block Island, RI	-71.127	40.969	48.16
44020	Nantucket Sound	-70.279	41.493	14.30
44025	Long Island	-73.164	40.251	36.30
44017	Montauk Point	-72.049	40.693	48.00
44065	New York Harbor Entrance	-73.703	40.369	25.00
44039	Central Long Island Sound	-72.655	41.138	27.00
44008	Southeast of Nantucket	-69.248	40.504	74.70
44066	East of Long Beach, NJ	-72.644	39.618	78.00
44091	Barnegat, NJ	-73.769	39.778	25.60

TABLE 3.1: Buoys' location, coordinates and water depth.

Specifically, WS data with values smaller than or equal to 0.2 m/s and SWH values lower than or equal to 0.1 meters were discarded. Previous studies [3] have used even stricter filtering criteria for the WS, recognizing that one disadvantage of the 4-blade, wind-vane sensors onboard buoys, is that they need a minimum, nonzero WS to start measuring and recording data reliably. The 0.1 meter-limit for SWH is also used by CDIP. Furthermore, data availability in terms of years of available data, as documented in Section 3.2, imposes the need for consistency on the final buoy time series. The final buoy datasets consist of data from 2007 until the end of 2019. Buoy time series have gaps owing to maintenance or change of the sensor payloads. The main goal was to have at least ten years of data for each buoy for consistent analysis. Previous studies have also documented that ten years of wave data are enough to characterize the seasonal variability for a specific location [7].

For this reason, buoy 44091 data were used only for the validation with altimeter data. Buoy 44039 data has two disadvantages that prevented their use for other than the validation with altimeters section of this study.

Buoy #	Distance to Coast (km)	Data Type	Data Availability (Years)
44097	41.0	wave only	2009-Present
44020	13.0	wind/wave	2009-Present
44025	42.0	wind/wave	1975-Present
44017	30.0	wind/wave	2002-Present
44065	23.0	wind/wave	2008-Present
44039	13.0	wind/wave	2004-2019
44008	103.0	wind/wave	1982-Present
44066	121.0	wind/wave	2009-Present
44091	27.5	wave only	2014-Present

TABLE 3.2: Buoys' distance to the closest coast and data availability depending on the type of the reported parameters and its period.

Specifically, SWH values have a precision of one decimal number, and dominant periods are rounded to the closest integer. Data are also recorded at irregular times, which creates challenges for interpreting the results, especially compared to the other buoys' stable recording times.
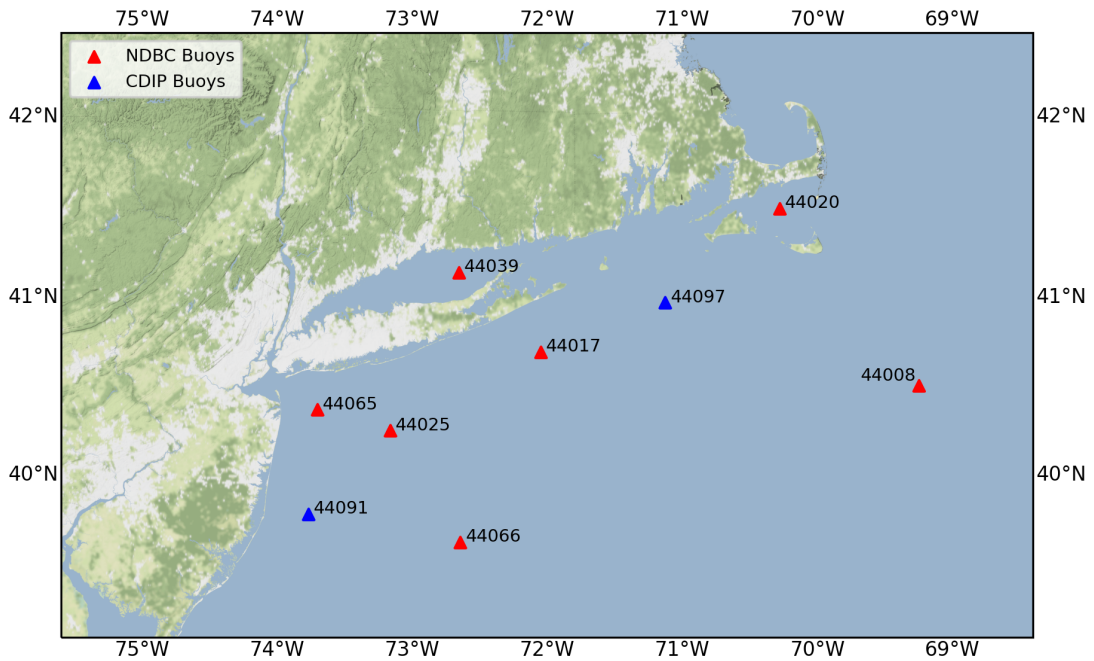
FIGURE 3.2: NDBC and CDIP buoys in the SNE region.

It is essential to mention the different datasets that were used and their unique characteristics. First of all, buoy payloads can record WS and wind direction in two distinct ways described in [71]. The first one is an 8-minute average of 1Hz observations, which leads to an hourly dataset. Data are reported at the end-of-acquisition minute, but that does not mean that the observation value includes measurements from the whole hour. This dataset was used when synchronous wind and wave observations were needed to validate altimeter data. The second one is a 10-minute average of the 1Hz observations, which is reported again at the end-of-acquisition minute. Still, the difference is that it is the average of the whole 10-minute period. This dataset is referenced as the 10-minute average dataset from now on, and it is especially useful for studying the diurnal variability and wind climate. It is

also the recommended dataset for wind observations, according to BOEM for offshore wind-related studies [22]. The 10-minute average dataset is used when wind data are processed independently, and the hourly dataset is used when combined with wave data.

Wave data are measured and reported in an entirely different way due to their more complex nature. All wave parameters are derived from the estimated energy spectra [71]; therefore, they are neither instantaneous nor average values of continuous observations. Wave parameters represent observations every 20 minutes. The acquisition time starts at the 20th minute of each hour and ends at the 40th. The final reported measurements are synchronized to the closest hourly wind observations. This is useful when we want to study, for example, the relationships between WS and SWH. Still, at the same time, we have to consider that the observations are not simultaneous in reality. Data organization and preprocessing were implemented using Python *Pandas* and other supplemental packages of the Python programming language. The final time series were saved as separate *.txt* files for each buoy and are available for future use.

3.1.2 Altimeter Data Collection and Organization

The theoretical aspect and the distinct qualities of the satellite altimeter observations are already emphasized in 2.6. This chapter will provide the necessary information regarding the altimeter datasets' characteristics, the reasons for their choice, and their actual use as input to the analysis.

	SARAL	Jason 3	Sentinel 3A	Sentinel 3B	Cryosat 2
Repeat Cycle	35	10	27	27	369
Frequency Band	Ka/C	Ku/C	Ku/C	Ku/C	Ku/C
Data Availability	03/2013-	09/2016-	03/2016-	05/2018-	07/2010-
Instrument	AltiKa	Poseidon-3B	SRAL	SRAL	SIRAL
Operation Mode	LRM	LRM	SAR	SAR	LRM/SAR
Product Type	GDR	GDR	NTC	NTC	GOP

TABLE 3.3: Satellite Altimeters used in this study and their characteristics.

First of all, this study's scientific context dictates the use of data from multiple altimeter missions. Currently, there are six satellite altimeters in orbit. Information about the main characteristics of each altimeter that is included in this study is provided in 3.3. Data from the most recent altimeter mission, the Chinese HY-2B, were not used or examined. Sentinel-3A and Sentinel-3B satellites are part of the same mission, often characterized as "twins" because they have complementary orbits. They are the only satellites equipped with multiple sensors, including the radar altimeter instrument SRAL.

Satellite with ARgos and ALtiKa (SARAL-AltiKa) is a collaboration between the Centre National d'Etudes Spatiales (CNES) and the Indian Space and Research Organization (ISRO) [99] with the participation of the European Organization for the Exploitation of Meteorological Satellites (EUMETSAT). This mission is unique, mainly for two reasons. SARAL-AltiKa is the first mission that takes advantage of the high-frequency Ka-band (35.75 GHz) capabilities. Specifically, its high-frequency signal means that the altimeter footprint is smaller, leading to better spatial resolution and more accurate measurements, in particular close to the coast. The disadvantage of Ka-band's high frequency is its sensitivity to water vapor and rain, leading to signal attenuation and making the atmospheric corrections even more challenging [10, 96]. SARAL-AltiKa is also unique because it was launched using the same orbit and ground tracks as its predecessor mission, ERS, from March 2013 until July 2016. From July 4, 2016, it has entered its second phase, which is called the drifting phase or SARAL-DP.

Since then, SARAL-AltiKa does not maintain its altitude; therefore after each repeat cycle, its ground tracks are no longer passing from the same location as the previous, but they "drift" a few kilometers. The mission agencies made this decision to preserve a few more years of its lifetime. It has been proven that it is possible to maintain good mesoscale sampling even without keeping the same altitude for the satellite [21].

The Jason 3 mission involves CNES, the National Aeronautics and Space Administration (NASA), EUMETSAT, and the National Oceanic and Atmospheric Administration (NOAA). It is the successor of Jason 2, and it was launched on January 17, 2016. Jason 3 entered its calibration and validation phase on February 19, 2016, when it also started measuring and reporting data. Its primary instrument, the Poseidon-3B altimeter, sends and receives its impulses in Low-Resolution Mode (LRM), and it operates in Ku-band (13.575 GHz). Jason 3 is also unique because it has the highest temporal resolution and the lowest spatial resolution of all the altimeters. Every repeat cycle covers ten days, and every ascending or descending along-track is at an approximately 2.8 degrees distance from the closest. The instruments onboard Jason 3, which are also common to satellites that include altimeters, are shown Figure 3.3.

Sentinel 3 mission is organized and implemented by the European Space Agency (ESA) and EUMETSAT. Satellite altimetry is one of its main objectives, but not the exclusive. Its payload also includes instruments that measure and record Sea Surface Temperature (SST) and Ocean Colour data that are equally important to the geophysical parameters derived from the radar altimeter. So far, Sentinel 3 is comprised of two satellites, Sentinel 3A and Sentinel 3B. Sentinel 3A launched on February 2016 and Sentinel 3B on April 2018. They are often characterized as the "twin mission" because their along-tracks are complimentary to increase spatial coverage. Both satellites are equipped with the same payloads; hence they will be referenced in this study as Sentinel 3. Sentinel 3 SRAL altimeter sends and receives its impulses in Ku-band. It is also worth mentioning that it is the first mission that operates in SAR (or delay-Doppler [83]) mode exclusively, even if it can function in both SAR and LRM modes. As a result, only the across-track resolution of its effective footprint is still pulse-limited because the along-track resolution is increased and constrained to 300 meters. Conventional altimetry operates in low-resolution mode, which is pulse-limited on both the across and the along-track directions. SRAL altimeter's received pulses can also be processed in Pseudo-Low Rate Mode (PLRM) and produce LRM-like waveforms when operating in SAR mode. Still, PLRM's estimates are noisier and have worse performance in coastal regions [74]. In this study, only SAR mode data are used and evaluated.

Cryosat 2 is an ESA mission launched on April 2010, and its primary objective is to monitor the Arctic sea ice extent. It is a pioneer altimeter mission because it is the first-ever to operate in SAR mode. Specifically, the SIRAL altimeter onboard Cryosat 2 can operate in three modes: LRM, SAR, and SAR Interferometry (SARIn). Generally, SIRAL operates like a traditional altimeter in LRM mode. SAR processing mode is available for a few oceanographic areas, specific for each cycle. SARin is only available for the ice sheet margins and over mountain glacier regions. Therefore, Cryosat 2 data used in this study are LRM-processed with very few exceptions that are processed using the SAR waveforms. Cryosat 2 has the most extended repeat cycle (369 days) with an approximately 30-day subcycle covering a specific region of interest. It is also worth mentioning that its orbit does not repeat after completing every cycle, unlike every other conventional altimeter mission, which makes it unique in that regard.

For each mission, there are three types of dataset files available: a reduced dataset that contains only the 1Hz data, a native or standard including both the 1Hz and the 20Hz parameters, and an expert or enhanced sensor product that includes the full waveforms. Only the native dataset was collected, organized, and used for this study.
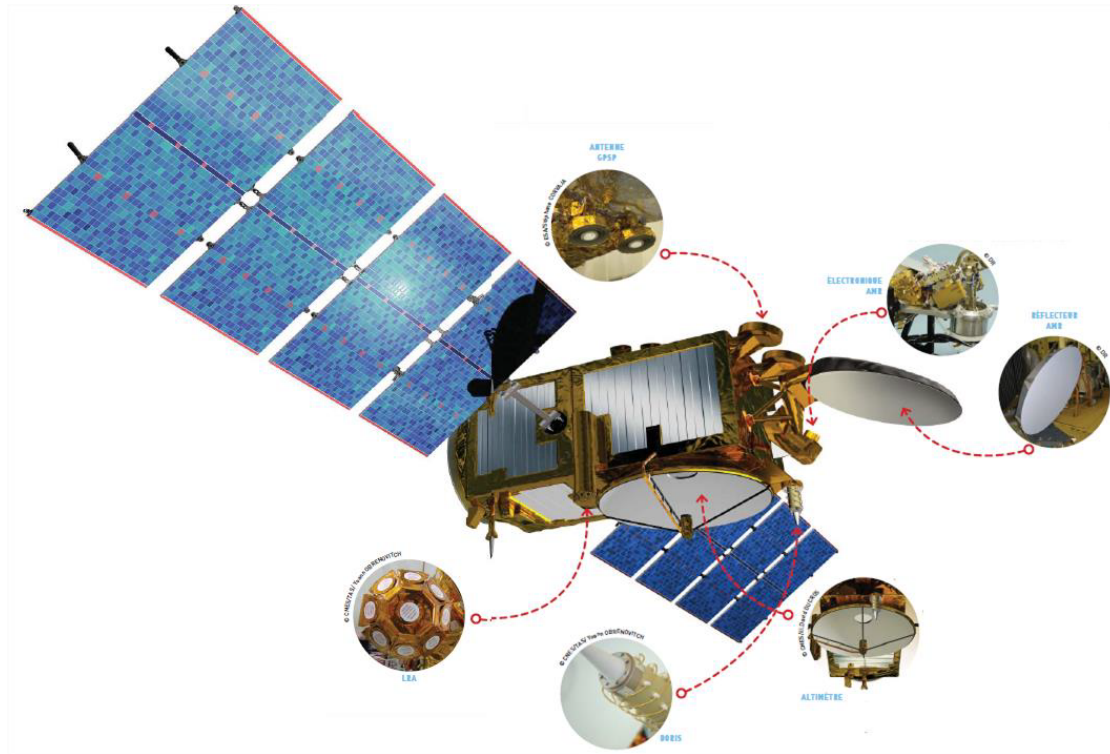
FIGURE 3.3: The main components of Jason 3 payload including the radar altimeter Poseidon-3B (center), the Advanced Microwave Radiometer (AMR, upper center) and the radio positioning DORIS system for the precise determination of its orbit (lower center). Other instruments include a Laser Reflector Array (LRA) used for the calibration of the orbit determination system (lower left) and a precision Global Positioning System Payload (GPSP) antenna (upper left). These components are common to all satellites that contain altimeter instruments. Derived from: [78]

Besides, every altimeter mission has a family of three distinct Level 2P (processed) product types, distinguished by increasing latency and accuracy. This family of products is often called Geophysical Data Records (GDR). Near Real-Time (NRT) or Operational GDR (OGDR) products are mainly useful for the operational community. They are disseminated only a few hours after the initial waveforms are received, but they may contain outliers. Short Time Critical (STC) or Interim GDR (IGDR) products have additional auxiliary data used in the processing, and they are provided a couple of days after the NRT products. The third product type is the Non-Time Critical (NTC), or GDR, and the only one used in this study. For Cryosat 2, this product type is called Geophysical Ocean Product (GOP) to distinguish it from the ice processors' GDR dataset. LRM products are followed by an additional M letter (GOPM) and SAR products with an R (GOPR). These products are delivered typically one month or two months after data acquisition with more precise orbit determination and atmospheric corrections. It incorporates additional auxiliary/ancillary data with lower errors.

There are different dataset standards throughout the lifetime of each altimeter. Generally, the initial standard uses the waveform retracking algorithms and geophysical/atmospheric corrections of the calibration/validation (Cal/Val) phase. Then, depending on the instrument's skills and contemporary research developments, the initial standards are updated one or two times during every altimeter's lifetime. Specifically, in this study, Jason 3 GDR-T data are used from February 2016 until September 2016. From September 2016, the GDR-D version is used. The most recent, GDR-F version of SARAL-AltiKa data is used for its first

phase (March 2013 until July 2016) and also for the period from November 2019 until July 2020. For the intervening period, the previous (GDR-T) version is used because it is not disseminated yet on the AVISO *ftp* server in its entirety.

Quality control is critical during the preprocessing stage. Editing criteria should be implemented on Level 2 data to filter outliers or erroneous data and keep only the valid observations before their use in the analysis. The two primary sources of the suggested editing criteria are every mission's data handbook [11, 31, 32, 65, 78], and the Quality Assessment Reports (QAR) that accompany the data files after the completion of each cycle. Generally, the discarded observations are not extensive due to the high data quality from the current missions. As already discussed, each altimeter has its unique features. For example, SARAL-AltiKa's Ka-band is more sensitive to rain and water vapor. Simultaneously, it is expected to provide more observations with higher accuracy close to the coast because of its smaller wavelength and effective footprint. These characteristics are also reflected in the valid altimeter data for each mission. It is the user's responsibility to select the suitable editing criteria according to the application. For this study, we use the official mission handbooks and QAR guidelines to filter suspect or erroneous Level 2 altimeter data.

Although there are multiple sources of satellite altimetry data, SARAL-AltiKa and Jason 3 GDR data were downloaded from the Aviso-CNES Data Center website, Sentinel 3 NTC data were downloaded from the EUMETSAT Coda website, and Cryosat 2 data were downloaded using ESA's Cryosat User Tool (CUT).

For the preprocessing stage, NetCDF data files were input, subsetted, filtered using Python *xArray* [51] package, and the final, quality-controlled data were written to single, *.txt* files using Python *Pandas* [64] to be available for future use.

3.2 Spatio-temporal collocation

The satellite altimeter products consist of point observations that are representative of the nadir-pointing sensor's footprint center. We have previously discussed that the altimeter's effective footprint cannot be considered a single point, though. It has a radius that is not constant and changes with respect to the sea state. This is also important when we want to compare altimeter measurements' accuracy against the buoys, which are stations in point locations.

A review of the different validation approaches, terminology, and metrics to assess the quality of satellite observations is available in [60]. Validation is a process that requires the determination of specific criteria by the user to accomplish two primary goals. First of all, there should be limits to the two datasets' proximity both in space and time. The process of applying these limits is called spatiotemporal collocation and results in the final datasets with the collocated observations to compare. Indeed, the validation of altimeter against buoy observations is sensitive primarily to selecting the collocation or sampling radius and secondarily to the chosen time window [54]. It has been documented that a reduced sampling radius or closer proximity of the two observations in space leads to smaller absolute differences between the two collocated values [67]. Traditionally, for global scale validation of 1 Hz altimeter data, a sampling radius of 50 or 25 kilometers and a time window of 30 or 60 minutes is selected. The data are again quality-controlled to remove possible outliers. The individual measurements are then straightforward or weighted averaged to compare with the buoy observations because they are considered simultaneous with a spatial distance of 6 to 7 kilometers [26, 82, 103]. The selection of a suitable sampling radius becomes challenging when approaching a coastal region due to the land contamination of the waveforms and the number of available stations. The former is discussed in 2.6, and the latter is the second goal we must achieve, the statistical significance of the results. Validation is often a compromise

between the two, and selecting the appropriate sampling radius and time window depends on the application.

There are inherent sources of measurement error in both types of observations. The accuracy of WS and SWH measurements from buoy sensors is reported in 3.1.1. On the other hand, the challenges of coastal altimetry are explained in 2.6. The primary sources of inaccuracy in altimeter measurements include estimating parameters like the backscatter coefficient or the altimeter range from the waveform retracking and the empirical nature of the algorithms used to calculate the final geophysical parameters (SSH, SWH, WS). Hence, instrumental errors are the first source of uncertainty when comparing two different measurement systems' observations. Even if the two measurement systems had zero or identical uncertainty, their comparison would still be challenging due to their diverse spatial and temporal sampling. In other words, we need to consider how close are the observations in space and time due to the wind and wave variability in multiple spatial and temporal scales. Furthermore, we also need to take into account the sampling variability of the two types of observations. Specifically, the reported observations from buoys as described in 3.1.1 are temporal averages, whereas the 1Hz altimeter values are considered instantaneous.

This study aims to validate wind speed and significant wave height measurements from altimeters with buoys in the SNE. There are limited buoy stations in this domain, as described in 3.1.1. At the same time, most of the stations are located closer than 50 kilometers from the coast, which is a choice of a limit for similar studies [103]. In contrast, data with proximity to land are not discarded in other studies to retain a larger sample size [82]. Therefore, the limits selection is a compromise between accuracy and statistical significance. Specifically, a 10-kilometer sampling radius around and a time window of 30 minutes before and after each buoy observation are chosen. The time window is reduced to 15 minutes for the CDIP waverider buoys, which have a more frequent recording of data (every 30 minutes). These criteria fulfill the first goal since the closest distance to the coast is 13 kilometers for buoys 44039 and 44020; hence, we can find a considerable amount of collocated measurements from altimeters in these locations, and we avoid erroneous data due to land contamination. Still, the sample size of collocated data gets smaller as we are approaching the coast. On the other hand, the validity of altimeter observations inside semi-enclosed basins like, for example, the Long Island Sound or in areas surrounded by land and islands like the Nantucket Sound is one of this study's goals. Besides, it has been documented that the compared observations' spatial proximity plays a larger role than the temporal proximity [54, 67]. For the reader's convenience, we call the two buoys mentioned above as "sheltered", the buoys which are closer than 50 kilometers from land as "coastal", and the ones with a distance over 50 kilometers off the coast as "open ocean" buoys. The results presented in 4.6 are all statistically significant, and the sample size of the collocated dataset is adequate for their interpretation. We examined the option to increase the sampling radius around the open ocean buoys. Still, we decided to be consistent with the coastal and sheltered buoys and compare them using the correlation coefficient. The 30-minute time window was selected because the hourly buoy WS and SWH datasets are used for the validation and also taking into account the buoy reporting times described in 3.1.1.

The exact, great-circle distance given the buoys and the altimeter observations coordinates were calculated using the haversine formula 3.1, where θ_1, θ_2 are the latitude and ϕ_1, ϕ_2 are the longitude coordinates of the two locations in radians. The time difference is calculated using the dates and times of the reported observations. Once the sampling radius and time window limits are applied, the collocated dataset is created. The average calculated distance is 7 kilometers. This distance is acceptable, especially when the altimeter measurement principles and the effective footprint (2-7 kilometers depending on sea state) is considered. By selecting a 10-kilometer radius, one or two collocated 1Hz altimeter observations correspond to every buoy value. In the case of two collocated altimeter observations,

the first one is located north and the second south of the buoy's location. The average of the two values is calculated and then compared with a single buoy measurement.

$$D(\theta, \phi) = 2 \cdot \arcsin\left(\sqrt{\sin^2\left(\frac{\theta_2 - \theta_1}{2}\right) + \cos\theta_1 \cdot \cos\theta_2 \cdot \sin^2\left(\frac{\phi_2 - \phi_1}{2}\right)}\right) \qquad (3.1)$$

The comparison of the two datasets was performed with Ordinary least squares linear regression. The slope and the intercept of the linear model fit are reported. Evaluation of the comparison is realized by calculating commonly used pairwise metrics [26, 103] :

$$Bias = \frac{1}{N}\sum_{i=1}^{N}(A_i - B_i) \qquad (3.2)$$

$$RMSE = \sqrt{\frac{1}{N}\sum_{i=1}^{N}(A_i - B_i)^2} \qquad (3.3)$$

$$SI = \frac{\sqrt{\frac{1}{N}\sum_{i=1}^{N}\left[(A_i - \bar{A}) - (B_i - \bar{B})\right]^2}}{\bar{B}} \qquad (3.4)$$

$$R = \frac{\sum_{i=1}^{N}(A_i - \bar{A})(B_i - \bar{B})}{\sqrt{\sum_{i=1}^{N}(A_i - \bar{A})^2(B_i - \bar{B})^2}} \qquad (3.5)$$

Bias is used to assessing the systematic errors or differences between the two datasets, RMSE is the Root Mean Square Error, SI is the scatter index and R is the Pearson's Correlation Coefficient. A_i are the altimeter values, B_i are the buoy values, $\bar{A}$, $\bar{B}$ represent their corresponding mean values, and N is the collocated dataset sample size.

All calculations described above are computationally intensive due to the size of the datasets. Python library *NumPy* [47] and its vectorized operations helped to efficiently optimize all computations. Regression analysis was performed, and evaluation statistics were calculated using the Python libraries *Scikit-learn* and *SciPy* [98, 100].

3.3 Variogram Modeling and Kriging Interpolation

Variogram modeling is defined by the variogram or semivariogram estimator function, which describes a variable's correlation in space. The variogram estimator is then crucial to predicting a particular variable's values at unobserved locations and obtain information on these predictions' accuracy.

The classical variogram estimator is:

$$\gamma(h) = \frac{1}{2N(h)}\sum_{i=1}^{N(h)}(z(x_i) - z(x_i + h))^2 \qquad (3.6)$$

There are also other, more robust estimator functions that we can use like, for example, the Cressie [18], the Dowd [25], or the Genton [35] estimators. This equation's parameters will be explained based on an example using satellite altimeter data on the SNE region for the winter 2019 season. The variogram estimates (blue dots) and the corresponding model (green line), which best fits the data, are presented in Figure 3.4.

First of all, $z(x_i)$ is the observed value at point x and $z(x_i + h)$ is the observed value at a distance h from point x. This distance is called the lag interval. Lag intervals result from a process called binning, in which we classify pairs of observations in groups based on their

separation distance. Figure 3.4 shows five groups of multiples of the first lag distance of 0.4 degrees until a maximum lag distance of 2 degrees, which can be selected by the user. *N(h)* is the number of observation pairs for each lag interval and is represented by the red histogram bars. With this process, all pairs of observations are given specific values of semivariances $\gamma(h)$ on the y-axis. We use the term semivariance due to the pairs of point observations. Hence, the semivariances represent variance per observation.
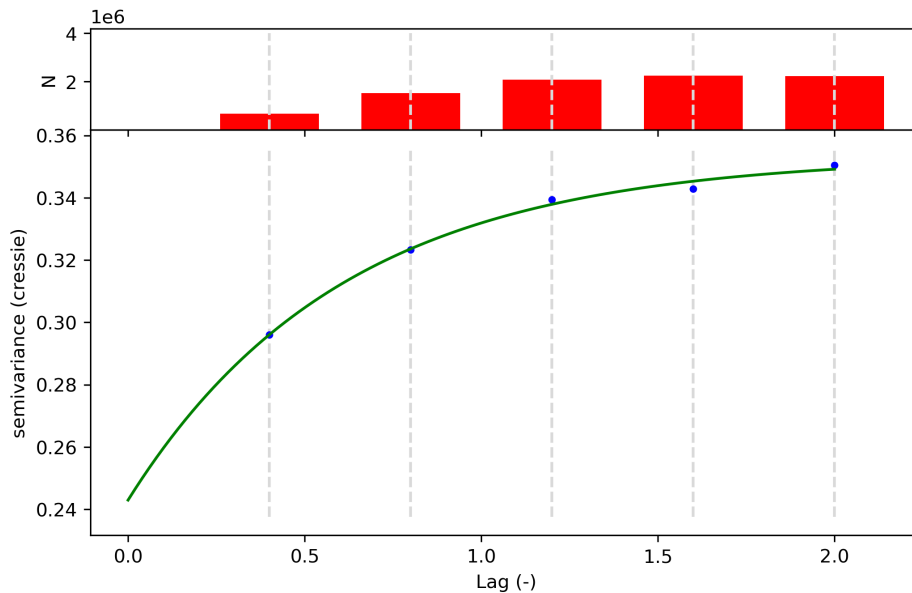
FIGURE 3.4: Variogram model for the satellite altimeter H_s data for the Winter 2019 season.

There are three fundamental parameters defined by the variogram. The first one is the sill, a variance plateau that is reached with increasing lag intervals. The sill has a value of approximately 0.11 in Figure 3.4. Specifically, it is called the partial sill in this example because there is an additional nugget effect, the second fundamental parameter of the variogram. The nugget can be observed as the y-intercept on the variogram (approximately 0.24 in Figure 3.4). It represents the minimum variance value, which exists even in zero lag interval due to small scale variations that are not captured by the large lag intervals [97]. When the nugget effect is present, the full sill is equal to the partial sill with the nugget's addition. The third variogram parameter is the range, defined as the lag distance at which the variogram reaches the sill or the partial sill if there is a nugget effect.

Once the variogram estimator function is defined, we can fit the variogram model. Certain functions can only be used as variogram models. The most commonly used is the spherical model. Other models used to fit the variogram estimator function are the exponential, linear, Gaussian, and Matern models. Both Python libraries that were used in this study, *PyKrige* [70] and *SciKit GStat* [63], provide multiple variogram estimators and models. The evaluation of each combination is performed with metrics like the correlation coefficient and RMSE and the variogram model visualization.

It is essential to mention that to perform kriging interpolation, we need to consider that the observations have to be Gaussian distributed before modeling the variogram. The variogram is sensitive to strong positive skewness resulting in higher semivariance values. Hence, if the data distribution has a long tail to the right, it is common to transform it into Gaussian using the Box-Cox transformation. An example is Figure 3.5A showing the distribution of the altimeter H_s dataset for winter 2019. Figure 3.5B shows the distribution after the Box-Cox transformation.
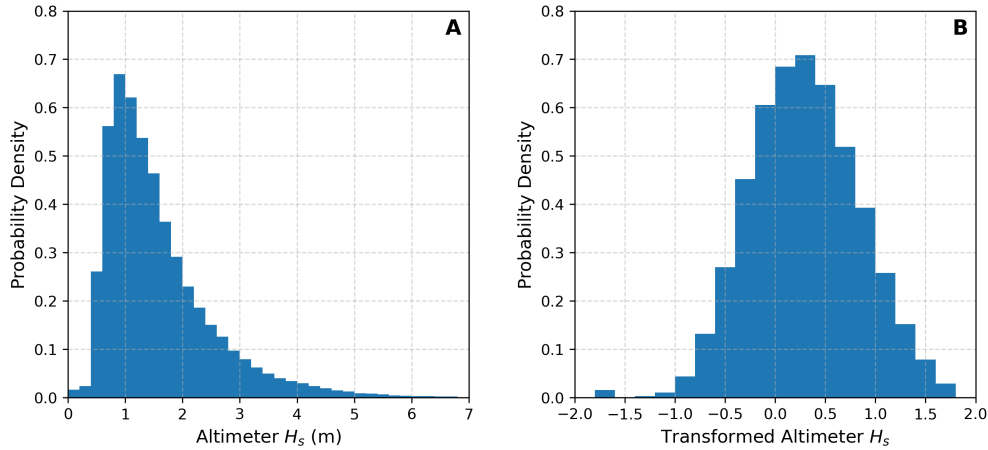
FIGURE 3.5: A. The original altimeter H_s distribution for the Winter 2018 season and B. The transformed to normal distribution for the same dataset.

After transforming the data and modeling the variogram, we can interpolate the point observations to a regular grid. There are several types of kriging interpolation, but the most common and the one that is used herein is ordinary kriging of point observations. It is based on the assumption that we do not know the variable mean. First, the weighted average of neighboring observations is calculated to estimate a variable's value in an unobserved location.

$$\hat{z}(x_0) = \sum_{i=1}^{N} \lambda_i z(x_i) \tag{3.7}$$

λ_i are the kriging weights, and the condition that applies to them is that their sum should be equal to 1 to ensure that the estimates are unbiased. The value at each grid point is accompanied by a predicted error value or the kriging variance $\sigma^2(x_0)$, and it is connected both with the variogram and the kriging weights.

$$\sigma^2(x_0) = 2 \sum_{i=1}^{N} \lambda_i \gamma(x_i, x_0) - \sum_{i=1}^{N} \sum_{j=1}^{N} \lambda_i \lambda_j \gamma(x_i, x_j) \tag{3.8}$$

$\gamma(x_i, x_j)$ is the semivariance between x_i, x_j and $\gamma(x_i, x_0)$ is the semivariance between x_i and the point we want to estimate x_0. The second condition that should be satisfied for kriging interpolation is that the estimated weights have to minimize the variances on equation 3.8. This optimization is accomplished mathematically with the inclusion of Lagrange multipliers. After the solution of a system of equations, we estimate the kriging weights. Then, we estimate the variable values at the unobserved grid point locations using 3.7 and the kriging variance for each grid point is calculated by:

$$\sigma^2(x_0) = 2 \sum_{i=1}^{N} \lambda_i \gamma(x_i, x_0) + \psi(x_0) \tag{3.9}$$

Finally, we need to emphasize the impact of the observations' relative distance on weights. First of all, nearby point observations to the unobserved locations have higher corresponding values of weights. However, when these points are concentrated in specific areas, their weights are lower with respect to those for isolated observations. Besides, increasing nugget variance in the variogram means that the weights of nearby points become smaller.

Chapter 4

Results

4.1 Wind and Wave Climatology of the SNE

The estimation of average atmospheric and marine conditions is fundamental, especially when we initially encounter the domain of interest, and we seek to describe it in terms of climatology. Identifying normal conditions is also the foundation of the study of extreme events at a later stage. For these reasons, we need a reliable and long-term record of data. In this chapter, we use the available buoy time series as described in Section 3.1.1 to provide an update for the wind and wave climate and the 2007-2019 period.

4.1.1 Diurnal Variability

Offshore wind farms are designed relatively close to the coast, at a maximum distance of 60 kilometers, due to the lower installation costs. Therefore, the wind's diurnal variability, induced by phenomena like the land-sea breeze, has to be understood [9]. The 10-minute average WS dataset is suggested to describe the variability [22] and all results presented in this section were derived using NDBC buoys' continuous winds dataset [71].

Statistics	44025	44017	44065	44020	NWPR1	44008
mean u_{10} (m/s)	9	9.18	8.51	8.2	4.83	9.09
max. u_{10} (m/s)	9.34	9.49	8.82	8.49	5.36	9.35
min. u_{10} (m/s)	8.48	8.77	7.93	7.8	4.48	8.84
time of max. u_{10}	00:40	02:00	07:10	23:00	14:24	20:50
time of min. u_{10}	15:30	13:50	13:40	13:40	06:00	10:10
u_{10} diur. range (m/s)	0.86	0.72	0.89	0.69	0.88	0.51
mean wind dir. (deg)	293.2	284.4	285.3	283.1	317.2	289.3
max. wind dir. (deg)	306.2	295.1	294.6	295.5	329.8	300.6
min. wind dir. (deg)	279.5	270.5	273	271.9	297.6	279.9
time of max. wind dir.	07:30	05:00	09:50	06:50	05:12	05:50
time of min. wind dir.	17:20	15:30	18:50	16:00	17:30	16:00
wind dir. diur. range (deg)	26.7	24.7	21.6	23.7	32.2	20.7

TABLE 4.1: NDBC Buoys & Station NWPR1 (Newport, RI) u_{10} and wind direction winter diurnal variability statistics including mean, minimum, maximum values, the diurnal range and the times when the minimum and maximum values are observed.

Since buoy time series are disseminated in UTC, first, we need to convert the time zone to local US Eastern time. The advective effects become more substantial with closer proximity to land. Thus, for this section, data from an additional meteorological station (NWPR1) at Newport, Rhode Island (41.504°N, 71.326°W), are used to compare the diurnal variability

in its location with the buoys'. This coastal station is maintained by NOAA and is located on land. The anemometer height is 8.4 meters; hence, we need to make a small adjustment to the reference height of 10 meters to compare with the buoys. The average u_{10} and wind direction is calculated for the 2007-2019 period. The 10-minute average dataset is used for the NDBC buoys and 6-minute average values for station NWPR1. We use the circular mean [91], not the arithmetic mean for the wind direction calculations. Data are grouped in mean values every 10 minutes for the buoys and every 6 minutes for station NWPR1 for the winter and summer seasons separately. Then these grouped values are subtracted from the 24-hour, seasonal mean for each buoy and station. The final time series represent the diurnal residuals. Figures 4.1, 4.2 show the diurnal residuals and their corresponding confidence intervals. Tables 4.1, 4.2 provide a summary of the calculations for the winter and summer seasons, including minimum and maximum values of the residuals and the times they occur during the day. The u_{10}, and wind direction diurnal range is the difference between the reported minimum and maximum residuals and characterizes the diurnal variability for each location. Figure 4.3 shows the diurnal range for all stations' locations with respect to their proximity to the coast.

Statistics	44025	44017	44065	44020	NWPR1	44008
mean u_{10} (m/s)	5.54	5.45	5.38	6.11	3.55	4.72
max. u_{10} (m/s)	6	5.81	6.35	6.65	5	4.83
min. u_{10} (m/s)	5.04	5.07	4.52	5.66	2.62	4.6
time of max. u_{10}	20:30	18:00	18:20	17:30	15:18	14:30
time of min. u_{10}	12:20	12:00	11:30	10:40	05:30	19:50
u_{10} diur. range (m/s)	0.96	0.74	1.83	0.99	2.39	0.23
mean wind dir. (deg)	208.1	221.7	206.6	215.7	222.4	202.5
max. wind dir. (deg)	261.8	252.8	270.5	246.6	303.1	216.7
min. wind dir. (deg)	186.8	203.5	178.2	190.3	209.4	190.7
time of max. wind dir.	08:00	06:20	07:20	08:10	06:12	04:20
time of min. wind dir.	17:50	15:20	15:00	15:50	21:12	20:40
wind dir. diur. range (deg)	75	49.3	92.3	56.3	93.6	25.9

TABLE 4.2: NDBC Buoys & Station NWPR1 (Newport, RI) u_{10} and wind direction summer diurnal variability statistics including mean, minimum, maximum values, the diurnal range and the times when the minimum and maximum values are observed.

The results from station NWPR1 indicate a u_{10} diurnal range over 2m/s during the summer months. This result is even more significant if we consider the WS's low average values at this location (3.55 m/s). During summer, the lowest WS values are observed in the early morning hours (5:30 AM), and the maximum is reached in the afternoon (3:18 PM). The winter minimum and maximum reported times are almost synchronous to the respective during summer. The maximum wind intensity occurs one hour earlier during the winter. The summer diurnal range is nearly three times more than the winter value, 2.39m/s, and 0.88m/s correspondingly. The wind gradually changes its direction from southwest to the northwest at 6:12 PM, which almost coincides with the minimum WS. It then reverses back to the southwest direction at noon and stays virtually constant until 2:00 AM. During winter, the wind is coming mainly from the northwest, and the diurnal range is relatively small (32 degrees).
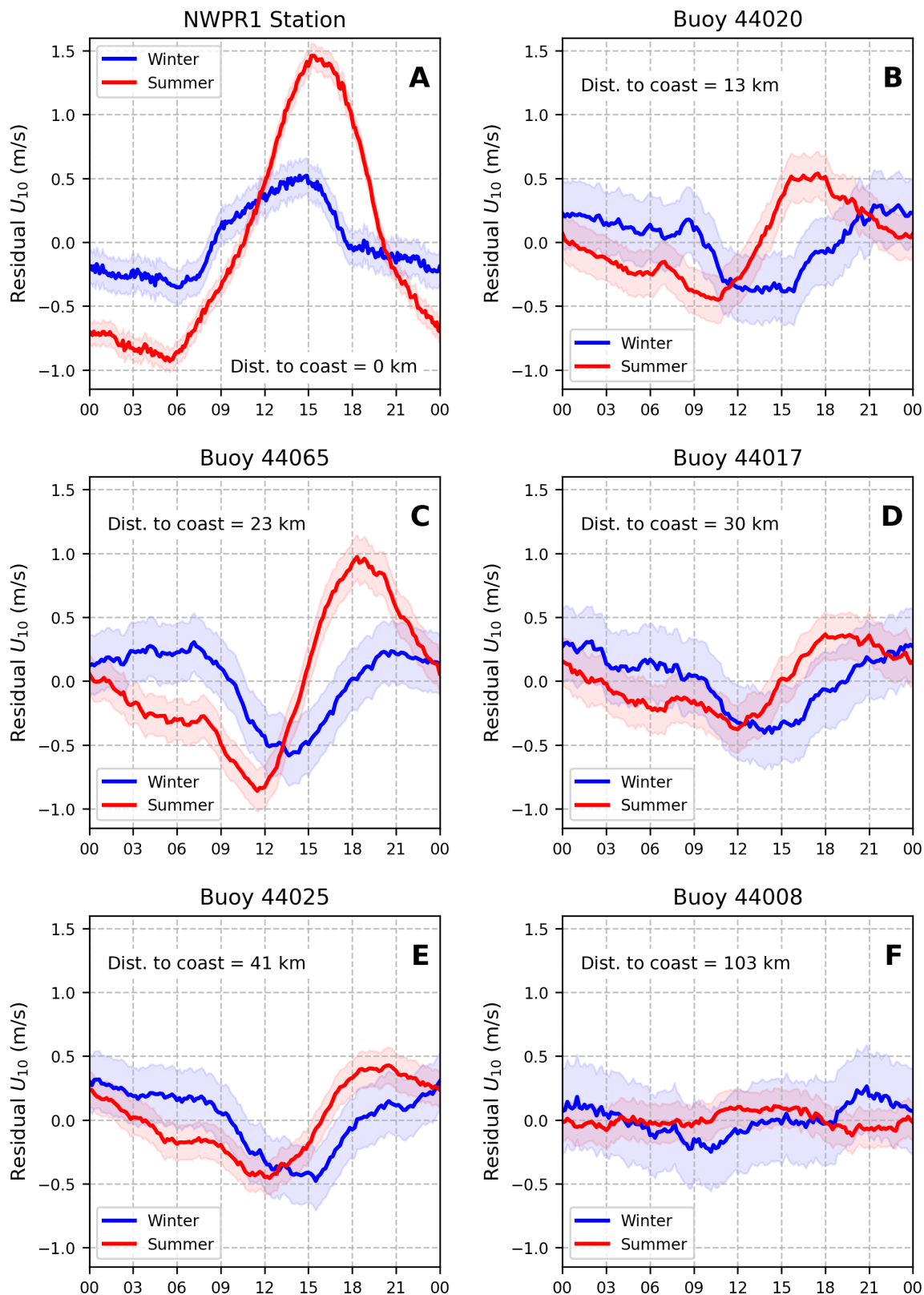
FIGURE 4.1: NDBC Buoys & Station NWPR1 (Newport, RI) u_{10} diurnal cycle
for the winter and summer seasons.
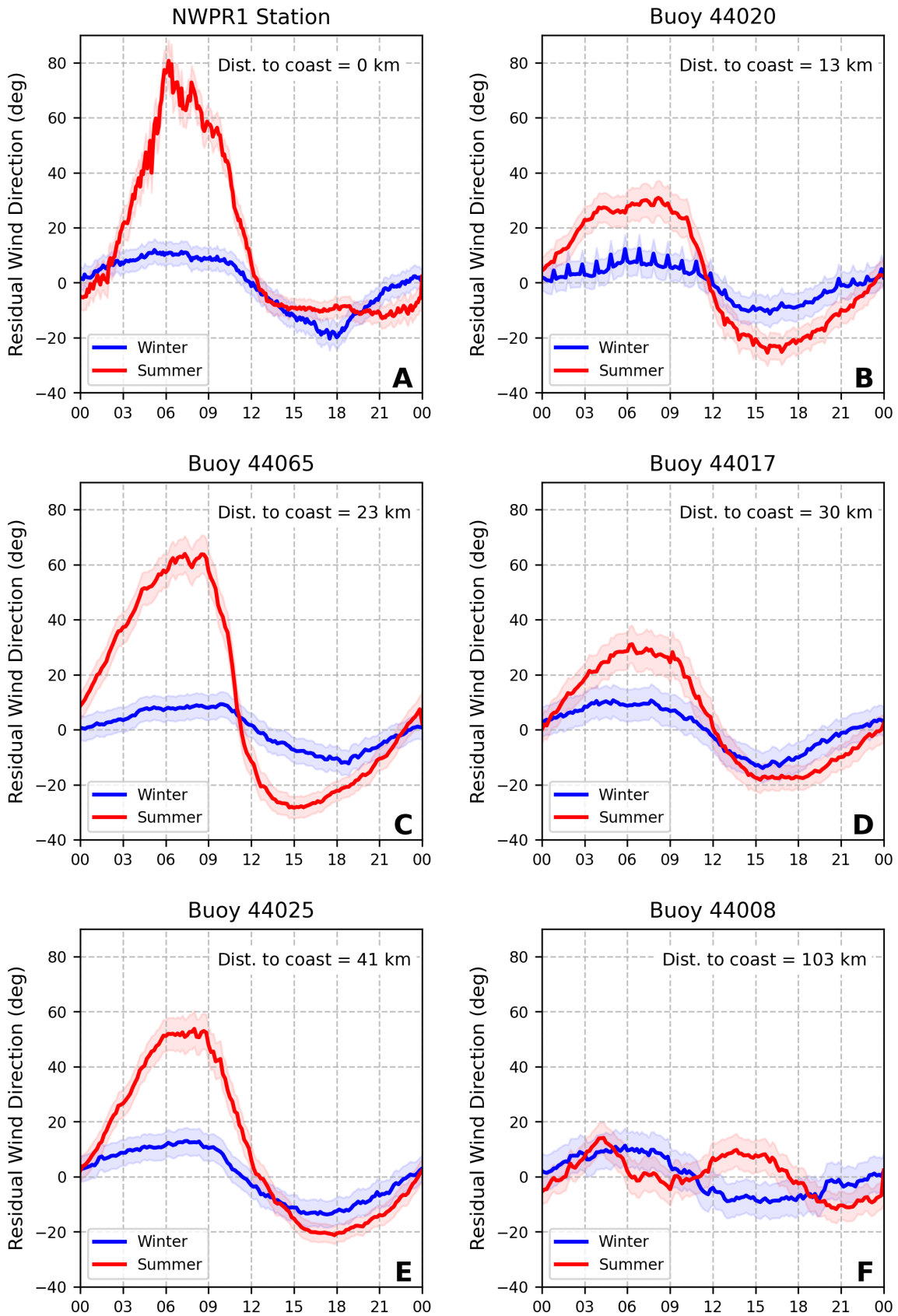
FIGURE 4.2: NDBC Buoys & Station NWPR1 (Newport, RI) wind direction diurnal cycle for the winter and summer seasons.

The diurnal cycles of the buoys located kilometers offshore reveal different attributes. The western part of the region presents the highest diurnal range, specifically at the coastal buoy 44065 location, 23 kilometers from the closest shore and southwest of Long Island. Therefore, both the proximity to land and the topography surrounding each buoy's location has to be considered. As we move further off the coast and to the eastern part of the region, the diurnal range differences for u_{10} and wind direction between summer and winter are not as significant as for station NWPR1. The uncertainty of the estimations also becomes higher. Besides, the WS diurnal cycle is not synchronous with the wind direction diurnal cycle. Generally, the lowest WS values are identified between 10:30 AM and 12:30 PM during the summer and the highest in the evening between 5:30 PM and 8:30 PM. On the other hand, minimum WS values are found during winter between 1:30 PM and 3:30 PM and the maximum in the early morning hours. There are also local wind speed maxima between 6:00 and 9:00 AM, which are apparent in Figures 4.1B and 4.1C. The diurnal range is more extensive during summer, and it can reach up to 2m/s. Maximum WS values are observed earlier at stations with closer proximity to the land. On the contrary, buoys' winter diurnal cycle is almost the reverse of the NWPR1 station. Specifically, buoys' minimum WS values are reported between 12:00 and 3:00 PM, the same hours of maximum WS observed on land. In contrast, the wind direction's diurnal cycle for each location coincides.

However, the above description does not include buoy 44008. Figures 4.1F and 4.2F confirm that the advective effects do not appear to influence locations 100 kilometers off the closest coast, where the diurnal range is almost negligible. Therefore, it may be concluded that generally, the diurnal variability has to be considered at distances less than 40 kilometers from the land. Still, it becomes weak at 100 kilometers or more offshore, especially on the eastern side of SNE.

Finally, the diurnal variability of the wind does not affect the wave climate significantly. The diurnal range of the SWH is in the order of centimeters (not shown here). Besides, we did not identify any significant influence on the directional spectra's diurnal variability for buoy 44097.
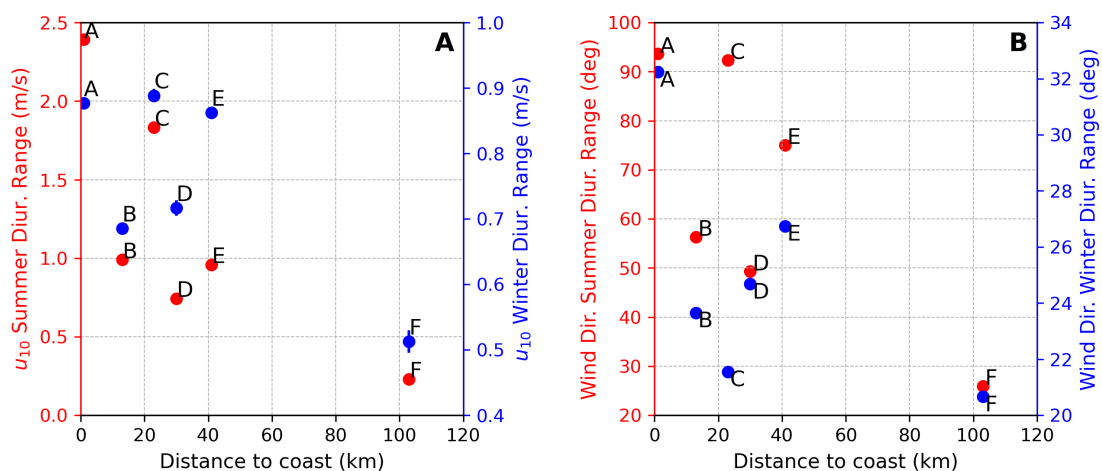
FIGURE 4.3: NDBC Buoys and NWPR1 station wind speed and direction diurnal range with respect to their distance from the closest coast.

4.1.2   Seasonal Variability

The seasonal variability of both the H_s and the u_{10} will be characterized in this study for SNE, a North Atlantic coastal region, using buoy data. Young [104] documented the North Atlantic wind and wave climate's strong seasonal trends using altimeter data and numerical models. He also emphasized that the extended NDBC buoy network is suitable for regional studies.

Figure 4.4 shows the u_{10} seasonal variability for six of the available buoys, including the daily mean values, their 25th, 75th percentiles, and a monthly lowpass filter to visualize the seasonality. Both Figure 4.4 and the average u_{10} values available in tables 4.3, 4.4 display that the seasonal variability ranges from 2m/s for the sheltered buoy 44020 to almost 4.5 m/s for the open ocean buoy 44008. Figure 4.5 shows similar results for the H_s. Buoys 44020 and 44065 that are closer to the coast show almost zero seasonal variability. Buoy 44039, located in the Long Island Sound, shows stronger seasonal variability with lower WS values on average than buoy 44020, even if they have the same distance to the coast. On the contrary, at over 100 kilometers from the coast, buoy 44008 presents a strong seasonal variability of approximately 1.3 meters on average. This difference is only partly explained by the direct influence of the wind on the sea surface. We show in 4.4 that the percentage of purely wind waves at the buoy 44008 location is small, especially during the summer season, and the opposite applies for the sheltered buoy 44020. Therefore, the strong seasonal variability in the open ocean buoy's location is also connected with the North Atlantic variability trend described by Young. In contrast, buoy 44020 is located 13 kilometers from the closest coast, where there is a low presence of swell waves due to topography. Finally, we can identify local minima during the first days of December for both u_{10} and H_s (Figure 4.5F) and also local H_s maxima between July and August.
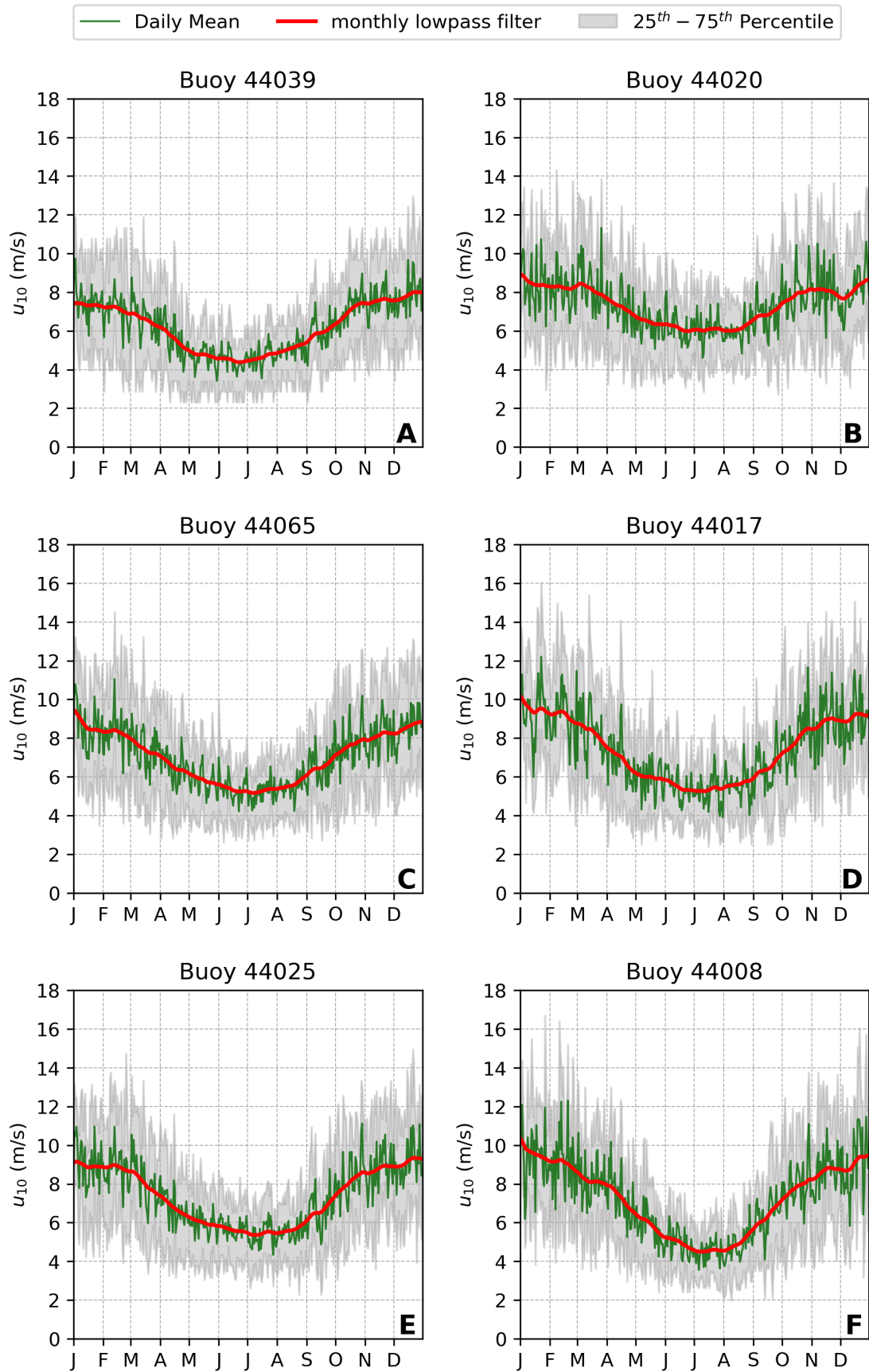
FIGURE 4.4: Buoy u_{10} seasonal variability
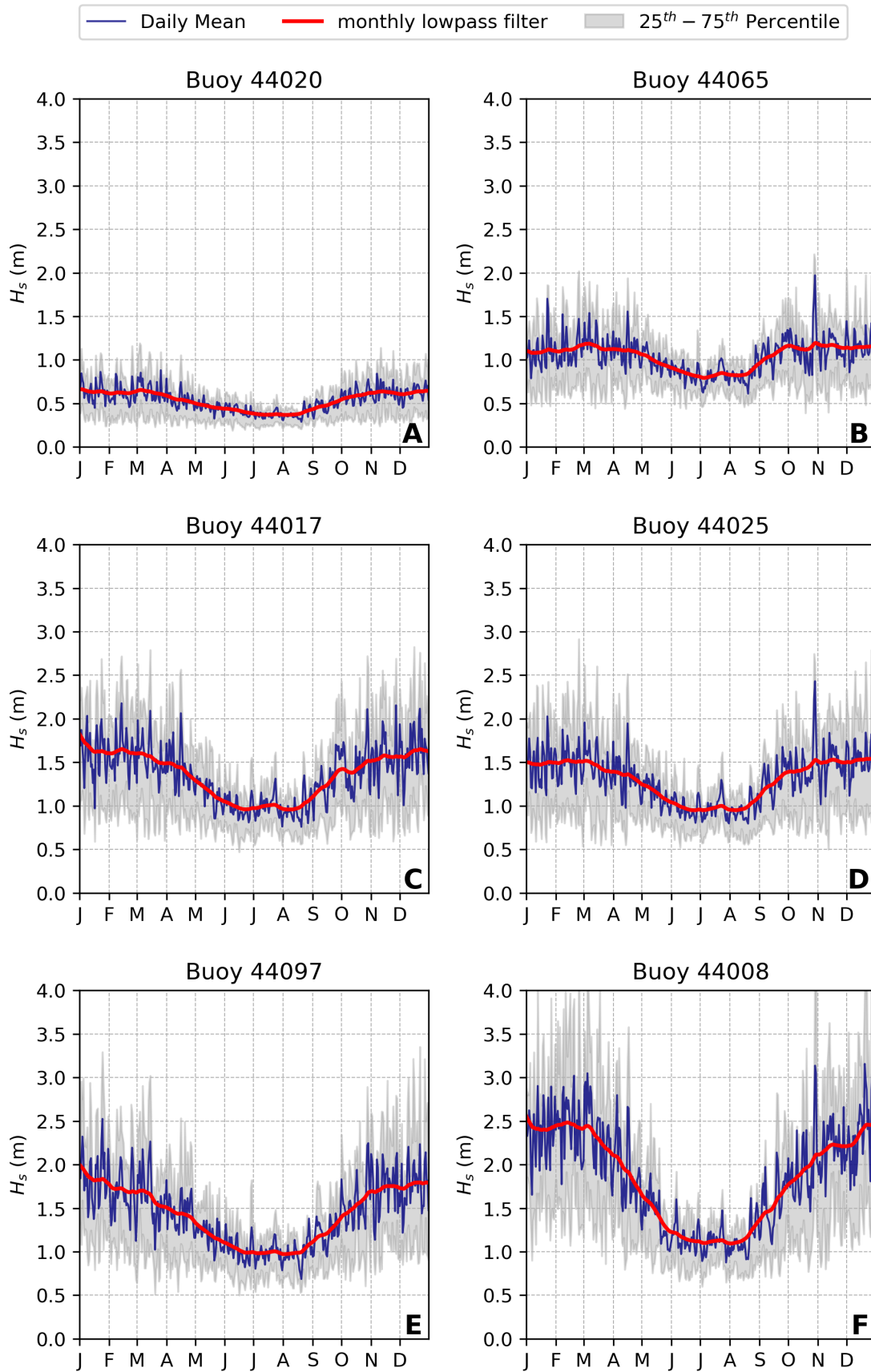
FIGURE 4.5: Buoy H_s seasonal variability

4.1.3 Interannual Variability

The interannual variability is essential for detecting anomalies, trends, and the representation of climatic averages. Due to gaps in the buoy time series, months with less than 50% of data availability were discarded.
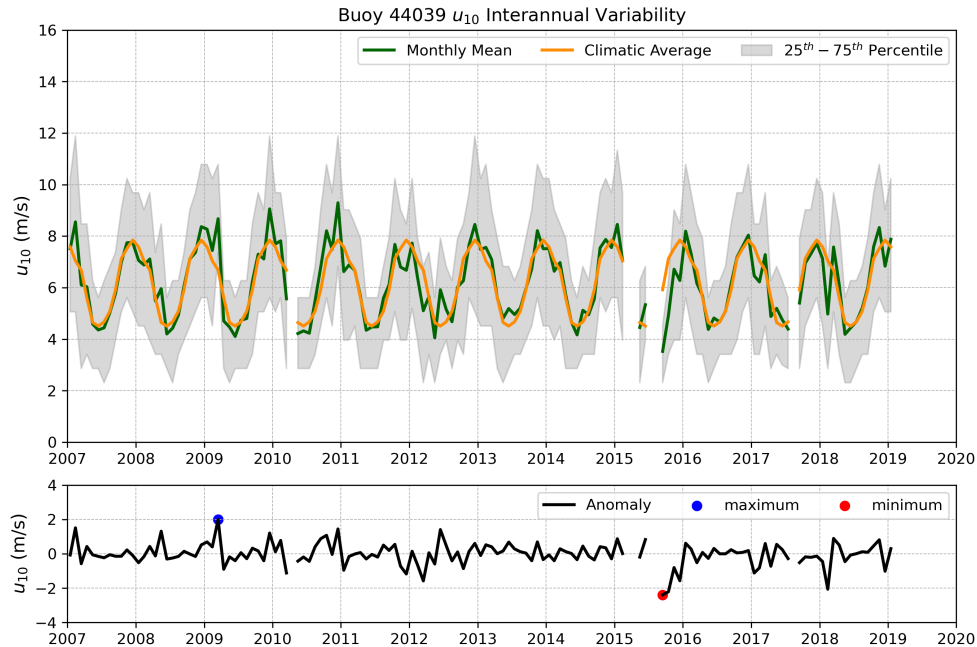
FIGURE 4.6: Buoy 44039 u_{10} interannual variability including monthly mean values, 25th and 75th percentiles, climatic average and monthly anomalies.
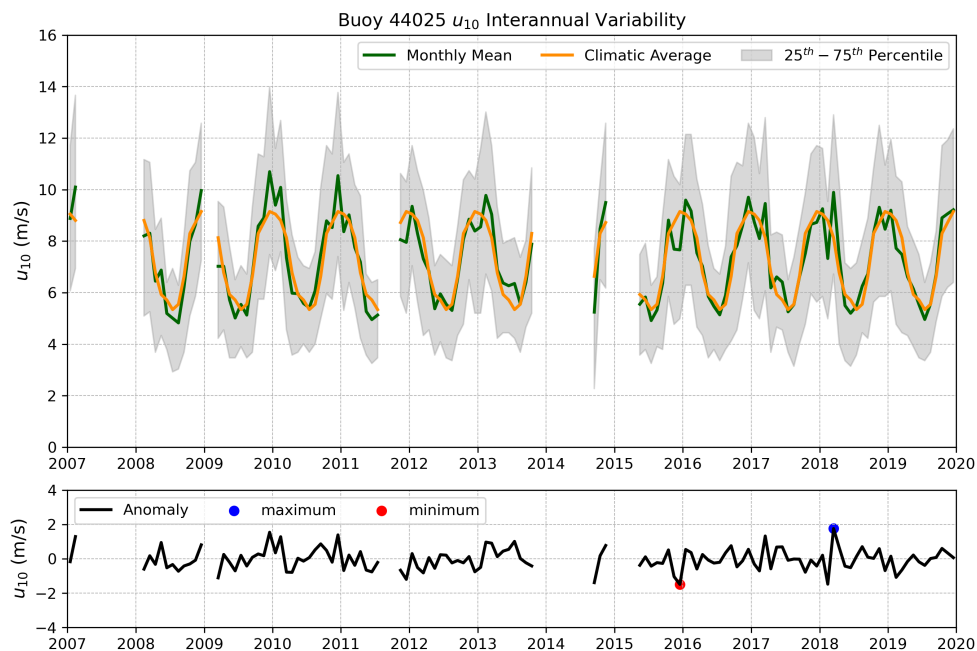
FIGURE 4.7: Buoy 44025 u_{10} interannual variability including monthly mean values, 25th and 75th percentiles, climatic average and monthly anomalies.

Statistically significant trends were not identified for H_s and u_{10} both for the winter and summer seasons. Two methods were used: linear regression analysis and calculating the

regression slope and the Mann-Kendall and seasonal Mann-Kendall trend test [53].
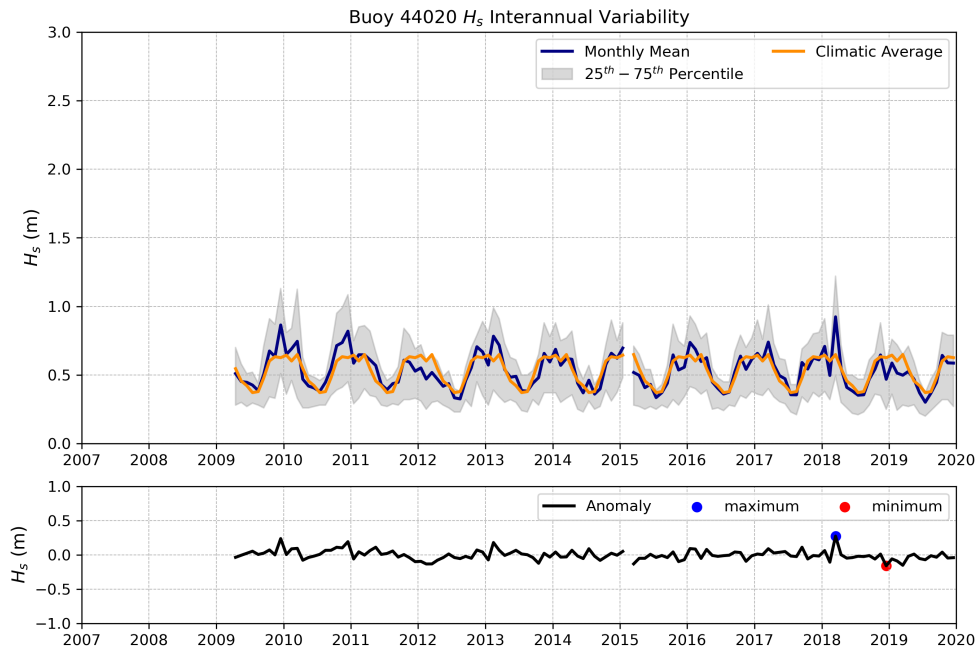
FIGURE 4.8: Buoy 44020 u_{10} interannual variability including monthly mean values, 25th and 75th percentiles, climatic average and monthly anomalies.
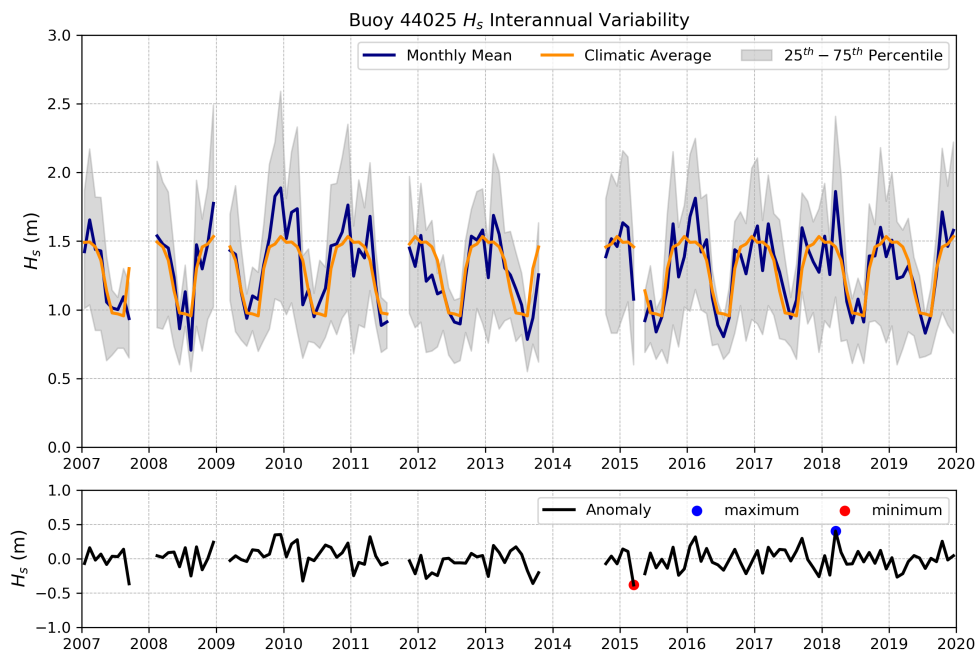
FIGURE 4.9: Buoy 44025 u_{10} interannual variability including monthly mean values, 25th and 75th percentiles, climatic average and monthly anomalies.

Data gaps and the relatively small number of years with available data for almost all stations were limiting factors to achieve statistical significance. For completeness, the interannual variability of H_s and u_{10} for the buoys with small gaps in their time series are

included in this section. In recent literature, data from long-term altimeter records and numerical models are not indicating statistically significant trends on the Northeast Atlantic coasts either [66, 95].

A feature that requires attention is the double peaks from late autumn to early spring, especially when considering the H_s figures. For example, the double peaks in Figure 4.11 can be assessed considering the monthly average wave spectrum of the same buoy in Figure 4.16.
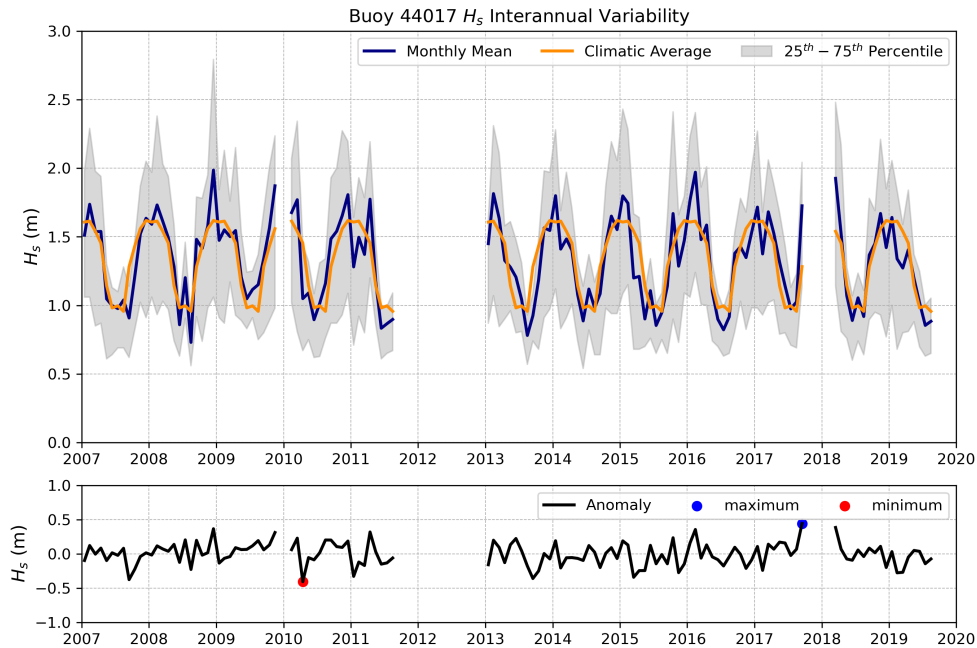
FIGURE 4.10: Buoy 44017 u_{10} interannual variability including monthly mean values, 25th and 75th percentiles, climatic average and monthly anomalies.
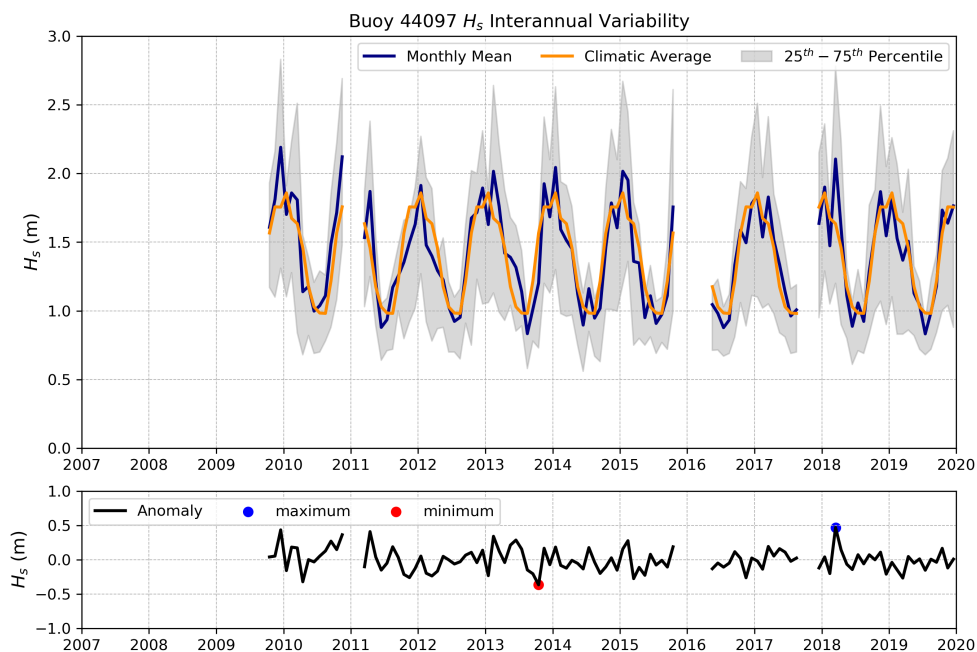
FIGURE 4.11: Buoy 44097 u_{10} interannual variability including monthly mean values, 25th and 75th percentiles, climatic average and monthly anomalies.

Specifically, double peaks appear regularly due to the southeastern swell system with the highest energy in March and November combined with the sea states' lower energy density during February and secondarily January. However, there are not available wind data for this station for further assessment. Judging from Figure 4.7, double peaks exist in the u_{10} winter monthly means. Multiple winter peaks also appear in the corresponding H_s Figure 4.9 for buoy 44025. Finally, the local H_s maxima during the summer months described in 4.1.2 is also present in the interannual variability figures and the monthly mean time series.

4.1.4   Wind and Wave Directional Distribution

The directional distribution of WS and SWH provides us with necessary information on the origin of winds and waves and also their magnitude in each direction. For the WS, the statistical distribution and visualization with a wind rose are adequate to assess the wind direction regime. On the other hand, wave distribution also requires more elaborate analysis due to multiple wave systems present.

The WS and SWH directional distribution tables and figures include only winter and summer data, and the directional spectra include all available data for the 2007-2019 period. Data from seven buoys were used for the analysis of joint WS and wind direction. Eight buoys record both SWH and mean wave direction data, and they were used for the SWH directional wave distribution. Six buoys are common for wind and wave analysis, buoy 44039 misses wave direction, and the two CDIP buoys (44097 and 44091) do not record wind data. The eight main directions from where the wind and waves are coming from were chosen, each with an angular window of 45 degrees. After grouping the data in these directions, the frequency of occurrence, the u_{10}, H_s average and standard deviation for each direction separately, and including all of them collectively were calculated. The results are presented in tables 4.3 - 4.6.

The buoy wind data exhibit homogeneous characteristics during the winter and summer seasons. During winter, over 50% of the observations reveal a wind direction from the west and northwest. The wind is also strongest from these directions. Buoy 44066, the most remote of all stations and located at the western side of SNE, shows the highest average WS values. The sheltered buoy 44020 reports the lowest wind intensity on average. The standard deviation of the WS is highest from the northeastern direction. During summer, the wind shifts to the south, with over 50% of observations showing wind direction from the west and southwest for each station. The strongest winds during summer are coming from the northeast, and the standard deviation is also higher for the northeastern winds. Buoy 44020 location is the one with the highest average WS value during summer, and it is expected due to the low seasonal variability, as we previously showed in 4.1.2. The reverse is true for buoy 44008, which has the lowest summer WS average, along with buoy 44039, due to high seasonal variability.

In contrast, the waves are not as coherent with respect to their directional distribution, especially during winter. Three parameters impose challenges to predict and characterize the wave climate during winter; strong winds, more frequent low-pressure systems passing over the region, and swell waves reaching SNE from distant North Atlantic storms. All the above lead to the broader spreading of the sea state to more directions and dictate the further investigation of the wave climate using the directional spectrum. Nevertheless, during winter, the wind's impact is most substantial to waves at the buoy 44020 location, to which they are coming from the west and secondarily from the northwest. There is a small influence of swell waves coming from the east in this location. During summer, waves are more coherent, and their dominant directions for most stations are the south and southeast for approximately 60% of the observations. The only exception is again buoy 44020, to where

swells are coming from the east, and the wind waves follow the direction of the wind coming from the southwest.

Buoy	Statistics	N	NE	E	SE	S	SW	W	NW	uni
	Frequency (%)	11.3	7.43	6.15	4.48	8.52	13.83	20.92	27.37	100
44025	Average (m/s)	8.08	8.05	8.24	6.84	7.6	8.02	9.86	10.43	9
	St. Dev. (m/s)	3.79	4.57	4.08	3.78	3.6	3.37	4.08	3.92	4.08
	Frequency (%)	8.93	6.5	6.66	4.83	6.36	14.08	29.5	23.14	100
44017	Average (m/s)	8.1	8.81	9.19	7.29	7.87	8.54	10.17	9.56	9.18
	St. Dev. (m/s)	4.05	4.99	4.13	3.38	3.71	3.53	3.94	3.65	3.98
	Frequency (%)	9.6	7.67	5.24	3.28	10.25	12.9	26.03	25.02	100
44065	Average (m/s)	7.73	8.32	7.36	5.65	7.31	6.95	9.36	9.9	8.51
	St. Dev. (m/s)	3.61	4.13	4.05	3.69	3.37	3.18	3.83	3.87	3.93
	Frequency (%)	11	5.41	5.81	5.13	6.85	13.03	29.95	22.83	100
44020	Average (m/s)	8.04	8.11	8.08	6.64	6.88	7.13	8.63	9.12	8.2
	St. Dev. (m/s)	4.18	4.98	4.01	3.56	3.69	3.13	3.75	3.61	3.86
	Frequency (%)	11.16	6.91	6.67	6.91	8.13	13.37	21.63	25.22	100
44008	Average (m/s)	8.9	8.16	8.13	7.49	7.92	8.48	10.1	9.94	9.09
	St. Dev. (m/s)	4.47	4.74	3.84	3.61	3.74	3.87	4.36	4.01	4.22
	Frequency (%)	13.95	6.09	8.67	3.78	6.43	11.29	26.57	23.23	100
44039	Average (m/s)	6.82	6.47	7.22	5.5	5.31	6.24	8.32	8.39	7.38
	St. Dev. (m/s)	3.2	3.4	3.8	3.48	3.37	3.07	3.59	3.34	3.57
	Frequency (%)	10.77	7.24	5.35	4.81	7.34	13.94	22.47	28.07	100
44066	Average (m/s)	8.45	8.85	8.41	7.89	8.01	9.23	10.52	10.34	9.52
	St. Dev. (m/s)	4.22	4.98	4.36	3.98	3.80	3.79	4.04	3.74	4.13

TABLE 4.3: Directional Distribution of winter u_{10} frequency, average and standard deviation using buoy data.
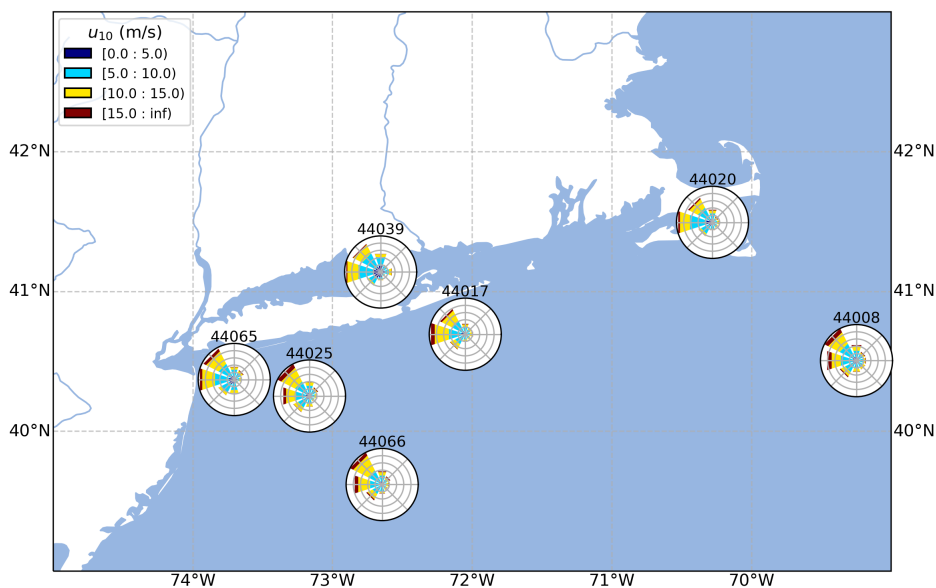
FIGURE 4.12: Buoy wind rose map for the winter season.

Buoy	Statistics	N	NE	E	SE	S	SW	W	NW	uni
	Frequency (%)	6.22	8.42	9.32	8.08	19.95	29.6	11.03	7.38	100
44025	Average (m/s)	5.3	6.25	5.6	4.54	5.62	5.93	4.81	5.22	5.54
	St. Dev. (m/s)	2.82	3.19	2.85	2.3	2.38	2.41	2.15	3.84	2.6
	Frequency (%)	5.11	7.27	7.67	7.36	14.28	37.35	13.57	7.39	100
44017	Average (m/s)	5.42	6.97	6.26	4.7	4.88	5.9	4.83	5.12	5.54
	St. Dev. (m/s)	2.88	3.69	3.19	2.51	2.31	2.29	2.17	2.68	2.64
	Frequency (%)	6.02	6.7	8.63	8.21	28.54	19.46	13.34	9.09	100
44065	Average (m/s)	5.21	5.98	5.77	4.6	6.04	4.96	4.55	5.41	5.38
	St. Dev. (m/s)	2.71	3.03	2.8	2.24	2.49	2.14	2.12	2.71	2.53
	Frequency (%)	7.22	9.22	8.77	7.11	15.68	35.88	10.63	5.49	100
44020	Average (m/s)	5.86	6.16	5.05	5.22	6.3	6.68	5.62	5.87	6.11
	St. Dev. (m/s)	3	2.92	2,67	2.94	2.84	2.41	2.7	2.99	2.76
	Frequency (%)	8.37	10.81	8.49	10.16	21.02	23.05	10.67	7.44	100
44008	Average (m/s)	4.93	5.6	4.71	4.31	4.62	4.77	4.29	4.61	4.73
	St. Dev. (m/s)	2.82	2.98	2.69	2.34	2.24	2.14	2.15	2.63	2.46
	Frequency (%)	8.14	5.98	12.35	6.77	18.45	22.91	17.35	8.05	100
44039	Average (m/s)	4.57	4.87	5.22	4.39	4.7	4.74	4.37	4.62	4.69
	St. Dev. (m/s)	2.34	2.68	2.74	2.43	2.2	2.07	2.1	2.45	2.32
	Frequency (%)	7.18	9.79	8.63	7.5	16.63	29.8	12.74	7.76	100
44066	Average (m/s)	6.05	6.55	5.55	4.9	5.51	6.24	5.02	5.16	5.74
	St. Dev. (m/s)	3.34	3.21	3.06	2.58	2.46	2.47	2.34	2.81	2.75

TABLE 4.4: Directional Distribution of summer u_{10} frequency, average and standard deviation using buoy data.
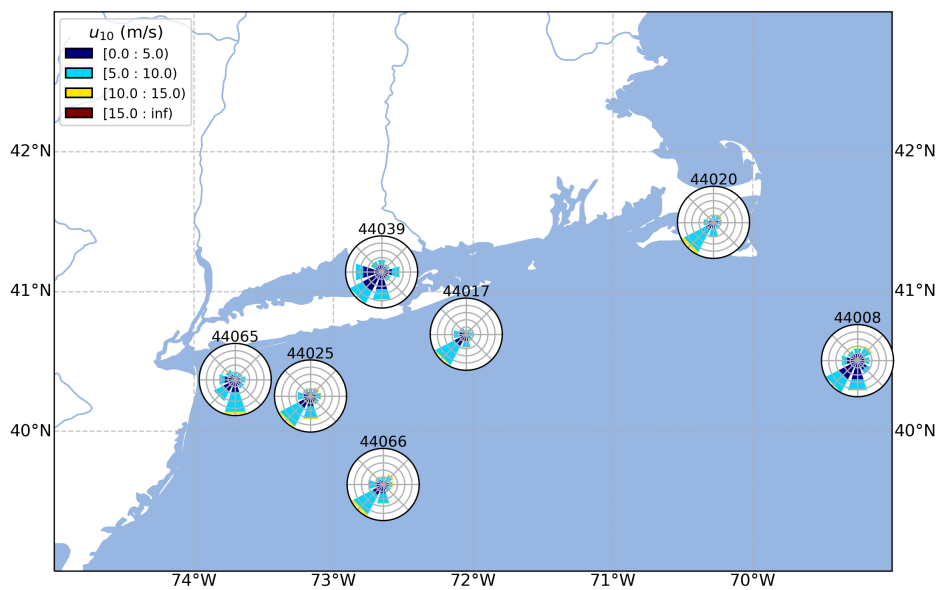
FIGURE 4.13: Buoy wind rose map for the summer season.

Buoy	Statistics	N	NE	E	SE	S	SW	W	NW	uni
	Frequency (%)	2.41	3.08	16.54	20.97	18.67	7.03	22.83	8.45	100
44025	Average (m)	1.24	1.24	1.59	1.42	1.53	1.33	1.65	1.46	1.51
	St. Dev. (m)	0.77	0.85	1.04	0.94	0.76	0.66	0.71	0.67	0.84
	Frequency (%)	1.95	3.56	14.44	22.09	22.84	24.56	5.87	4.7	100
44017	Average (m)	1.09	1.4	1.65	1.57	1.79	1.66	1.36	1.3	1.61
	St. Dev. (m)	0.48	0.81	0.98	1	0.88	0.77	0.68	0.54	0.88
	Frequency (%)	1.82	0.84	18.88	30.98	20.35	1.79	7.9	17.45	100
44065	Average (m)	0.88	0.81	1.28	1.11	1.1	0.8	1.13	1.07	1.12
	St. Dev. (m)	0.5	0.47	0.81	0.68	0.54	0.43	0.48	0.43	0.63
	Frequency (%)	6.81	6.74	20.71	4.3	4.69	6.23	37.23	13.29	100
44020	Average (m)	0.78	0.86	0.57	0.63	0.61	0.56	0.72	0.76	0.69
	St. Dev. (m)	0.46	0.57	0.33	0.36	0.31	0.24	0.32	0.38	0.37
	Frequency (%)	7.01	9.5	12.98	9.5	19.25	19.14	16.29	6.34	100
44008	Average (m)	2.13	2.36	2.11	1.88	2.65	2.46	2.5	2.46	2.37
	St. Dev. (m)	1.18	1.49	1.23	1.18	1.39	1.18	1.15	1.28	1.28
	Frequency (%)	4.99	3.18	4.5	18.76	22.31	21.05	17.16	8.05	100
44097	Average (m)	1.46	1.73	1.73	1.46	1.83	1.99	1.87	1.69	1.76
	St. Dev. (m)	0.76	0.94	0.93	0.88	1.06	1.01	0.82	0.72	0.95
	Frequency (%)	11.23	4.2	27.32	20.78	20.14	4.88	5.01	6.44	100
44091	Average (m)	1.29	1.63	1.52	1.24	1.45	1.18	1.43	1.43	1.4
	St. Dev. (m)	0.56	1.02	1.01	0.65	0.61	0.47	0.51	0.54	0.76
	Frequency (%)	5.37	5.88	18.17	13.37	17.21	8.08	11.45	20.48	100
44066	Average (m)	1.62	2.57	1.75	1.55	2	1.97	2.23	2.05	1.94
	St. Dev. (m)	0.99	1.79	1.06	1	1.06	0.9	1.06	0.99	1.11

TABLE 4.5: Directional Distribution of winter H_s frequency, average and standard deviation for NDBC Buoys and Stations
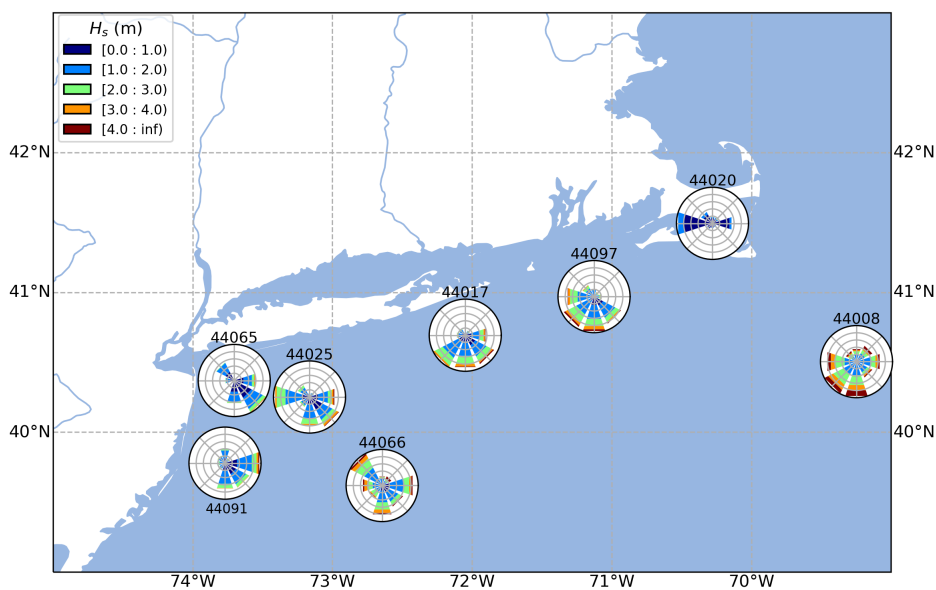
FIGURE 4.14: Winter wave rose map for NDBC buoys

Buoy	Statistics	N	NE	E	SE	S	SW	W	NW	uni
44025	Frequency (%)	0.59	1.84	16.35	34.47	37.19	7.25	1.62	0.69	100
	Average (m)	0.93	1.1	1.05	0.87	1.02	0.99	0.89	0.88	0.97
	St. Dev. (m)	0.26	0.42	0.52	0.4	0.38	0.35	0.29	0.29	0.41
44017	Frequency (%)	0.31	1.88	12.65	32.94	39.49	11.9	0.57	0.27	100
	Average (m)	0.87	1.23	0.98	0.9	1.05	0.99	0.77	0.88	0.99
	St. Dev. (m)	0.31	0.46	0.43	0.42	0.43	0.34	0.24	0.23	0.42
44065	Frequency (%)	0.3	0.48	15.23	43.98	37.35	1.17	0.27	1.22	100
	Average (m)	0.75	0.72	0.91	0.78	0.87	0.82	0.73	0.75	0.83
	St. Dev. (m)	0.18	0.26	0.41	0.34	0.34	0.36	0.39	0.21	0.36
44020	Frequency (%)	7.91	9.4	20.32	8.05	11.11	18.31	17.81	7.08	100
	Average (m)	0.44	0.56	0.4	0.44	0.47	0.46	0.46	0.43	0.45
	St. Dev. (m)	0.21	0.3	0.18	0.23	0.19	0.16	0.16	0.18	0.2
44008	Frequency (%)	1.37	4.54	17.93	24.02	34.62	14.45	2.78	0.29	100
	Average (m)	1.23	1.35	1.08	0.97	1.21	1.25	1.06	1.1	1.14
	St. Dev. (m)	0.43	0.62	0.5	0.45	0.53	0.6	0.35	0.4	0.53
44097	Frequency (%)	0.57	1.51	2.57	28	38.6	23.88	4.23	0.64	100
	Average (m)	1.09	1.19	1.17	0.86	0.98	1.16	1.01	0.96	1
	St. Dev. (m)	0.33	0.3	0.51	0.38	0.39	0.53	0.35	0.29	0.44
44091	Frequency (%)	1.78	1.78	26.02	29.97	36.51	3.16	0.13	0.65	100
	Average (m)	0.97	1.35	1.05	0.88	1.01	0.91	1.07	0.97	0.99
	St. Dev. (m)	0.56	1.02	1.01	0.65	0.61	0.47	0.51	0.54	0.76
44066	Frequency (%)	1.07	3.18	17.81	27.61	31.59	14.79	1.66	2.29	100
	Average (m)	1.08	1.44	1.12	0.84	1.13	1.11	1	1.21	1.05
	St. Dev. (m)	0.32	0.56	0.49	0.37	0.35	0.26	0.39	0.28	0.4

TABLE 4.6: Directional Distribution of summer H_s frequency, average and standard deviation for NDBC Buoys and Stations
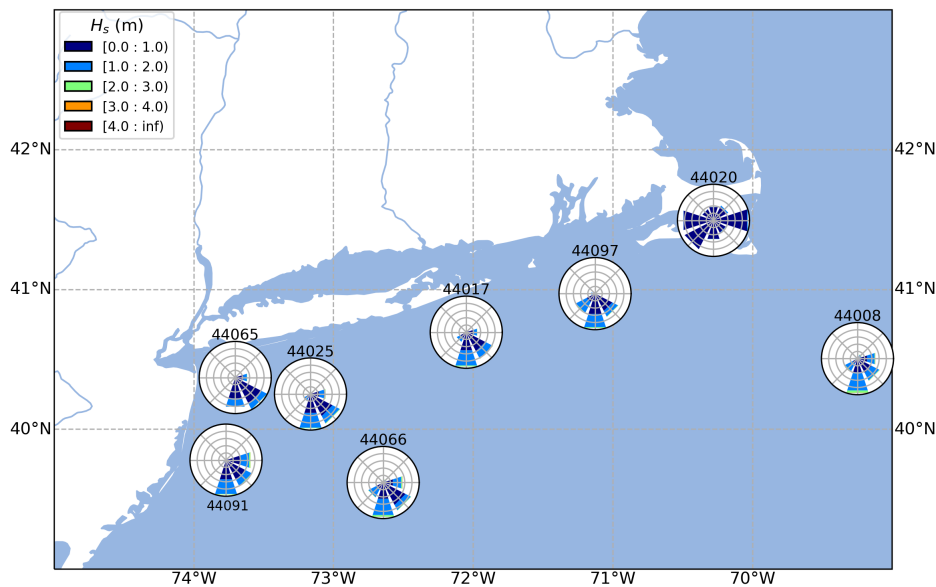
FIGURE 4.15: Summer wave rose map for NDBC buoys and Stations

The wave directional spectra reveal even more detailed characteristics of the wave climate. Specifically, Figure 4.16 shows the buoy 44097 monthly average wave elevation variance density, or energy density as it is commonly referenced, for all direction and frequency bands. This station's selection was made because it is located inside the SNE offshore wind projected area and our main domain of interest.
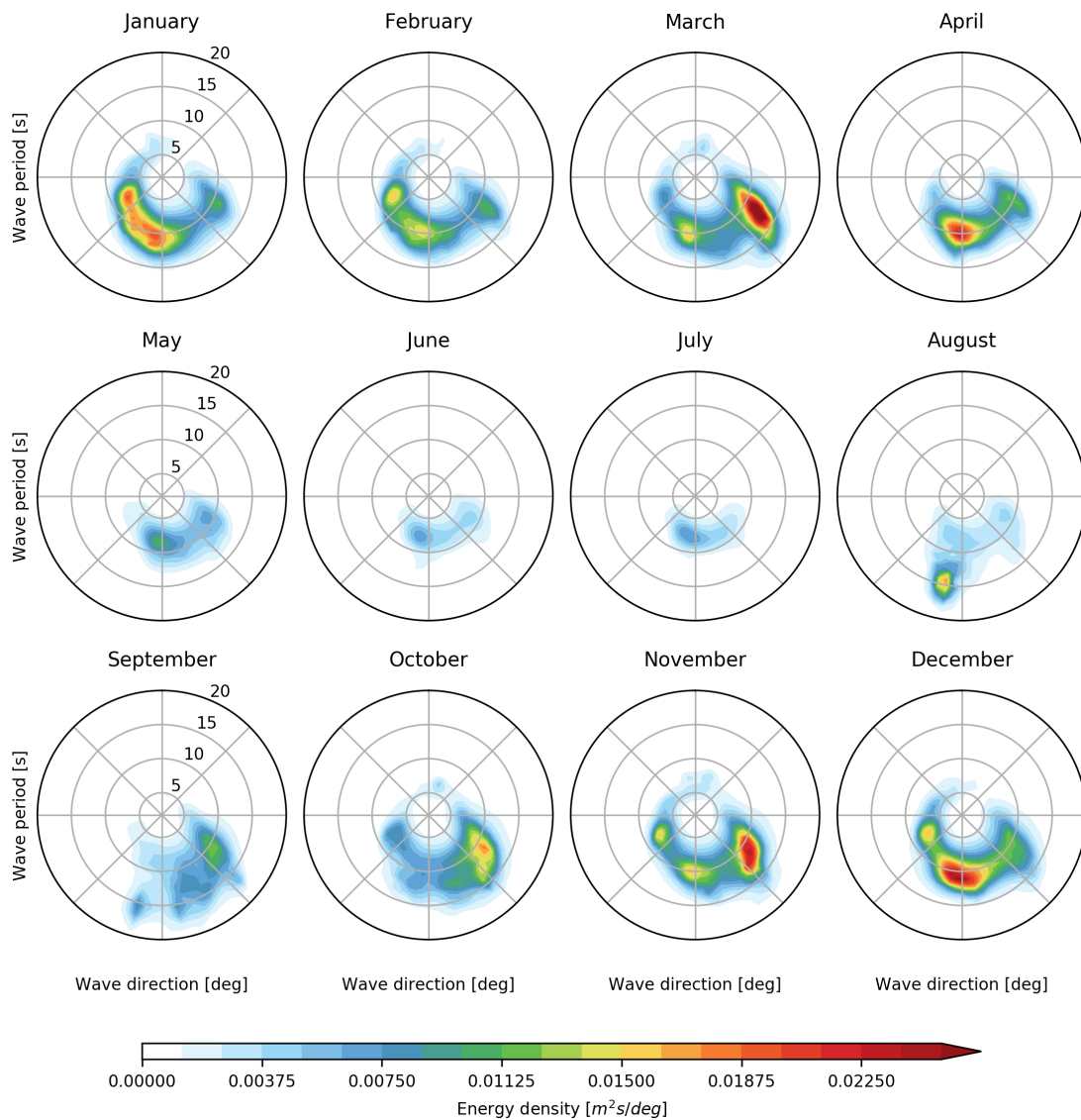
FIGURE 4.16: Buoy 44097 monthly average wave variance (energy) density for the 2009-2019 period.

Three main wave systems can be identified with distinct directions, periods, and development of their variance density throughout the year. The first one is a wind wave system, judging from its direction and range of periods. This wave system propagates its energy from the southwest with average periods of between 6 to 8 seconds, and it is evolving from October to April, with a peak in January. Starting from May and during the summer months, this system shifts its direction to southern with noticeably lower energy. The second system is a mixed swell-wind wave system that propagates from the south. It is evolving from November until April with maximum variance density in December and April. The third one is a swell system with a 10 to 15 seconds period range propagating from the southeast. This system is strongest in March and November, but it shows considerable energy from

September to April. Besides, all three main systems are present from November until March with distinct levels of variance density. Finally, the southern wave direction during summer, evident in Figure 4.15, is caused mainly by the southern swell with the highest energy density during August, with periods close to 15 seconds.

4.2 Wind Speed Probability Density Functions

The process of fitting to the theoretical probability functions and the estimation of the corresponding parameters was described in 2.5. The initial assessment and comparison between the *SciPy* extended library of PDFs is not included in this section. Only the estimated parameters, statistics, and figures of the four best fitted PDFs to each boy's data are included. The evaluation of the fitting is performed with the Kolmogorov-Smirnov (K-S) goodness-of-fit test and the calculation of the K-S error, which represents the deviation of the empirical Cumulative Distribution Function (CDF) to the theoretical. The distribution with the smallest K-S error value is often proposed as the best fit. For further assessment, the probability plots for each buoy and each of the four proposed PDFs are also added, including the coefficient of determination (R^2).

All calculations were performed to WS data from four selected buoys with a distance less than 50 kilometers from the coast. First, a table including the estimated PDF parameters are presented for each buoy's time series and all four distributions. The four distributions included are the ones with the smallest K-S error among the 90 distributions available in the *SciPy* library. Finally, Figure 4.21 contains all empirical PDFs that fit best to the buoys' data and also the u_{10} histograms.

Based on the K-S error values in Table 4.7 and the coefficients of determination on the probability plots, the distributions that best fit the data are the Beta and Johnson S_B for the coastal buoys 44025, 44017, and 44065, which are located between 20 and 40 kilometers off the coast. For the sheltered buoy 44020, the Weibull 3P distribution is accepted as the best to describe the long-term u_{10} distribution.

Buoy	PDF	shape α	shape β	location γ	scale η	K-S error
44025	Johnson S_B	1.45889	1.51276	-1.36785	29.55943	0.00855
	Beta	2.70274	7.88593	-0.23496	29.49847	0.00861
	Weibull 3P	2.02042	-	0.01575	8.21624	0.01256
	Rayleigh	2	-	0.04085	5.78170	0.01034
44017	Johnson S_B	1.26469	1.39953	-1.02751	27.13660	0.00870
	Beta	2.50125	6.73867	-0.08808	27.31905	0.00892
	Weibull 3P	2.00142	-	0.05729	8.18246	0.01318
	Rayleigh	2	-	0.05897	5.78394	0.01301
44065	Johnson S_B	1.45918	1.52591	-1.34807	28.62410	0.01001
	Beta	2.70918	7.70465	-0.21269	28.02316	0.00808
	Weibull 3P	2.03604	-	0.02152	7.96683	0.01285
	Rayleigh	2	-	0.06330	5.58648	0.01106
44020	Johnson S_B	1.69612	1.78309	-2.17746	32.48900	0.01429
	Beta	3.44047	10.4444	-0.64746	32.00931	0.01364
	Weibull 3P	2.16096	-	-0.04203	8.27184	0.01086
	Rayleigh	2	-	0.12833	5.65487	0.03053

TABLE 4.7: u_{10} Probability Density Function parameter and K-S error statistics.
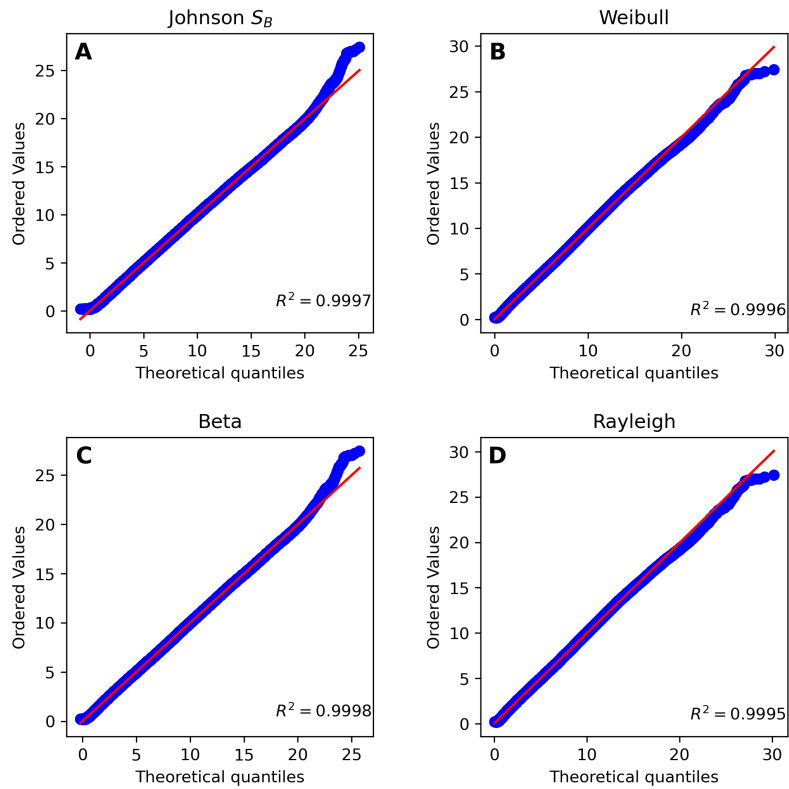
FIGURE 4.17: Buoy 44025 u_{10} probability plots and the corresponding coefficient of determination for each PDF.
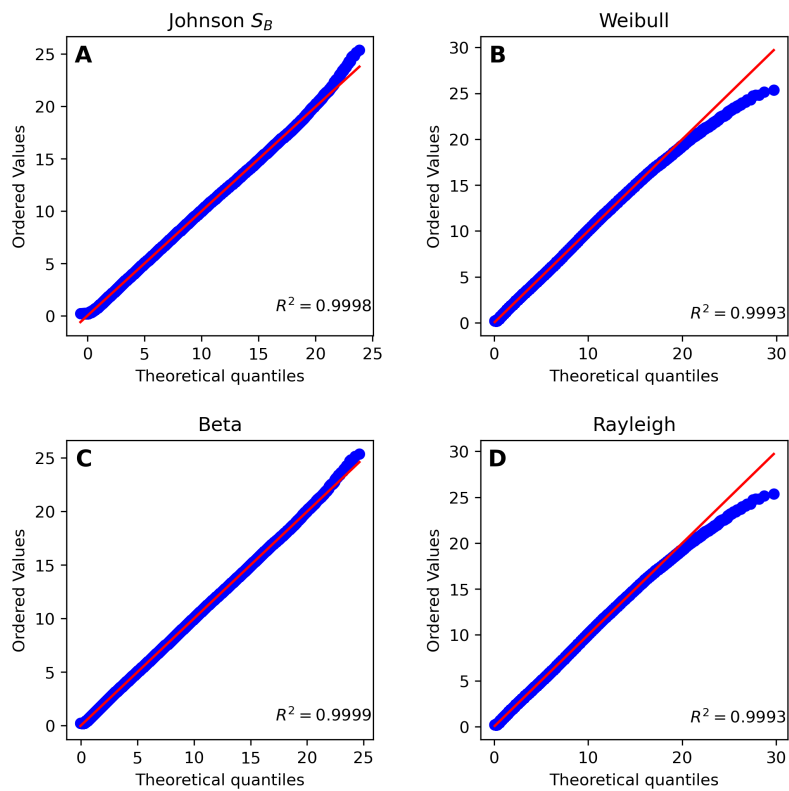
FIGURE 4.18: Buoy 44017 u_{10} probability plots and the corresponding coefficient of determination for each PDF.
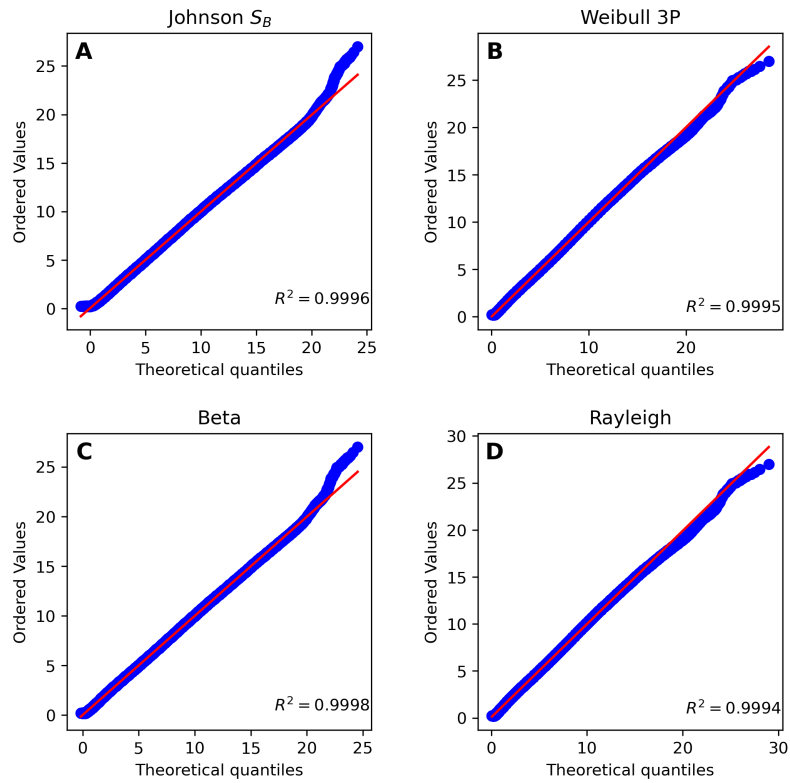
FIGURE 4.19: Buoy 44065 u_{10} probability plots and the corresponding coefficient of determination for each PDF.
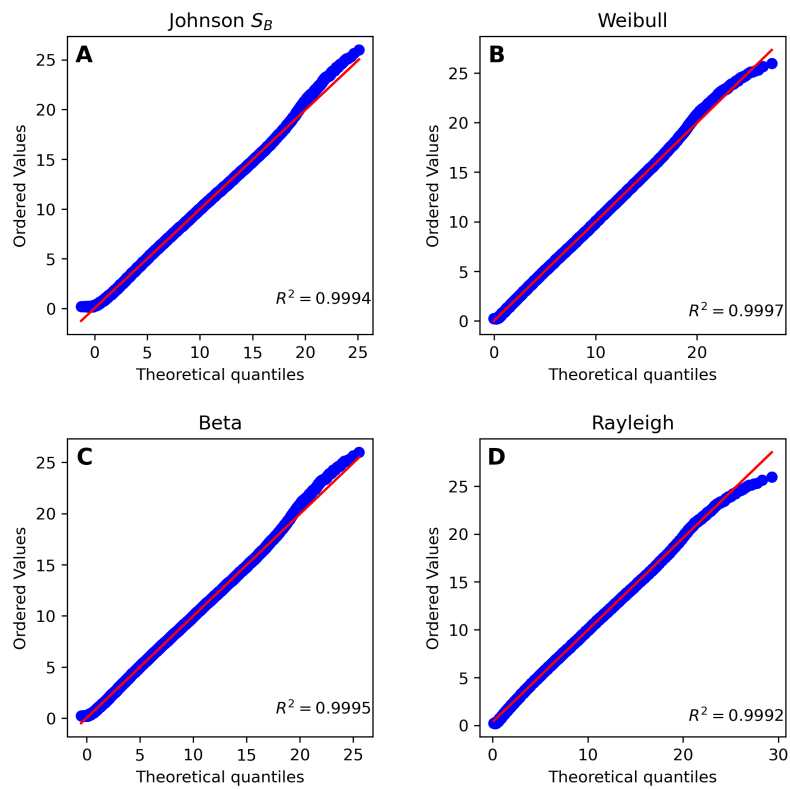
FIGURE 4.20: Buoy 44020 u_{10} probability plots and the corresponding coefficient of determination for each PDF.
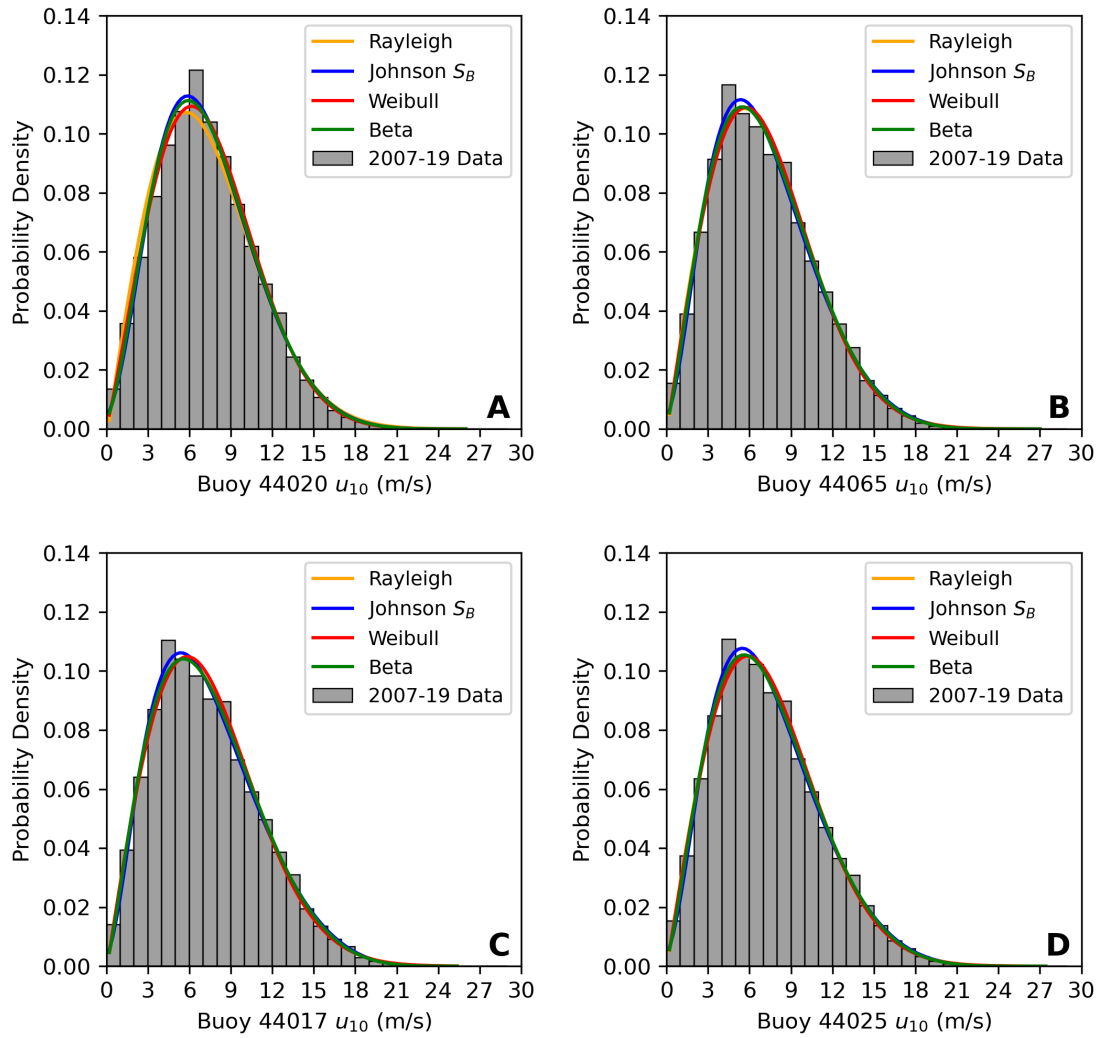
FIGURE 4.21: u_{10} histograms and the four PDFs that provide the best fit to the buoy data.

4.3   Wind Speed and Wave Height Relationships

The theoretical formulas which connect u_{10} with H_s are available in 2.4. In this study, the wind-wave relationships are estimated using a second-degree polynomial regression fitting of the SWH to the u_{10} adjusted values. Previous studies, dedicated to the East Coast of the United States, use more sophisticated methods [4]. This study attempts to integrate and interpret the difference between the wind-wave relationships depending on the wind direction for every location. Specifically, the eight major directions, each with an angular window of 45 degrees, are used. All figures include the sample size and the estimated coefficients of the fitted line.
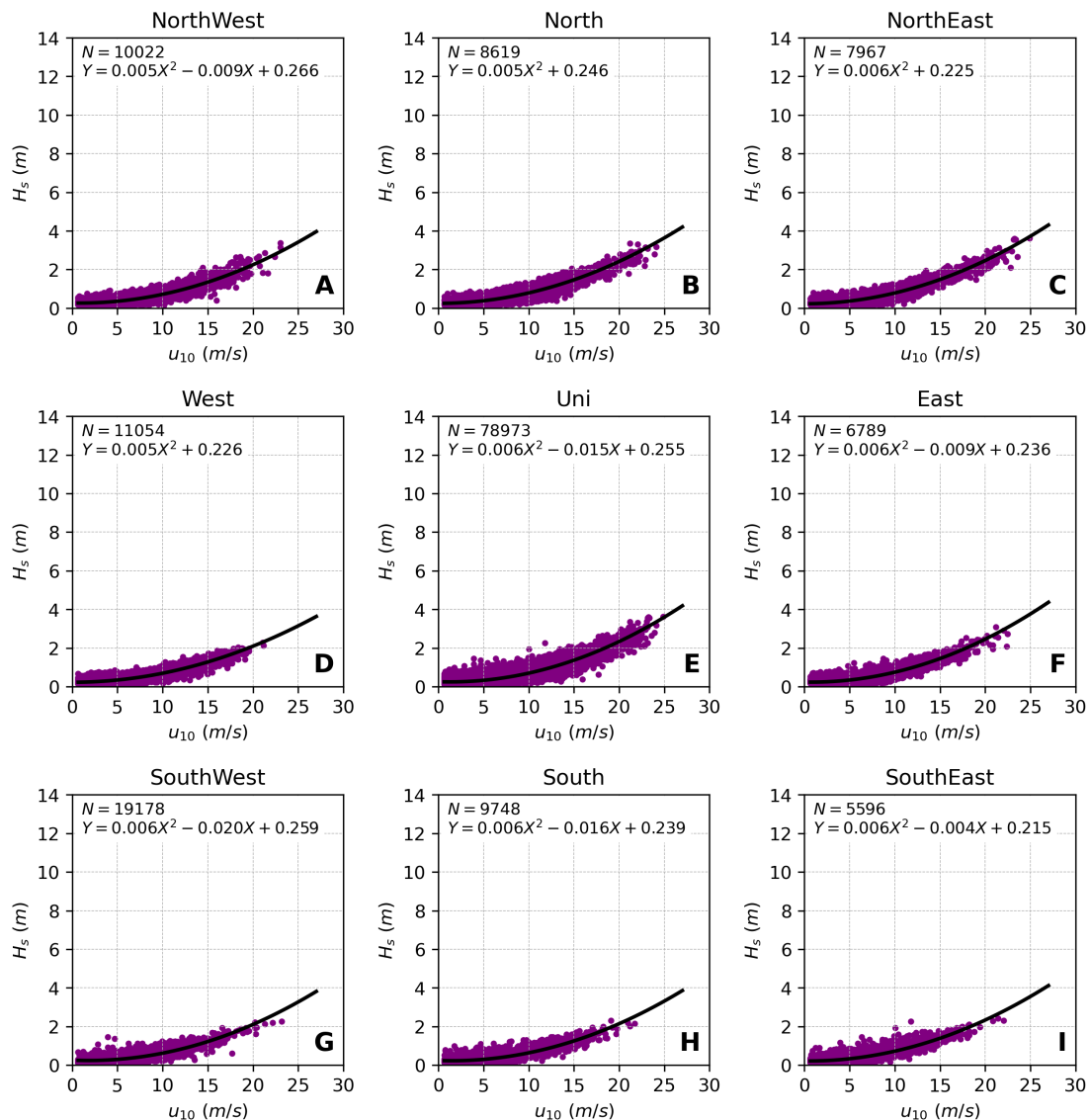
FIGURE 4.22: Buoy 44020 wind wave relationships for each of the main wind directions and for all directions combined (E).

Figure 4.22 indicates the strength of the relationship. The sheltered buoy 44020 is surrounded by the southeastern Massachusetts and the Martha's Vineyard, Nantucket islands. The only opening for the entrance of swell waves in the region is from the east. Hence, wind waves dominate the region throughout the year. The relationships fit exceptionally the data with a minimal number of outliers. Even the highest waves that are coming from

the northeast and north directions are well-captured by such relationships. Generally, the coefficients are consistent for every wind direction, except for the west, north, and northeast directions, where the second coefficient is zero. The small intercept is an indication of the minimal influence of swells in the region.
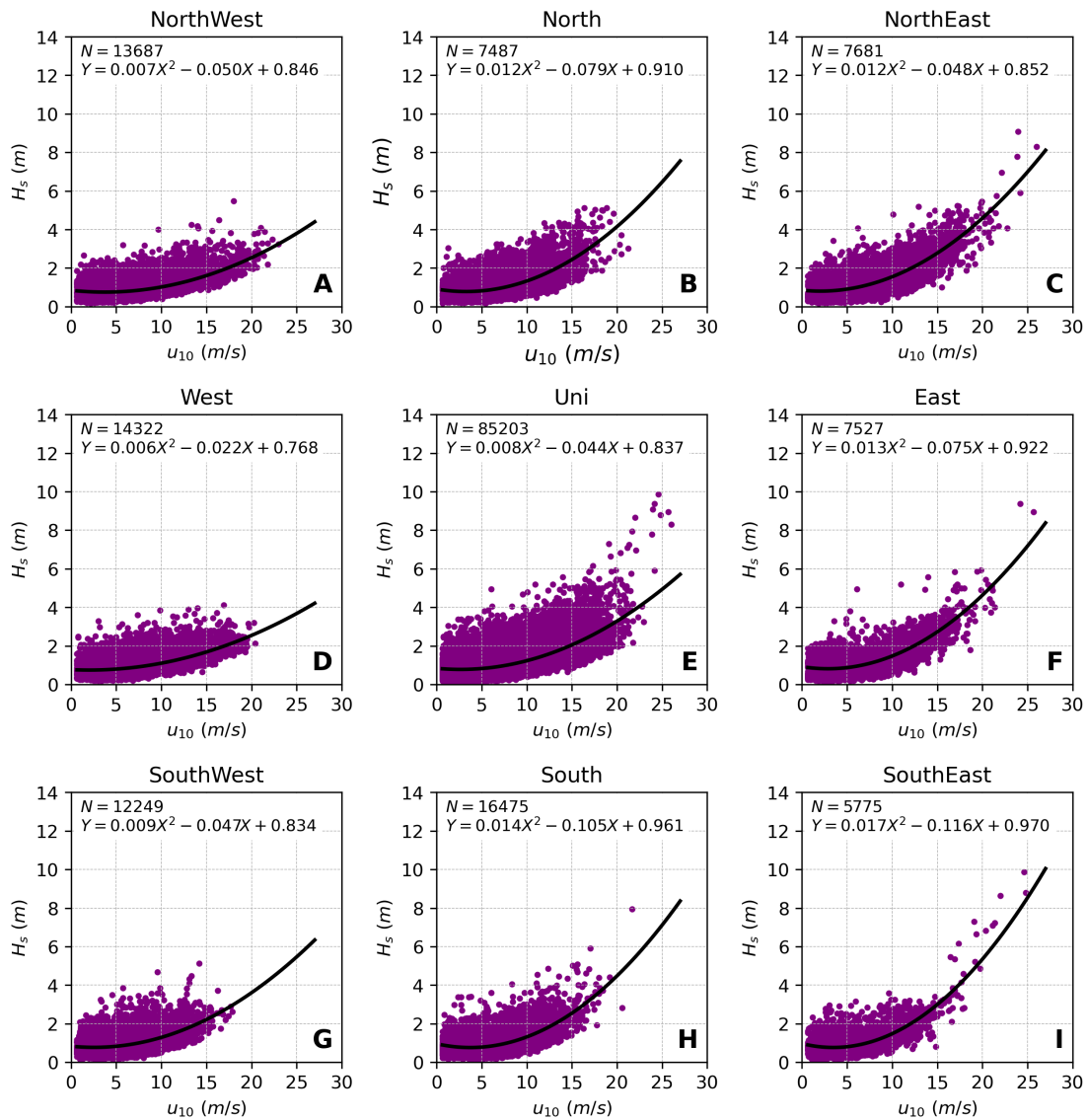
FIGURE 4.23: Buoy 44065 wind wave relationships for each of the main wind directions and for all directions combined (E).

On the contrary, this is not the case for the open-ocean buoy 44008, as it is located in a swell-dominated region, although its distance from the sheltered buoy is just 50 kilometers approximately. The range of the H_s values is substantial, even for low wind speeds, increasing the uncertainty of its estimation when only the u_{10} is given. The coefficients also vary depending on the wind direction. In directions with higher wind speeds and potential for producing higher sea states, the coefficients tend to be larger, as the northeast and east directions. Besides, an interesting feature of the coastal buoy relationships is that when the wind is aligned with the swell direction (from the east to the south), the second coefficient is significantly larger, almost ten times the same coefficients of the relationships for the western wind direction, which is the most common for every location in SNE throughout the year. The above means that on conditions of very light winds speeds (0-5 m/s), the H_s becomes

smaller with increasing wind speed. This feature is not present in the sheltered buoy relationship. We may connect this behavior with the upward momentum transfer described in [42], but it requires further investigation.
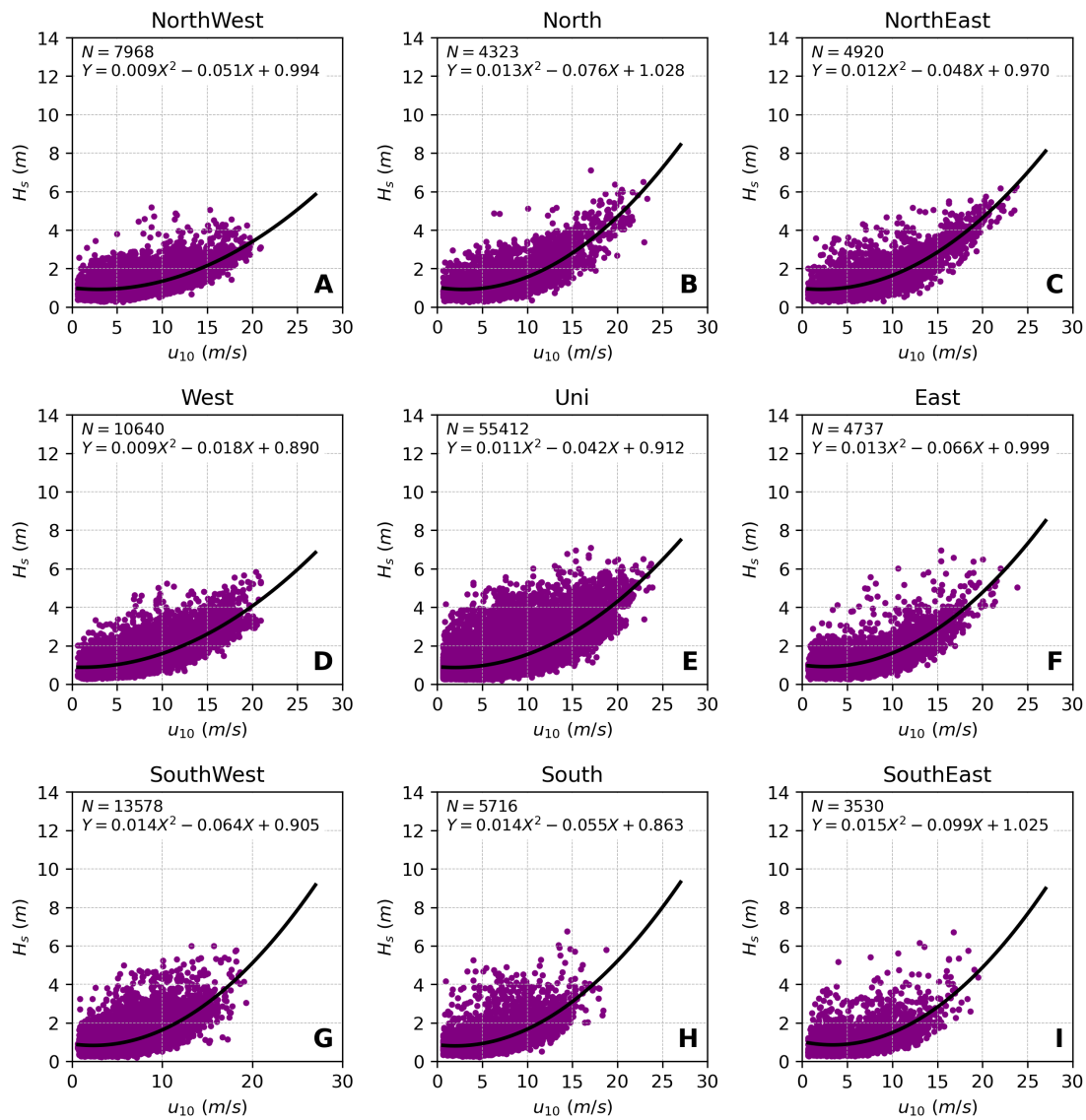
FIGURE 4.24: Buoy 44017 wind wave relationships for each of the main wind directions and for all directions combined (E).

Finally, Figure 4.27 shows a comparison of the estimated relationships for the whole time series record of each buoy. The increasing curvature of the lines of best fit with increasing distance from the coast is expected. It is also worth mentioning that the adjacent coastal buoys 44025 and 44017 located south of the Long Island Sound show almost identical relationships. Again, it is necessary to highlight the increased uncertainty of the relationships and their reduced capability to describe them in highly swell-influenced regions accurately. The latter leads us to investigate the wind-wave interactions with respect to waves' growth stage in the next section.
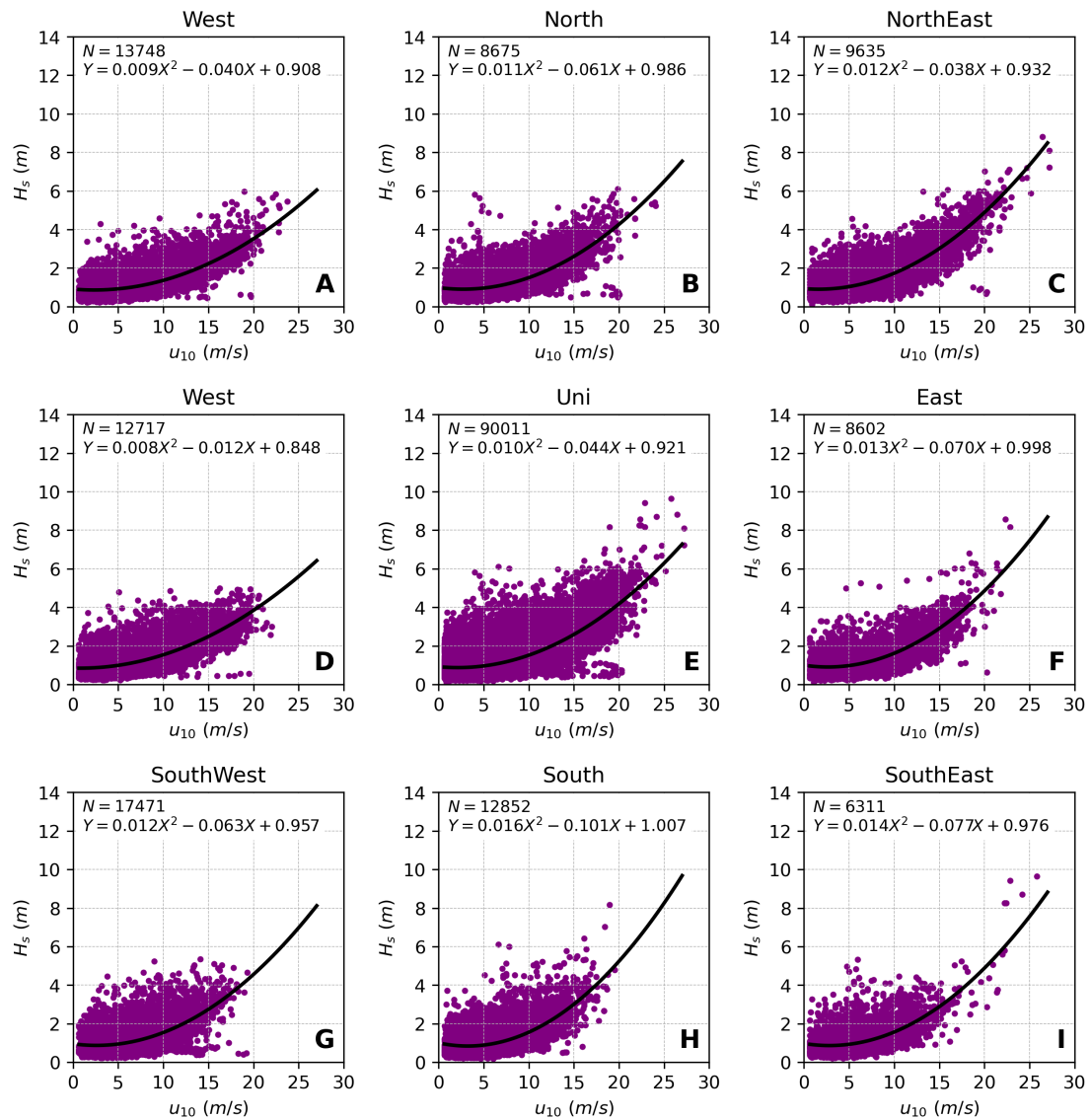
FIGURE 4.25: Buoy 44025 wind wave relationships for each of the main wind directions and for all directions combined (E).
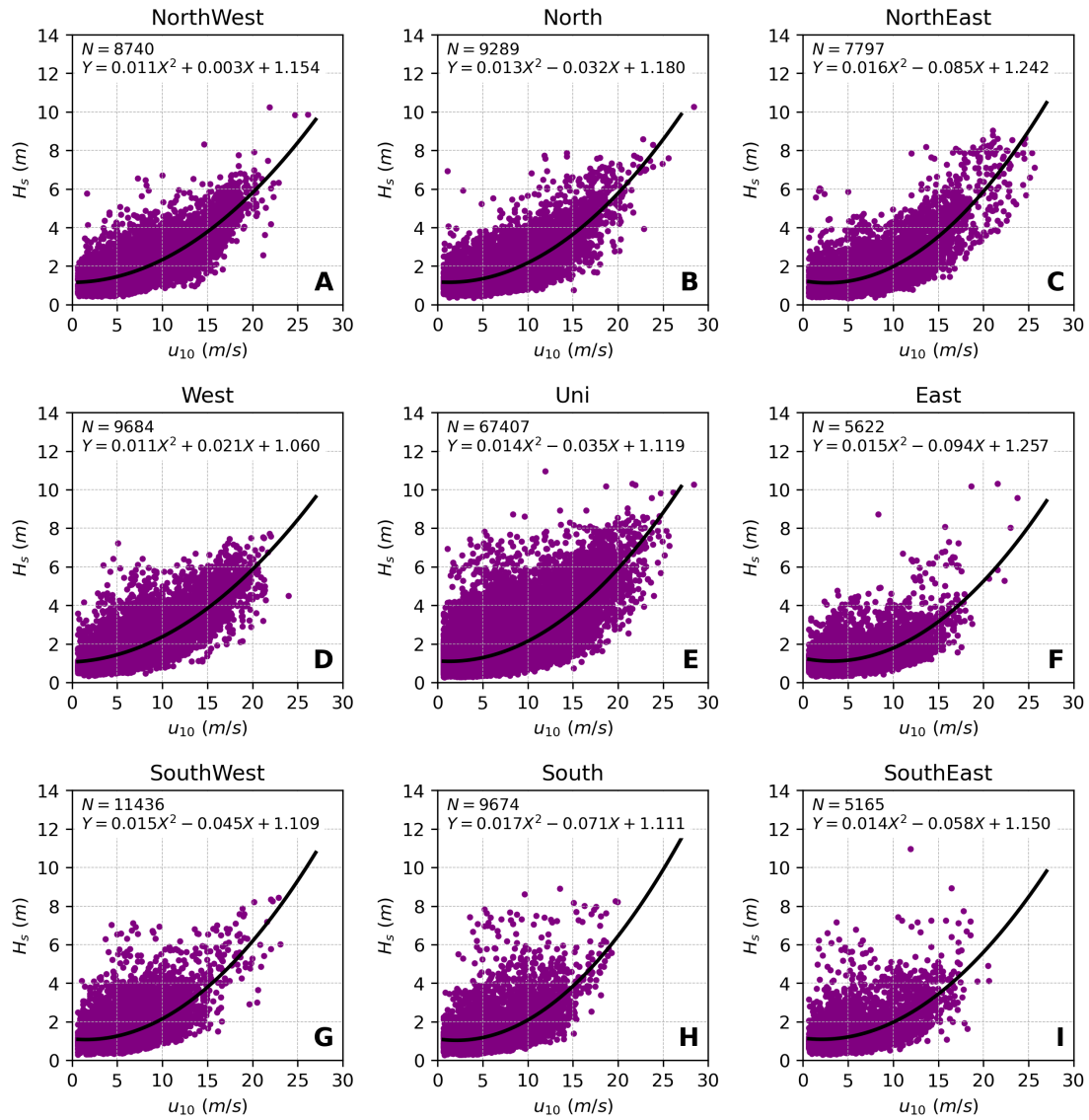
FIGURE 4.26: Buoy 44008 wind wave relationships for each of the main wind directions and for all directions combined (E).
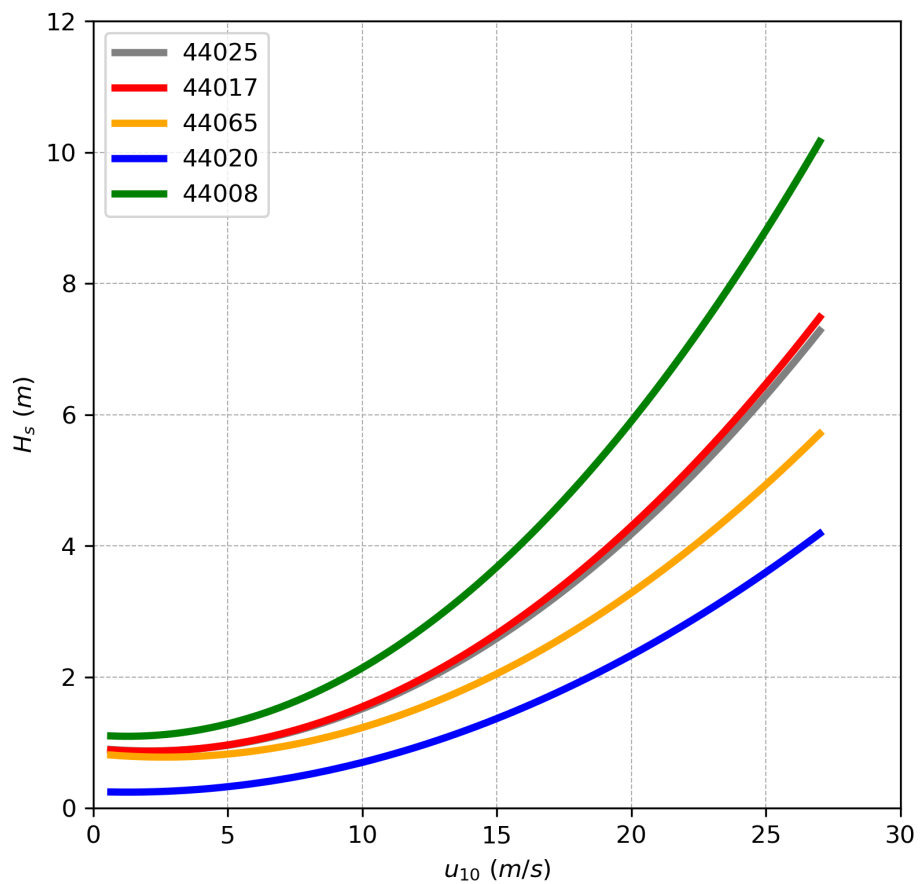
FIGURE 4.27: A comparison of the wind-wave relationships for the NDBC Buoys.

4.4 Classification of ocean waves based on their inverse wave age

The theoretical basis of the inverse wave age criterion is explained in 2.2. The results presented in this section are based on the inverse wave age histograms for each buoy. Three figures are included: one for the whole datasets and two representing the inverse wave age distribution during the winter and summer seasons respectively. The estimated probabilities of occurrence for wind waves, mixed sea state, and swells are reported in Table 4.8.

Buoy	Summer			Winter			All		
	Wind	Swell	Mixed	Wind	Swell	Mixed	Wind	Swell	Mixed
44020	0.647	0.215	0.139	0.774	0.130	0.096	0.717	0.162	0.121
44065	0.129	0.483	0.387	0.382	0.444	0.173	0.247	0.474	0.279
44017	0.142	0.464	0.394	0.323	0.416	0.261	0.226	0.455	0.319
44025	0.149	0.457	0.393	0.446	0.354	0.201	0.284	0.413	0.302
44008	0.044	0.485	0.470	0.225	0.363	0.412	0.132	0.429	0.439
44066	0.163	0.424	0.413	0.433	0.290	0.276	0.280	0.368	0.352

TABLE 4.8: Frequency of occurence of wind-sea, swell and mixed sea state for NDBC buoys using the inverse wave age classification for winter, summer and all seasons.

Generally, the inverse wave age distributions are bimodal. The first peak represents the mixed sea states and swells, and the second peak, the wind waves. The figures include a vertical dashed line that represents the wind-wave equilibrium. Sea states with an inverse wave over 0.83 are characterized as purely wind waves, although this is not a hard limit. Besides, an empirical limit for swell dominated sea states is an inverse wave age equal to 0.15. Waves with an inverse wave age between the two limits are categorized as mixed, and they are influenced both by wind-waves and swell. It is worth mentioning that the inverse wave age represents deep water waves at the peak, not the whole wave spectrum.

A general trend is that the second peak, which represents the wind waves, does not appear during the summer, except for the sheltered buoy 44020. The latter indicates again that swell's influence in this location is not significant with respect to the coastal and open ocean buoys. The bimodal distribution retains its characteristics during the summer with higher wind waves and lower probability of mixed/swell waves. During winter, almost 80% of the waves are purely influenced by the wind in this location. This result is connected with the low WS seasonal variability in Figure 4.5B. The above does not apply to the coastal buoys and the open ocean buoy 44066. Figures 4.30B,C,D,F show clear peaks after the wind-wave equilibrium during the winter, when the influence of the wind is most substantial due to the high values of u_{10}. However, the second peak ceases to appear during the summer distributions in Figure 4.29, and at the same time, the mixed/swell probability density peaks almost double their value. The western part of the region is significantly influenced by the wind, especially during winter, when the wind-waves' probability is nearly as high as the probability of swell/mixed seas. For buoy 44025, purely wind waves are developing three times less during the summer than the winter, when the probability density peak is higher than the swell/mixed.

For the open ocean buoy 44008, the inverse wave age distribution appears to have a single peak throughout the year. During the winter, this peak has a lower probability density, and the distribution is more spread to a broader range of inverse wave age values. In contrast, over 95% of the waves are characterized as mixed or swell based on the inverse wave age classification during summer. Consequently, the wind waves' influence during the summer

is minimal for the eastern part of SNE and at a distance over 100 kilometers from the closest coast.
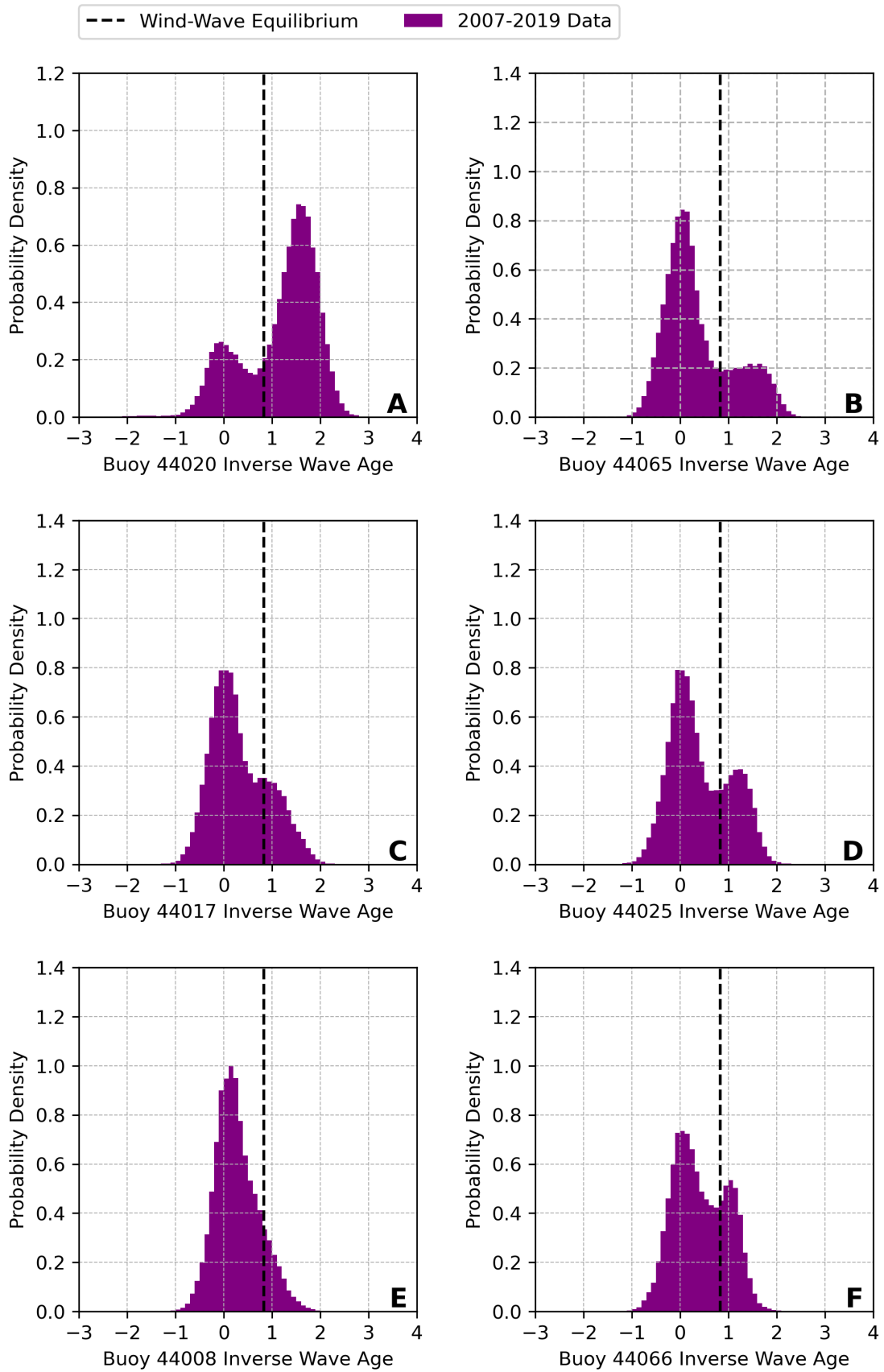
FIGURE 4.28: NDBC buoys Inverse Wave Age distribution.
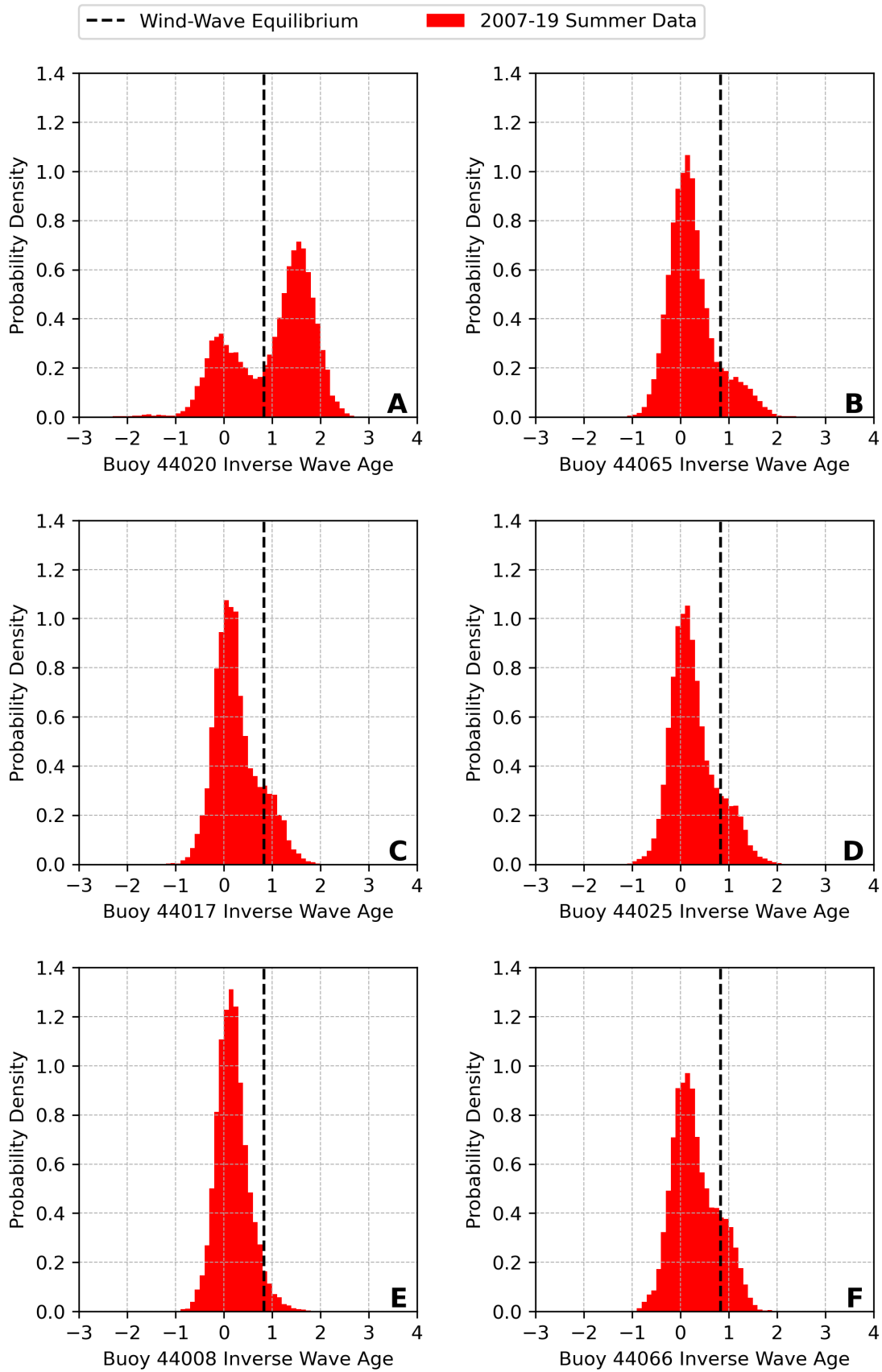
FIGURE 4.29: NDBC buoys summer Inverse Wave Age distribution.
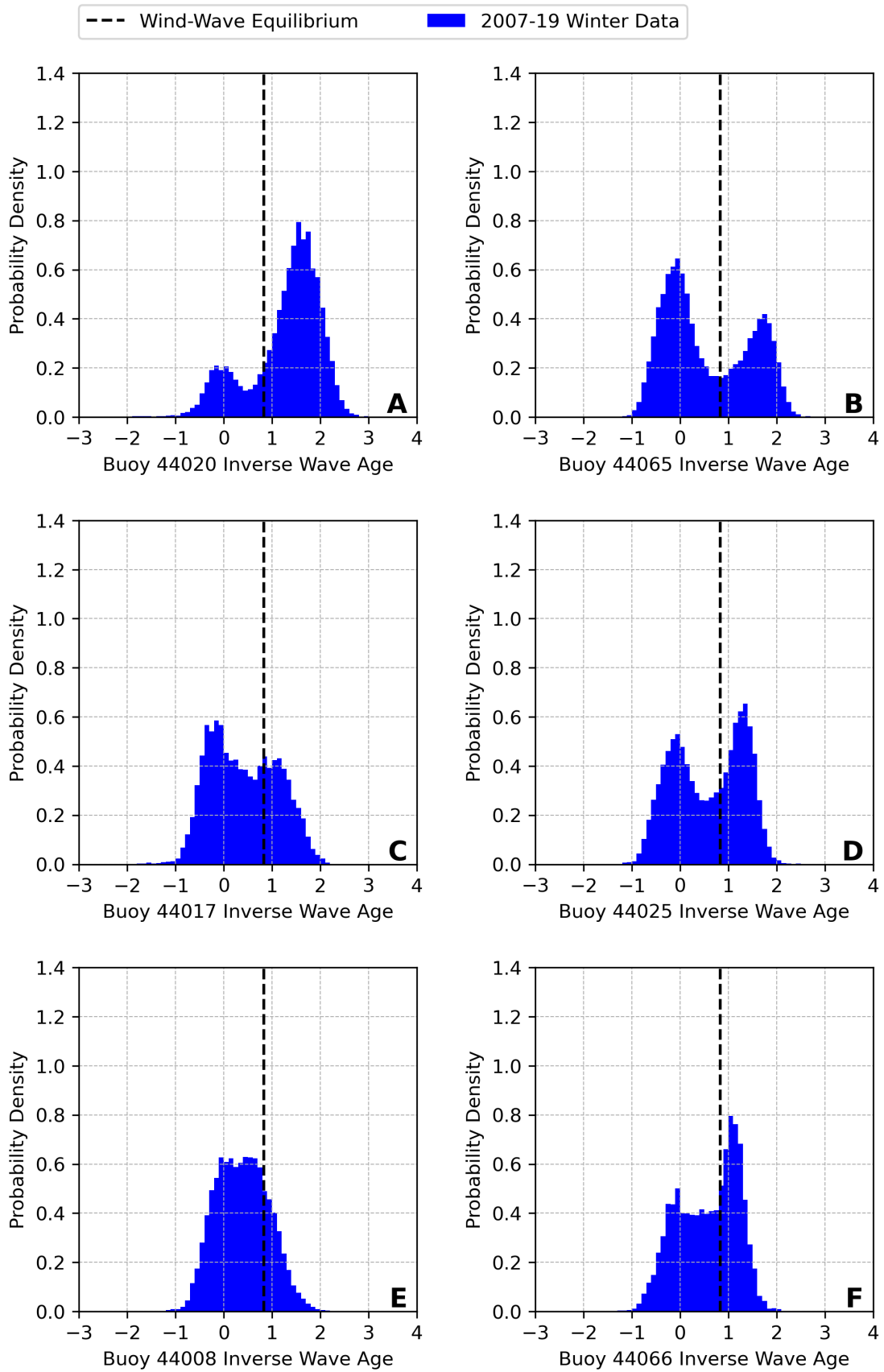
FIGURE 4.30: NDBC buoys winter Inverse Wave Age distribution.

4.5 A case study of extreme events

In the previous sections, the focus was on the normal wind-wave conditions. On the other hand, extreme winds and waves are often described by values at the upper tail of the u_{10} and H_s probability density functions. The study of extreme events is essential and precedes the offshore wind farms' design and construction to assess the wind turbine fatigue loads. This section aims to describe the wind and wave mechanisms underlying the development of the most frequent extreme events in SNE, the extratropical storms, or Nor'easters, defined in 1.2.
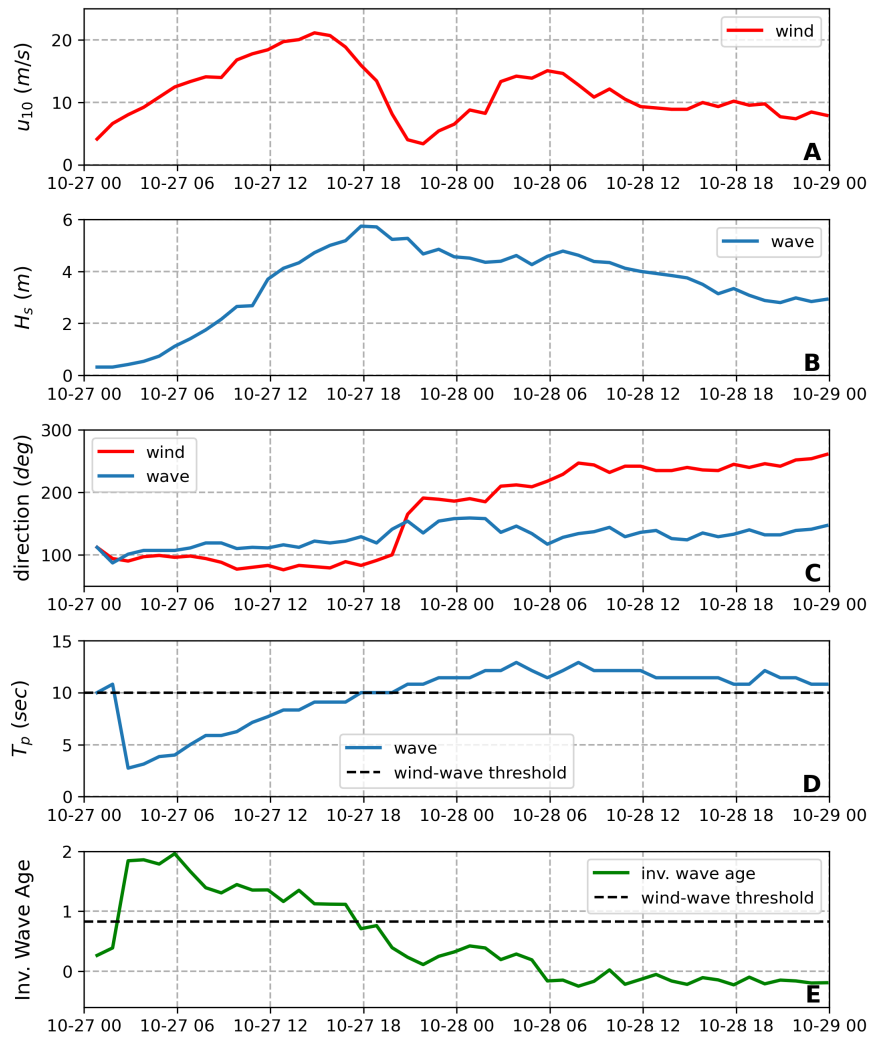
FIGURE 4.31: Time series of the main wind and wave parameters measured by buoy 44017 during October 27 and 28, 2018 describing the passing of the Nor'easter.

The time series of the wind and wave parameters measured by buoy 44017 in Figure 4.31 shows the development of the Nor'easter storm that passed from SNE on October 27, 2018, bringing extreme waves and coastal flooding. In the early morning hours of October 27, light winds and calm sea states are present before the storm's passing. Wind and waves are coming from the same, east-southeast direction. As the wind increases its intensity, the waves' H_s and T_p also progressively increase. The WS reaches its maximum at around 3:00 PM, while the sea state becomes roughest with a three-hour lag at 6:00 PM.
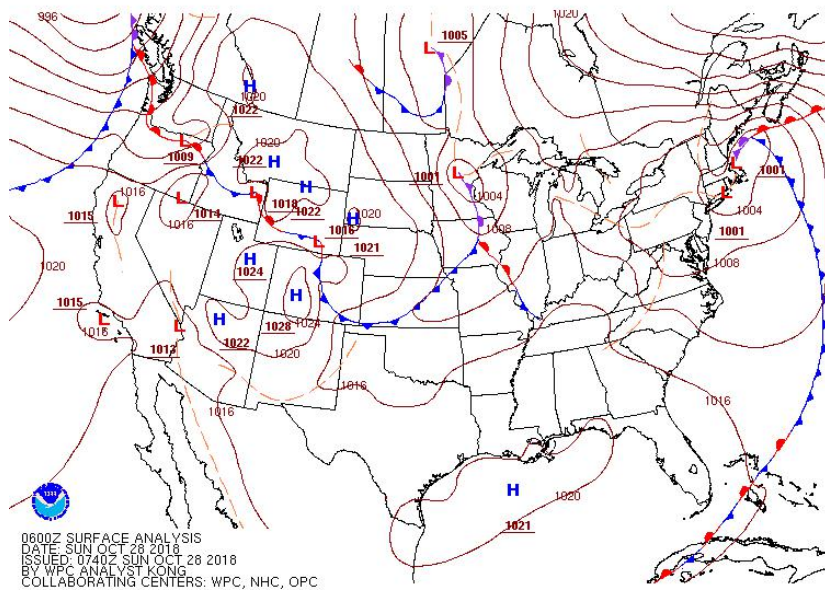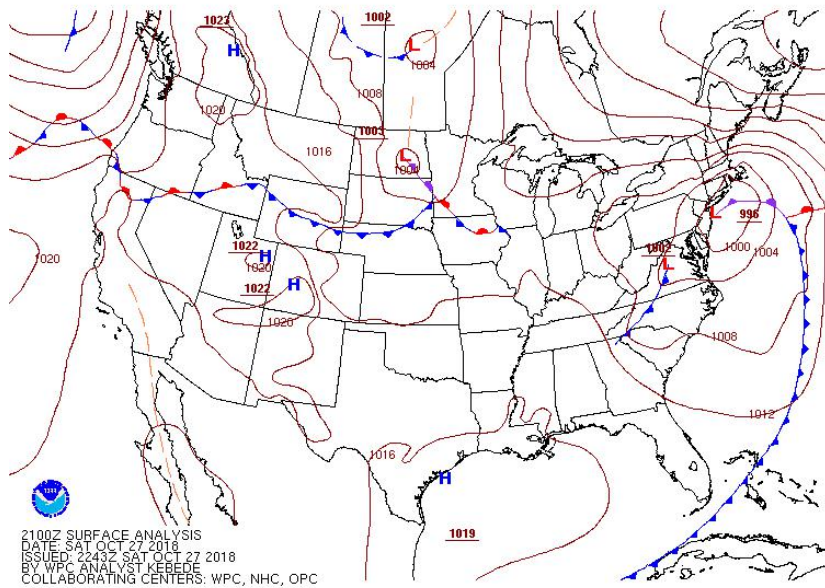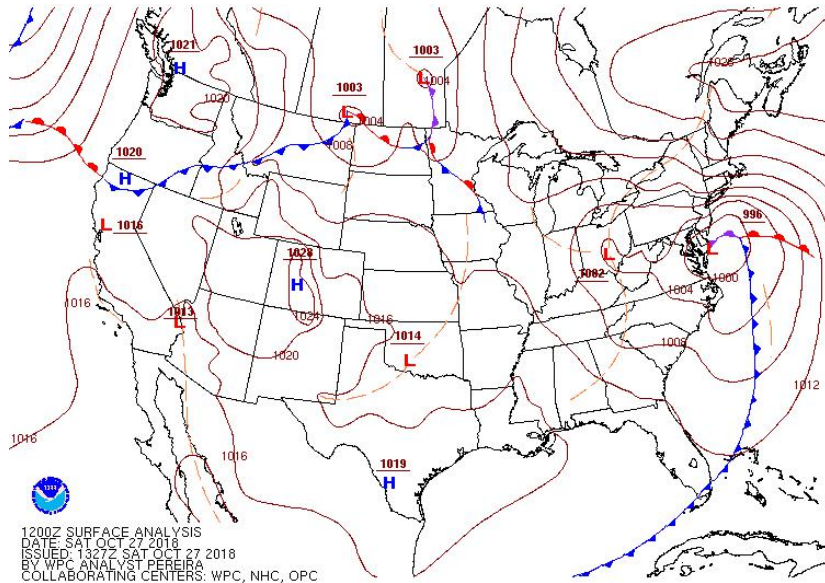
FIGURE 4.32: Surface analysis maps before (upper panel), during (center panel) and after (bottom panel) the passing of the October 27, 2018 Nor'easter from SNE. Derived from: WPC's Surface Analysis Archive
.
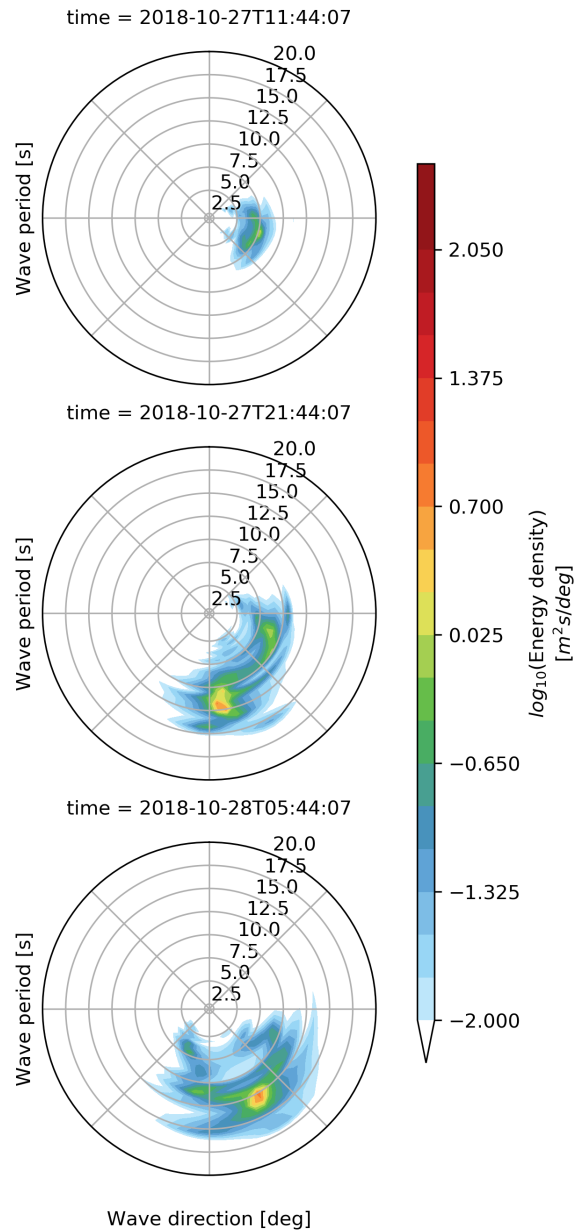
FIGURE 4.33: Buoy 44097 directional wave spectra before (upper figure), during (center figure) and after (bottom figure) the passing of the October 27, 20018 Nor'easter over SNE. Values represent the energy density logarithm for better visualization.

At 6:00 PM, the wind also starts to shift its direction to the south while the wind intensity decreases to a minimum at 9:00 PM. The combination of the WS decrease and the shift of the wind's direction is critical for developing a local south-southwestern swell system. From this point on, wind and waves are coming from different directions. Considering the dominant period, it passes the crude 10-seconds wind-wave threshold simultaneously to the WS's minimum. If we also look at the inverse wave age time series, the sea state becomes mixed at the same time when the SWH peak occurs and becomes swell-dominated between 5:00 to 6:00 AM of October 28. The wind, which started to increase again on October 27 at 9:00 PM, reaches a second but lower maximum and remains almost constant from the early hours of October 28 and throughout the day. The waves remain substantially high (over 4 meters) until noon on October 28, but they are gradually losing their energy.
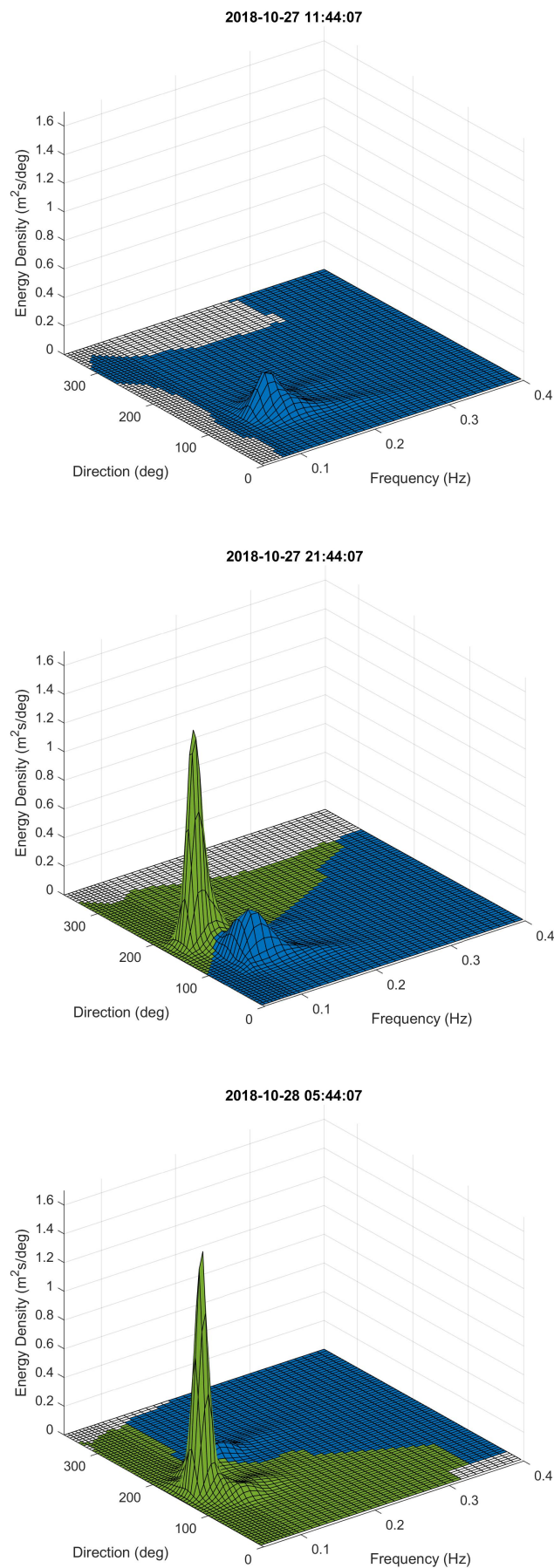
FIGURE 4.34: Spectral partitioning of the buoy 44097 directional wave spectra before (upper figure), during (center figure) and after (bottom figure) the passing of the October 27, 2018 Nor'easter over SNE.

Figure 4.32 includes the surface analysis maps from the Weather Prediction Center's (WPC) archive before, during, and after the passing of the Nor'easter from SNE. For a more detailed analysis, we provide the buoy 44097 directional spectra. Figure 4.33 includes three snapshots of the storm development based on buoy observations, almost coinciding with the surface analysis maps. The upper figure at 11:44 AM shows a single wind-wave system with relatively small but increasing elevation variance density and a dominant period of 7-8 seconds. After the wind direction shift at 9:44 PM, we can distinguish the split in two separate systems, the wind-wave, and the south-southeast swell, with an 11 to 12 seconds period. After nine hours, only the swell system is still present. Figure 4.34 is an even more realistic representation of the sea state and the result of spectral partitioning of the aforementioned directional spectra described in 2.2. The blue color represents wind-waves, green is for the first swell system, and the noise, the spectral domain where zero energy is observed, is the white part of the directional wave spectra. In the upper figure, the wind-wave system with low elevation variance density is only observed. At 9:44 PM, the swell system has already been generated by the shift in the wind direction, and we can identify the two separated peaks. This snapshot is an example of a mixed sea state when the highest peak represents the swell and the lowest the wind-wave. The latter gradually loses its energy, and in the early morning hours of October 28 (lower figure), the swell system is dominant but with decreased elevation variance density.

4.6 Validation of Altimeter WS and SWH observations in the SNE region

A description of the inherent challenges of validating satellite altimeter observations with ground truth stations is available in Section 3.2. Sensors onboard buoys and altimeters are sensitive to errors. However, even if we considered their measurements perfect, deviations would still exist on the match-up observations due to the spatial and temporal sampling and representation differences based on each measurement system's principles. The results presented in this section aim to quantify how well altimeters match buoy observations on a regional level.
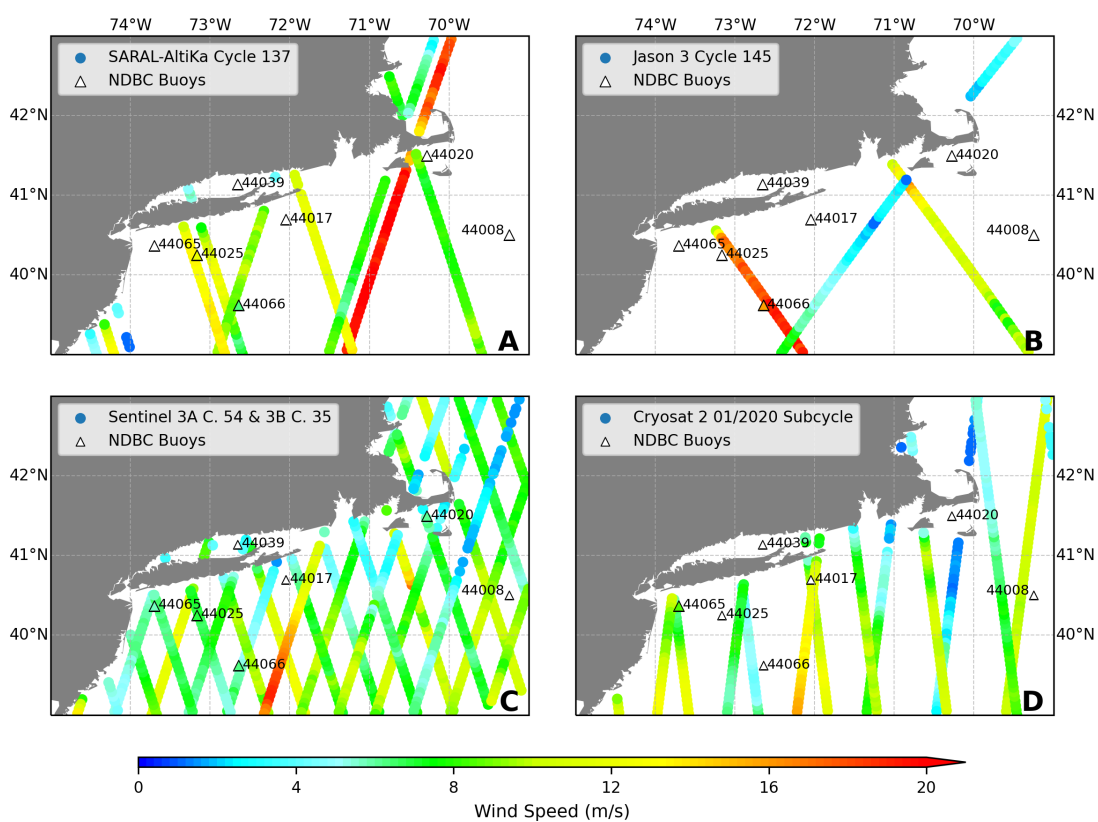
FIGURE 4.35: Altimeter tracks during January 2020 over SNE, including the buoys' locations and the collocated WS observations.

Figure 4.35 shows the altimeters tracks and WS observations over SNE during a specific cycle or subcycle in January 2020. Sentinel 3 A and B tracks are included in the same Figure 4.35C, and their combined dataset was used in the calculations because they are considered as the same mission with identical sensors. In the same Figure, the buoys' locations are depicted with triangles. The collocated observations are represented by colored triangles, whereas the buoys that do not match with the altimeters during their specific cycle or subcycle are left empty. This process described in 3.2 was performed iteratively for multiple years, depending on the altimeters' data availability. The final collocated dataset contains both buoy and altimeter observations that were matched in space and time. Its sample size is expected to be relatively small, considering the range of the altimeter cycles (10 to 35 days) and the small sampling radius required in a coastal region.
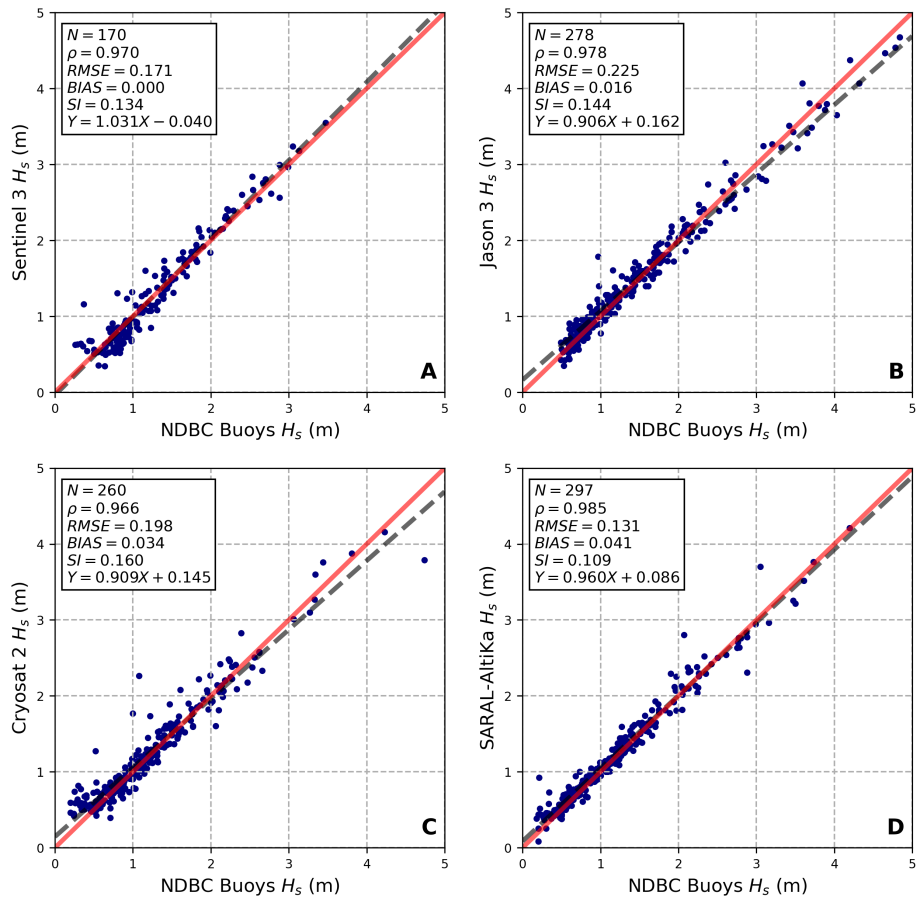
FIGURE 4.36: Comparison of SWH between altimeter and in-situ observations.
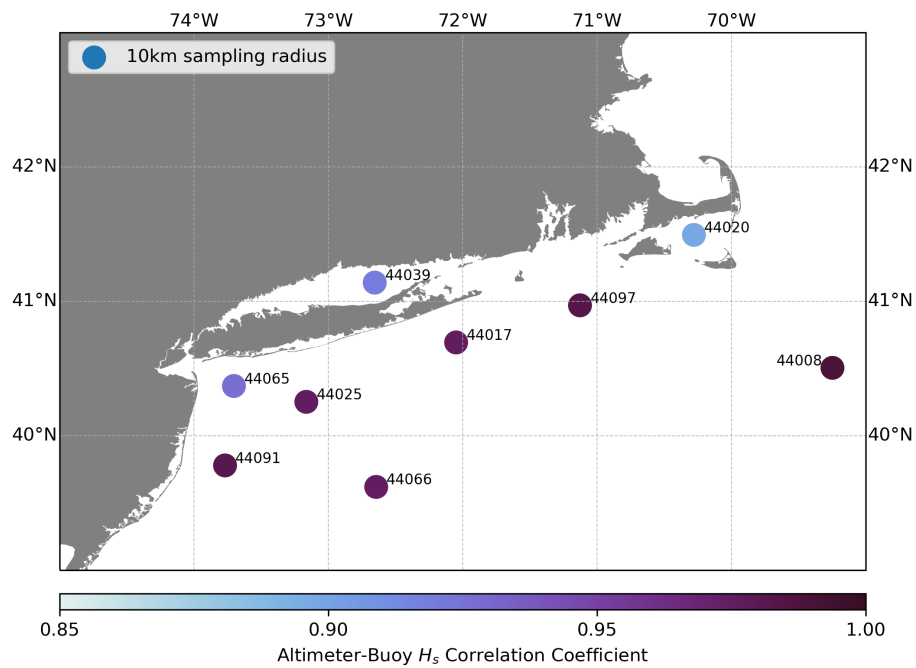
FIGURE 4.37: Correlation coefficient map between altimeter and buoy SWH collocated data.
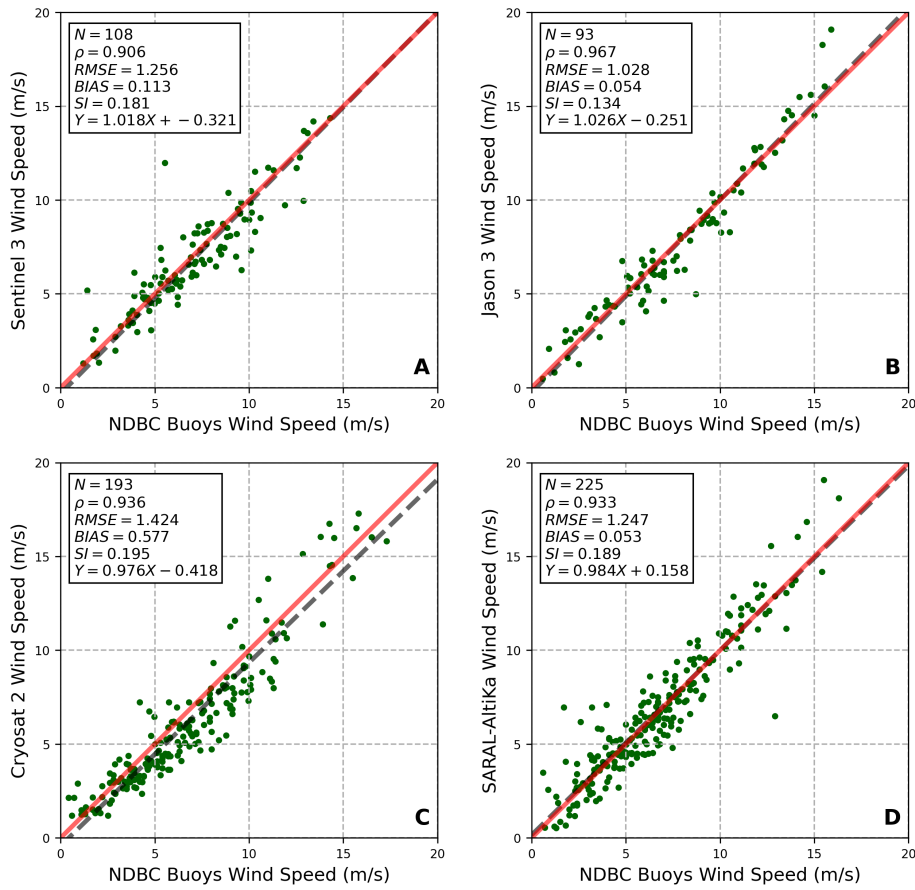
FIGURE 4.38: Comparison of WS between altimeter and in-situ observations.
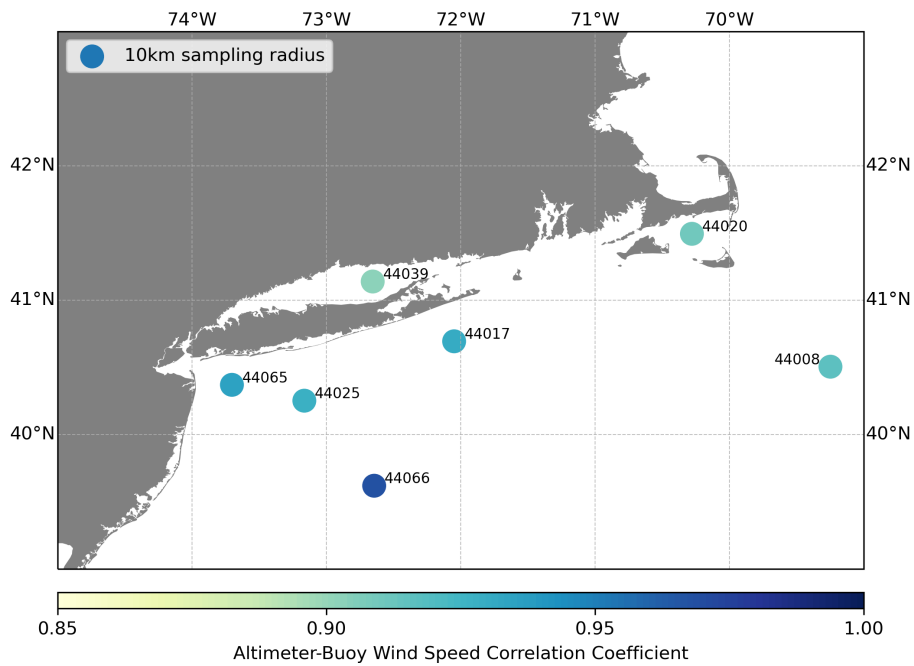
FIGURE 4.39: Correlation coefficient map between altimeter and buoy WS collocated data.

The collocated dataset's WS and SWH comparison and also the evaluation statistics

are shown in Figures 4.36, 4.38. It is evident that due to the different number of buoys with available WS and SWH, the corresponding comparisons result from larger sample sizes for the SWH. The evaluation metrics and the slope of the regression line show that SARAL-AltiKa has the best overall agreement with the buoys. Although there are a few outliers, they do not significantly influence the close approximation to the buoys' ground truth values. The uncertainty is very low even for SWH values lower than 1 meter, which has been documented as a challenge due to the difficulty in estimating the leading edge slope in low sea states and a general limitation of the satellite altimetry [6]. A root mean squared error (RMSE) of 13 centimeters, a scatter index (SI) of almost 11%, and a correlation coefficient of 0.985 emphasize these results. Sentinel 3 also matches the buoy measurements with a zero average bias, which could also be attributed to the small sample size. Despite the small bias and the high correlation, Jason 3 shows the largest RMSE. This result can be attributed to the considerable number of match-up observations representing SWH over 3 and up to 5 meters. Cryosat 2, which utilizes the oldest technology of the current altimeters, also shows a good agreement with the buoys regarding their correlation and the small bias. Still, it has the highest number of outliers reflected on the SI (16%) and RMSE (19.8 cm). Figure 4.37 confirms the assumption that the agreement between the buoy and altimeter observations is worse at locations with proximity to the land due to the challenges of coastal altimetry described in 2.6. Generally, the agreement is exceptional in terms of correlation statistics, as the SWH correlation coefficient is well over 0.9 in almost every location. The highest correlation coefficient was calculated for the open ocean buoy 44008 and the lowest for the sheltered buoy 44020, located in the Nantucket Sound.

The WS comparison is more challenging, primarily due to the smaller sample size of the collocated dataset. Except for the lower number of stations with available wind data (7), the WS times series also contain more gaps than the SWH. The agreement in terms of statistics is best for Jason 3, but all collocated observations are located in a specific region surrounding the open ocean buoy 44066. On the other hand, SARAL-AltiKa has the largest sample size and collocated measurements at almost every buoy location. The statistics show good agreement with the buoy data with a minimal overall bias (0.053m/s). The comparison of Sentinel 3 with the buoys is sensitive to outliers due to the small collocated sample size, and it has the lowest correlation coefficient among all altimeters. Still, the RMSE (1.256m/s) and the bias (0.113m/s) are small and comparable to the values in the performance reports disseminated after every completed cycle. The worst performance belongs to Cryosat 2 with substantial bias (higher than 0.5m/s). However, the statistics are comparable with the target accuracy of 0.5m/s bias and 2m/s RMSE of the WS estimation from scatterometers [34]. Figure 4.38C shows an apparent underestimation of low WS (0-10m/s) and an overestimation of the higher WS values (10-20m/s), although the sample size is not as large for the higher WS. Figure 4.39 shows that for the WS, the location with the best agreement with altimeter data in terms of the correlation coefficient is the open ocean buoy 44066 (higher than 0.95), and the worst is the sheltered buoy 44039 (almost 0.9) located in the Long Island Sound.

Considering the expected differences [67] and results from similar studies [88, 103], altimeter SWH is consistent with the buoy observations. The comparison also showcases the strength of SARAL-AltiKa in coastal regions due to its higher resolution and lower noise in the observations [6, 10]. Validation of altimeter WS with the available buoys in SNE is more challenging due to the relatively small sample size and the sampling radius. However, the overall statistics show good agreement between the two data sources. Although studies related to the altimeter WS algorithms [1, 41, 57] define the ocean surface WS as the WS at 10 meters height, the buoy measurements were not adjusted. The adjustment, assuming neutral boundary layer stability, induced systematic biases, and worse overall performance regarding the statistics.

4.7   Wind and Wave maps based on satellite altimeter data

In the previous section, we evaluated each altimeter's performance with respect to in situ observations and their collective dataset with increasing distance to the coast. This section attempts to utilize altimeter data and the methodology described in 3.3 to create maps of the surface WS and the SWH in the SNE region for the winter and summer seasons. One goal is to estimate the WS and SWH in unobserved locations by interpolating the altimeter observations to a regular grid. The selected $0.125° \times 0.125°$ grid is consistent with the distance between altimeter observations on each track (6-7 kilometers) and the altimeter's effective footprint (2-7 kilometers). We selected data from 2019 primarily because it is the first year with data available from all five altimeters, Jason 3, Sentinel 3 A and B, SARAL-AltiKa, and Cryosat 2. Therefore, we filled spatial gaps by adding as many neighboring observations as possible. One disadvantage of the buoys' fixed point locations is that we cannot make assumptions of the geophysical parameters' transition between each station or how the observations are correlated from point location to another. It is neither feasible to have a dense network of in situ stations. Besides, only CDIP buoy 44097 is located inside the offshore wind projected areas. Thus, one of the benefits of this section's results is deducing the WS and SWH gradient from the interpolated maps and its uncertainty.

Figure 4.40 is the map of the interpolated WS altimeter observations for the winter (A) and the summer (B) seasons. Grey contour lines have been added to distinguish areas with a 0.5m/s difference, primarily due to the significant WS gradient during winter. Generally, WS increases with increasing distance to the coast due to the sea surface's lower roughness length and the land's decreasing influence on the transition from a coastal area to the open ocean. Besides, we showed in 4.1.1 and 4.1.2 that SNE is characterized by substantial seasonal variability, especially in the open ocean where the difference of the average WS between the summer and winter seasons is over 4m/s. The WS maps show general agreement with this result as most areas present significant seasonal differences. This feature is critical for offshore wind energy because the wind turbines start operating at a cut-in WS of 3-4 m/s, and their rated WS of maximum capacity is between 11 and 16 m/s. However, the altimeter WS maps represent interpolated surface WS values, and the WS values are expected to be higher at the turbine height. The WS maps indicate values between 4 to 6 m/s for the summer and 6 to 10 m/s for the winter season, respectively. During summer 2019, coastal areas and the northeastern part of the region showed the lowest WS values, and the area between $39° - 39.5°$N and $72.5° - 71.5°$W the highest. The region of peak WS during winter is at $40°N$ and $70.5°$W. There are also two high WS regions, one south of the eastern Long Island and the other north of Cape Cod, MA. The lowest WS can be identified close to the New Jersey shores and the Massachusetts Bay and Boston area. The notable WS gradient could be attributed to the local phenomena present during winter and described in 1.2. The case study of an extreme event in 4.5 also showed that the WS is at its highest during the passing of storms. Therefore, when altimeters capture several extreme events, our estimations are sensitive to extreme WS values. The opposite applies if altimeters miss the passing of the storms. On the contrary, slow-moving, high-pressure systems are mostly present during summer over SNE, decreasing the variability between consecutive altimeter tracks. On average, there are two altimeter tracks available every day over SNE. Still, these tracks represent the satellites' passing over specific regions each time, and they do not cover the whole domain. Therefore, our estimations have spatial and temporal limitations.

Figure 4.41 contains the interpolated SWH maps for the 2019 winter (A) and summer (B) seasons. Figure 4.5 showed that generally, there is strong SWH seasonal variability in the region, especially in the open ocean and as we move further offshore. However, the seasonal variability is almost insignificant in areas surrounded by land or islands like the Nantucket sound, mainly due to the relatively low WS seasonal variability and the small

percentage of swell waves reaching the domain. Therefore, the higher gradients of SWH during the winter that are depicted in Figure 4.41A with respect to Figure 4.41B are expected. On average, SWH ranges from 1 meter close to the coast to over 2 meters in distances over 100 kilometers offshore during the winter. During summer, SWH is low in the coastal area north of Cape Cod Bay, and the highest values are estimated at approximately 70°W and 39°N, the same region of peak SWH during winter 2019. Based on the climatological averages available in Tables 4.5 4.6 and the interannual variability Figure 4.8, the interpolation maps overestimate the SWH very close to the coast and in areas where the influence of swell waves is minimized. This result depicts one of the disadvantages of the kriging methodology and interpolation in general. Kriging provides the best linear unbiased prediction based on the modeled variogram. Still, the topography's constraints and, consequently, the coastal wave dynamics in a semi-enclosed area or inside a sound are not considered for the estimations. Therefore, they are biased with substantial deviations from the expected values.
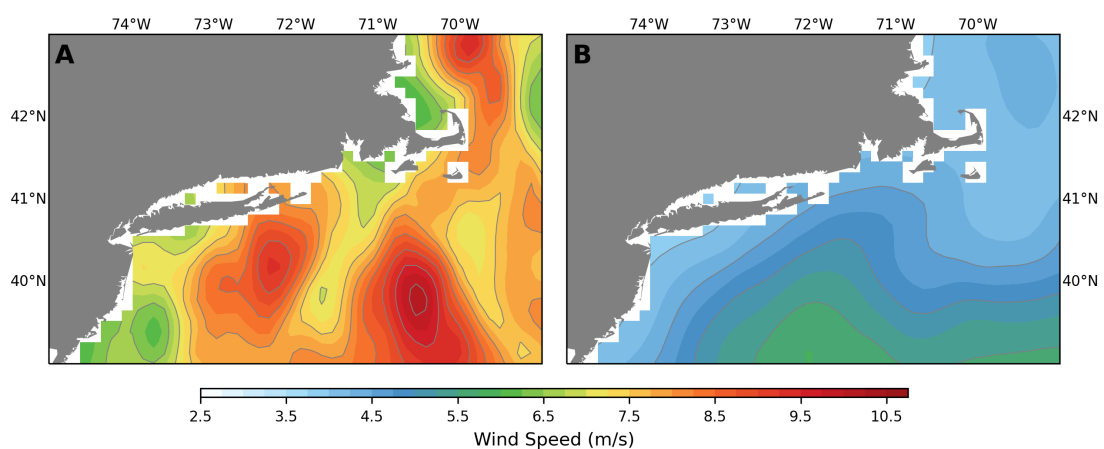
FIGURE 4.40: Surface WS kriging interpolation maps of altimeter data for the 2019 winter (A) and summer (B) seasons.
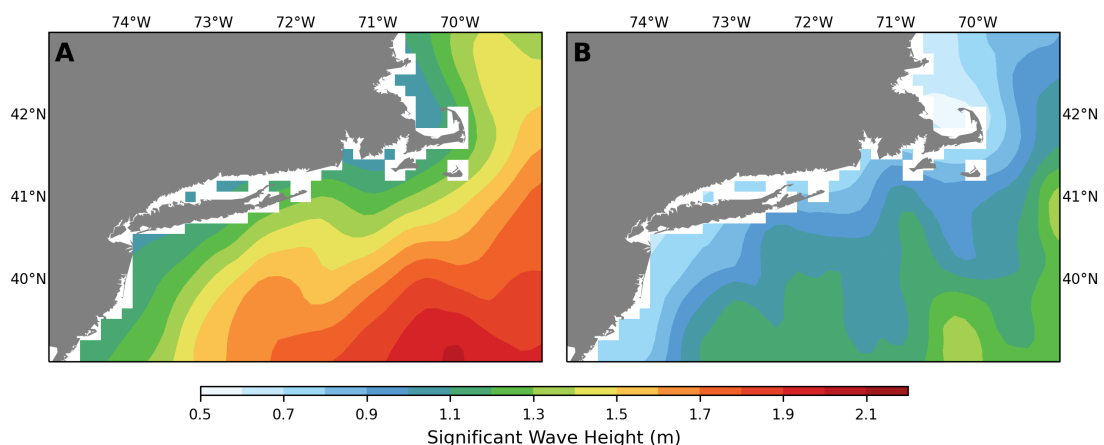
FIGURE 4.41: SWH kriging interpolation maps of altimeter data for the 2019 winter (A) and summer (B) seasons.

There are several types of errors associated with the interpolated WS and SWH maps. First of all, as explained in 3.3, one of the advantages of kriging is that for every estimated value at each grid point, we also estimate the corresponding kriging variance. The variance's square root is the kriging standard error, and it represents the uncertainty of the kriging

interpolation. Figure 4.42 showcases the improvement of the SWH kriging standard error for the winter 2019 season once we include from only one to all five altimeters. The interpolation error becomes smaller even in locations with very few observations, like the southwest and close to the coast, and almost homogeneous to the whole domain when including data from all altimeters. The kriging standard error is smaller than the real estimation errors because other inherent sources of uncertainty are not considered. The second type of error is associated with the initial estimation of the Level 2 altimeter data. Specifically, every altimeter parameter that is derived from the retracking as explained in 2.6 has a corresponding error which is not included in the interpolation.
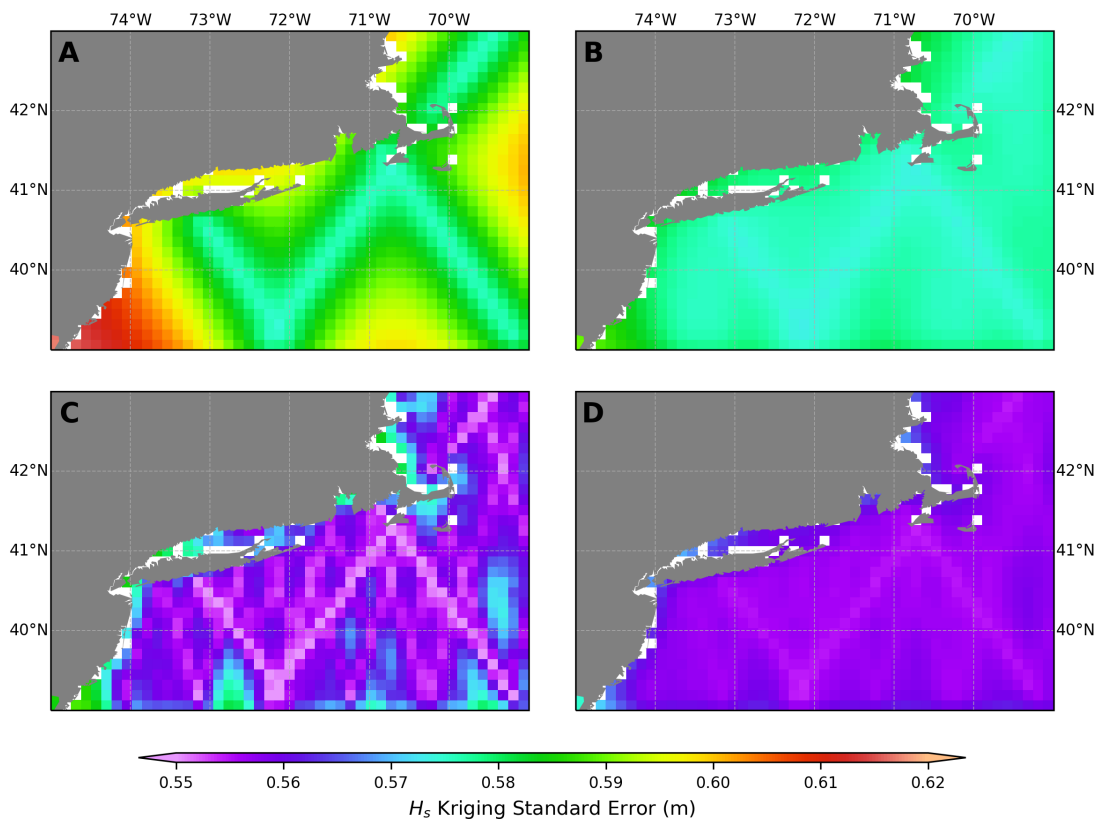
FIGURE 4.42: SWH kriging standard error maps for the 2019 winter using data from (A) Jason 3, (B) Jason 3 and SARAL-AltiKa, (C) Jason 3, SARAL-AltiKa and Sentinel 3 and (D) all altimeters.

The diurnal sampling bias [2, 9] also needs to be considered, especially for the WS and consequently, offshore wind energy estimation. In Section 4.1.1, we showed that there is substantial diurnal variability in locations with a distance less than 40 kilometers from the closest coast, based on observations from buoys, which record the WS every 10 minutes. In contrast, satellites generally pass over a region at specific hours during the day. Three of the five altimeters used in this study, SARAL-Altika, Sentinel 3 A and B, pass over SNE at certain hours. These are the hours of the ascending and the descending tracks. Specifically, SARAL-AltiKa's ascending tracks pass at 6:00-6:30 AM and the descending tracks twelve hours later. Sentinel 3 ascending tracks pass at 9:00-9:30 PM and the descending tracks at 11:00-11:30 AM. Jason 3 and Cryosat 2 pass at irregular times over SNE. Indeed, each cycle or subcycle begins one hour later than the previous one.
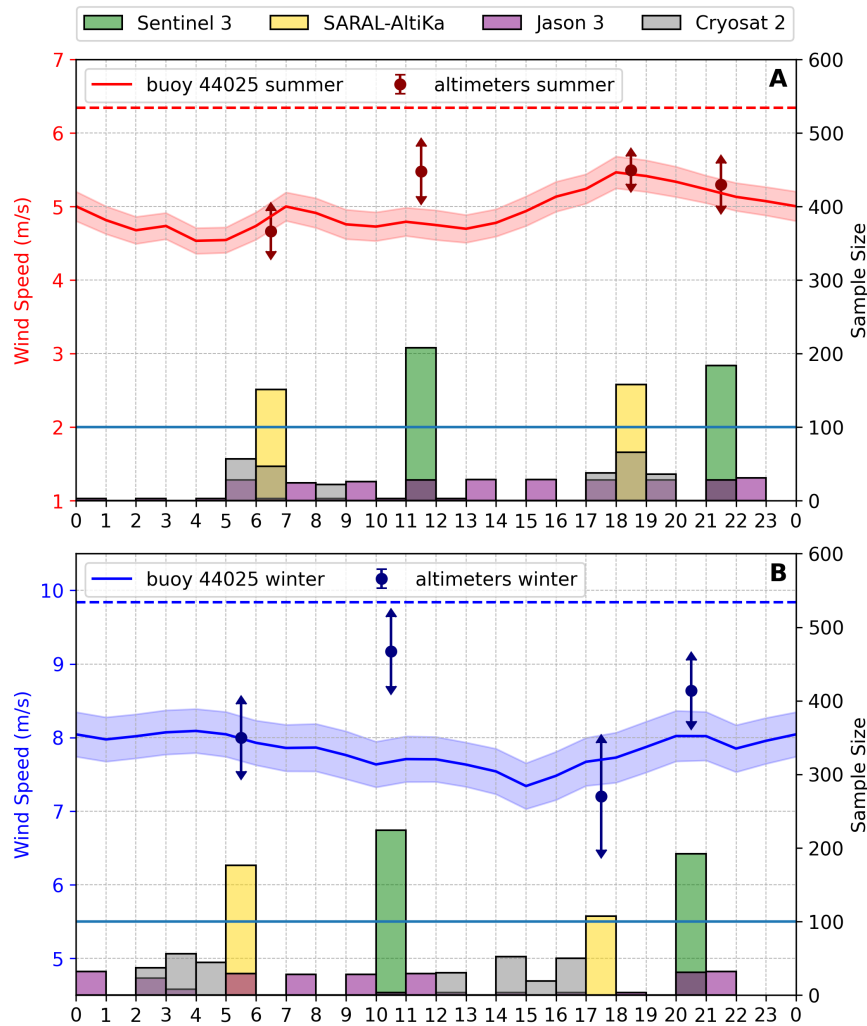
FIGURE 4.43: A visualization of the diurnal bias due to altimeter sampling frequency compared with buoy 44025 for the summer (A) and winter (B) seasons. A straight horizontal blue line was added to display the sample size limit (100) of altimeter observations for the calculation of the average WS value that represents specific hours. The dashed horizontal lines were added to display the minimum available buoy observations for each hour (534).

A summary of this description and comparison with buoy data is presented in Figure 4.43. The histograms represent the altimeter sample size, and a light blue horizontal line is added to visualize the sample size limit for the comparison with buoy observations. We selected a limit of 100 altimeter observations with a maximum distance of 1 degree from buoy 44025. The average and confidence intervals are represented with red dots and arrows for the summer and blue for the winter season. The 1-degree distance is relatively large, but we wanted to have enough observations to compare with over 500 observations per hour from the buoy represented by the blue and red dashed lines. The average WS from altimeters are generally close to the buoy average except for the observations representing the descending Sentinel 3 track. This difference is more significant during winter, and it could be partly attributed to the spatial and temporal limitations previously mentioned. Besides, the SARAL-AltiKa descending track captures the highest WS values at the buoy 44025 location during summer. On the other hand, altimeters' tracks do not coincide with the lowest WS values observed between 5:00 to 6:00 AM by buoy 44025. During winter, both the buoy maximum at 4:00 AM and the minimum WS at 3:00 PM are represented only by a small number of Cryosat

2 and Jason 3 observations. Figure 4.43 is also essential because it depicts the temporal gaps we need to fill with other sensors that measure the WS like scatterometers or SAR to reduce the uncertainty.

Chapter 5

Concluding Remarks and Discussion

Observations are essential to define the wind and wave conditions through all phases of an offshore wind farm, from the design and planning to decommission. They also enhance the quality of the numerical models' initial conditions estimation. In this study, data from buoys and satellite altimeters in the SNE region were used and analyzed.

First, we specified the normal conditions in different scales of variability using the buoy measurements due to their continuous, long-term, and reliable datasets. During the summer season, the surface WS diurnal range can reach up to 2m/s in stations with a distance of 40 kilometers or less from the closest coast. These values are lower than the diurnal range on a meteorological station on land, and the uncertainty is generally higher. The WS diurnal variability also has unique characteristics over the ocean. WS minimum values are identified six hours after the lowest WS on land and the maximum values three to six hours later. The wind direction diurnal cycle has similar patterns for the on land and offshore stations, with a lower diurnal range during the summer season for the coastal buoys. All the above do not apply for stations located over 100 kilometers off the coast, where the diurnal variability is insignificant.

SNE, a mid-latitude North Atlantic coastal region, is characterized by substantial WS and SWH seasonal variability. On the one hand, it ranges from 2m/s for the locations close to the coast to almost 4.5 m/s for the open ocean buoys. The SWH seasonal variability is negligible in areas with proximity to land and a low presence of swell waves. In contrast, it increases with distance to the coast, and it reaches up to 1.5 meters for the open ocean buoys. This difference is only partly explained by the direct influence of the wind on the sea surface. Wind roses sufficiently visualize the directional wind distribution. Generally, the wind has a west or northwest direction during the winter, while it comes from the west or southwest during the summer months. Directional wave distribution does not show the same homogeneity, especially during the winter months when higher wind speeds, storms, and swells with higher energy density are present. The directional wave spectrum of buoy 44097, located on the eastern side of SNE, reveals that the highest monthly average energy density is attributed to waves that arrive from remote regions in the Atlantic Ocean. We can also identify three systems developing throughout the year. The southeastern swell, which has energy density peaks in November and March, is the most dominant. The results indicate the importance of the directional wave spectrum for studying and monitoring the wave conditions in the SNE. Directional spectra observations can also be derived from SAR and satellite missions focused on wind and waves (CFOSAT) and assimilated into numerical models to correct their initial conditions. Therefore, the reconstruction of the directional spectrum of waves from wave buoys or NDBC stations, when available, can serve as a ground truth reference for future studies involving remote sensing observations and the evaluation of numerical models.

The relatively small number of available years of data for most buoys and the gaps in their time-series record were limiting factors for detecting statistically significant WS and SWH trends in SNE. Studies on general or extreme WS and SWH trends using in situ, remote

sensing observations, and data from models show inconsistent or inconclusive results [101] for the Eastern US coasts. On the other hand, the increased storm frequency and intensity in coastal regions like SNE indicate the need for further investigation.

Extreme events are also critical for offshore wind energy yield estimation and fatigue assessment on the infrastructure. Therefore, the wind and wave conditions before, during, and after the passing of a nor'easter storm are examined as a case study.

The relationships between u_{10} and H_s are calculated with polynomial regression fitting to the buoy observations for each of the primary wind directions. The relationships can adequately represent the wind and wave conditions in areas where the wind influence prevails, like the Nantucket Sound, but they are insufficient in swell-dominated locations. For this reason, the wind-wave coupling was further examined using the inverse wave age criterion that considers the wave celerity with respect to u_{10}. This process results in the classification of waves based on their growth, and its advantage is the inclusion of the wind and mean wave direction. The classification shows that at the coastal buoys' locations, especially on the western side of the SNE region, the wave conditions are influenced by the wind, notably during the winter. Still, there is also a substantial presence of swell waves, which is increased during the summer months due to the decreasing wind speed. 70% of the observations at the sheltered buoy 44020 location consist of purely wind waves, while at the open ocean buoy 44008, the sea state is swell-dominated with 95% mixed and swell waves during the summer. We need to emphasize that relationships and classifications have their limitations, primarily because they consider only the wave spectrum's peak. A complete way to observe the sea state is by considering the whole directional wave spectrum, if available.

The accurate estimation of the WS PDF and its parameters is crucial for the offshore wind energy assessment. Specifically, the shape and scale parameters of the distribution are included in calculating the wind power output. The Weibull distribution is the most commonly used and proposed as the best fit to the WS data in similar studies. After fitting the data from four buoys located less than 40 kilometers offshore to a collection of 90 distributions and evaluating the results visually with the probability plots and quantitatively with error statistics, we suggest that the Johnson S_B and the Beta distributions generally have exceptional performance. Only data from the sheltered buoy 44020 fit best to the Weibull 3P. The limitation of such estimations for offshore wind is that the rotor's height is greater than or equal to 100 meters, which is substantially higher than the 10-meter buoy reference height. Future studies using data from offshore towers and lidar buoys in the domain that measure WS and direction at several heights will also expand our knowledge by comparing the results included herein. Besides, even if the distributions mentioned above fit exceptionally the data from buoys in SNE, we need to examine whether mixed distribution models proposed in similar studies [68] improve our estimations.

Satellite altimetry is also an essential source of offshore wind data due to SWH and WS observations' availability to characterize both the sea state and the surface wind regime. Validation of altimeter WS and SWH against in situ observations is required to assure the quality and determine the measurements' accuracy. Although SNE is a relatively small domain with a limited number of available stations, the agreement between the collocated altimeter and buoys dataset is confirmed. The consistency is highlighted by correlation coefficient maps showing high values (over 0.9) at each buoy location to compare using the collective altimeter dataset and an increasing trend with increasing distance from the land. The results verify the exceptional performance of SARAL-AltiKa close to the coast and its ability to provide reliable measurements in low sea states.

The accumulated dataset from all five satellite altimeters was used to interpolate the observations using the kriging methodology for the 2019 winter and summer seasons. The resulting maps show strong WS gradients during winter in SNE, and further investigation is needed to assess the sensitivity of the output maps to extreme events. SWH maps show

coherency during winter and summer with the highest sea states at the southeastern part of the region and decreasing SWH with increasing proximity to the land. Although the availability of SWH and WS in locations close to the coast or areas surrounded by land is one of the advantages, the estimation is not as robust as in the open ocean due to the smaller sample size and the limitations induced by topography. The various sources of errors in the estimation are documented, emphasizing the WS diurnal or sampling bias. Monitoring of the sea state and surface wind conditions requires multiple sources of data, and combined satellite datasets are analyzed in recent studies [48]. The requirement to fill the temporal gaps of the satellite altimeter observations in future studies is addressed.

Bibliography

[1] S. Abdalla. "Ku-Band Radar Altimeter Surface Wind Speed Algorithm". In: *Marine Geodesy* 35.sup1 (Dec. 2012), pp. 276–298. ISSN: 0149-0419. DOI: 10.1080/01490419.2012.718676.

[2] Tobias Ahsbahs et al. "US East Coast synthetic aperture radar wind atlas for offshore wind energy". In: *Wind Energy Science* 5.3 (Sept. 2020), pp. 1191–1210. ISSN: 2366-7451. DOI: 10.5194/wes-5-1191-2020.

[3] Edgar L. Andreas, Larry Mahrt, and Dean Vickers. "A New Drag Relation for Aerodynamically Rough Flow over the Ocean". In: *Journal of the Atmospheric Sciences* 69.8 (Aug. 2012), pp. 2520–2537. ISSN: 0022-4928. DOI: 10.1175/JAS-D-11-0312.1.

[4] Edgar L. Andreas and Sinny Wang. "Predicting significant wave height off the northeast coast of the United States". In: *Ocean Engineering* 34.8-9 (2007), pp. 1328–1335. ISSN: 00298018. DOI: 10.1016/j.oceaneng.2006.08.004.

[5] F. Ardhuin. "Ocean waves in geosciences". In: (2019), p. 277. ISSN: 00445851. DOI: 10.13140/RG.2.2.16019.78888/5.

[6] Fabrice Ardhuin et al. "Observing sea states". In: *Frontiers in Marine Science* 6.APR (2019), pp. 1–29. ISSN: 22967745. DOI: 10.3389/fmars.2019.00124.

[7] G A Athanassoulis and Ch N Stefanakos. "A nonstationary stochastic model for long-term time series of significant wave height". In: *Journal of Geophysical Research* 100.C8 (1995), p. 16149. ISSN: 0148-0227. DOI: 10.1029/94JC01022.

[8] B.H. Bailey. "Wind resources for offshore wind farms". In: *Offshore Wind Farms*. Elsevier, 2016, pp. 29–58. ISBN: 9780081007792. DOI: 10.1016/B978-0-08-100779-2.00003-9.

[9] R. J. Barthelmie and S. C. Pryor. "Can satellite sampling of offshore wind speeds realistically represent wind speed distributions?" In: *Journal of Applied Meteorology* (2003). ISSN: 08948763. DOI: 10.1175/1520-0450(2003)042<0083:CSSOOW>2.0.CO;2.

[10] Pascal Bonnefond et al. "The benefits of the Ka-band as evidenced from the SARAL/AltiKa altimetric mission: Quality assessment and unique characteristics of AltiKa data". In: *Remote Sensing* 10.1 (2018). ISSN: 20724292. DOI: 10.3390/rs10010083.

[11] E. Bronner, A. Guillot, and N Picot. *SARAL / AltiKa Products Handbook*. Tech. rep. 2013, p. 76. URL: https://www.aviso.altimetry.fr/fileadmin/documents/data/tools/SARAL_Altika_products_handbook.pdf.

[12] Gary S. Brown. "The Average Impulse Response of a Rough Surface and Its Applications". In: *IEEE Journal of Oceanic Engineering* 2.1 (1977), pp. 67–74. ISSN: 15581691. DOI: 10.1109/JOE.1977.1145328.

[13] Kyra Bryant and Muhammad Akbar. "An Exploration of Wind Stress Calculation Techniques in Hurricane Storm Surge Modeling". In: *Journal of Marine Science and Engineering* 4.3 (Sept. 2016), p. 58. ISSN: 2077-1312. DOI: 10.3390/jmse4030058.

[14] D. J.T. Carter. "Prediction of wave height and period for a constant wind velocity using the JONSWAP results". In: *Ocean Engineering* (1982). ISSN: 00298018. DOI: 10.1016/0029-8018(82)90042-7.

[15] Dudley B. Chelton et al. "Satellite Altimetry". In: *Satellite Altimetry and Earth Sciences: A Handbook of Techniques and Applications*. Elsevier, 2001. Chap. 1, pp. 1–131. DOI: 10.1016/S0074-6142(01)80146-7.

[16] Ge Chen et al. "A global view of swell and wind sea climate in the ocean by satellite altimeter and scatterometer". In: *Journal of Atmospheric and Oceanic Technology* (2002). ISSN: 07390572. DOI: 10.1175/1520-0426(2002)019<1849:AGVOSA>2.0.CO;2.

[17] Charles Cox and Walter Munk. "Measurement of the Roughness of the Sea Surface from Photographs of the Sun's Glitter". In: *Journal of the Optical Society of America* 44.11 (1954), p. 838. ISSN: 0030-3941. DOI: 10.1364/josa.44.000838.

[18] Noel Cressie and Douglas M. Hawkins. "Robust estimation of the variogram: I". In: *Journal of the International Association for Mathematical Geology* 12.2 (Apr. 1980), pp. 115–125. ISSN: 0020-5958. DOI: 10.1007/BF01035243.

[19] G. T. Csanady. "Wind Waves and the Mechanisms of Air-Sea Transfer". In: *Air-Sea Interaction*. Cambridge University Press, Mar. 2001, pp. 51–96. ISBN: 9780521796804. DOI: 10.1017/CBO9781139164672.002.

[20] Robert G. Dean and Robert A. Dalrymple. "Wave Statistics and Spectra". In: *Water Wave Mechanics for Engineers and Scientists*. World Scientific, Jan. 1991. Chap. 7, pp. 187–211. DOI: 10.1142/9789812385512{_}0007.

[21] Gérald Dibarboure et al. "The drifting phase of SARAL: Securing stable ocean mesoscale sampling with an unmaintained decaying altitude". In: *Remote Sensing* 10.7 (2018), pp. 1–21. ISSN: 20724292. DOI: 10.3390/rs10071051.

[22] DNVGL. *Metocean Characterization Recommended Practices for U. S. Offshore Wind Energy*. Tech. rep. August. 2018. URL: https://www.boem.gov/sites/default/files/environmental-stewardship/Environmental-Studies/Renewable-Energy/Metocean-Recommended-Practices.pdf.

[23] R DOLAN and R. DAVIS. "An intensity scale for Atlantic Coast northeast storms". In: *Journal of Coastal Research* (1992). ISSN: 0749-0208.

[24] C. Douglas and G. Voulgaris. *WavePart v1.1, MATLAB(r) scripts for the partition of 2-D ocean wave spectra and identification of swell and wind wave trains*. 2019. DOI: 10.5281/zenodo.3495817.

[25] P. A. Dowd. "The Variogram and Kriging: Robust and Resistant Estimators". In: *Geostatistics for Natural Resources Characterization*. Dordrecht: Springer Netherlands, 1984, pp. 91–106. DOI: 10.1007/978-94-009-3699-7{_}6. URL: http://link.springer.com/10.1007/978-94-009-3699-7_6.

[26] Tom H. Durrant, Diana J.M. Greenslade, and Ian Simmonds. "Validation of Jason-1 and Envisat remotely sensed wave heights". In: *Journal of Atmospheric and Oceanic Technology* 26.1 (2009), pp. 123–134. ISSN: 07390572. DOI: 10.1175/2008JTECHO598.1.

[27] M D Earle. *Nondirectional and Directional Wave Data Analysis Procedures. NDBC Technical Document 96-01*. Tech. rep. January. National Data Buoy Center, 1996. URL: https://www.ndbc.noaa.gov/wavemeas.pdf.

[28] M. D. Earle, K. E. Steele, and D. W.C. Wang. "Use of advanced directional wave spectra analysis methods". In: *Ocean Engineering* 26.12 (1999), pp. 1421–1434. ISSN: 00298018. DOI: 10.1016/S0029-8018(99)00010-4.

[29] James B. Edson et al. "On the exchange of momentum over the open ocean". In: *Journal of Physical Oceanography* 43.8 (2013), pp. 1589–1610. ISSN: 15200485. DOI: 10.1175/JPO-D-12-0173.1.

[30] Stefan Emeis. *Wind Energy Meteorology*. Green Energy and Technology. Cham: Springer International Publishing, 2018, p. 255. ISBN: 978-3-319-72858-2. DOI: 10.1007/978-3-319-72859-9.

[31] ESA. *CryoSat-2 Product Handbook*. Tech. rep. 2019, p. 58. URL: https://earth.esa.int/documents/10174/125272/CryoSat-Baseline-D-Product-Handbook.

[32] EUMETSAT. *Sentinel-3 SRAL Marine User Handbook*. Tech. rep. 2017, p. 55. URL: https://earth.esa.int/eogateway/documents/20142/1564943/Sentinel-3-SRAL-Marine-User-Handbook.pdf.

[33] Eduardo G. G. de Farias, João A. Lorenzzetti, and Bertrand Chapron. "Swell and Wind-Sea Distributions over the Mid-Latitude and Tropical North Atlantic for the Period 2002–2008". In: *International Journal of Oceanography* 2012 (2012), pp. 1–8. ISSN: 1687-9406. DOI: 10.1155/2012/306723.

[34] J. Figa-Saldaña et al. "The advanced scatterometer (ascat) on the meteorological operational (MetOp) platform: A follow on for european wind scatterometers". In: *Canadian Journal of Remote Sensing* (2002). ISSN: 17127971. DOI: 10.5589/m02-035.

[35] Marc G. Genton. "Highly Robust Variogram Estimation". In: *Mathematical Geology* (1998). ISSN: 08828121. DOI: 10.1023/A:1021728614555.

[36] David B. Gilhousen and Rex Hervey. "Improved estimates of swell from moored buoys". In: *Proceedings of the International Symposium on Ocean Wave Measurement and Analysis* 1.2001 (2001), pp. 387–393. DOI: 10.1061/40604(273)40.

[37] Roman E. Glazman and Stuart H. Pilorz. "Effects of sea maturity on satellite altimeter measurements". In: *Journal of Geophysical Research* 95.C3 (1990), p. 2857. ISSN: 0148-0227. DOI: 10.1029/JC095iC03p02857.

[38] Yoshimi Goda. "Description of Random Sea Waves". In: *Random Seas and Design of Maritime Structures*. 3rd. World Scientific, June 2010. Chap. 8, pp. 357–368. ISBN: 978-981-3101-02-9. DOI: 10.1142/9789814282413{_}0009.

[39] Yoshimi Goda. "Techniques of Irregular Wave Analysis". In: *Random Seas and Design of Maritime Structures*. 3rd. World Scientific, June 2010. Chap. 10, pp. 433–489. DOI: 10.1142/9789814282413{_}0011.

[40] C. Gommenginger et al. "Retracking Altimeter Waveforms Near the Coasts". In: *Coastal Altimetry*. Ed. by Stefano Vignudelli et al. Berlin, Heidelberg: Springer Berlin Heidelberg, 2011, pp. 61–101. ISBN: 978-3-642-12795-3. DOI: 10.1007/978-3-642-12796-0{_}4.

[41] J. Gourrion et al. "A two-parameter wind speed algorithm for Ku-band altimeters". In: *Journal of Atmospheric and Oceanic Technology* 19.12 (2002), pp. 2030–2048. ISSN: 07390572. DOI: 10.1175/1520-0426(2002)019<2030:ATPWSA>2.0.CO;2.

[42] A. A. Grachev and C. W. Fairall. "Upward Momentum Transfer in the Marine Boundary Layer". In: *Journal of Physical Oceanography* 31.7 (July 2001), pp. 1698–1711. ISSN: 0022-3670. DOI: 10.1175/1520-0485(2001)031<1698:UMTITM>2.0.CO;2.

[43] Abderrahim Halimi et al. "Parameter estimation for peaky altimetric waveforms". In: *IEEE Transactions on Geoscience and Remote Sensing* 51.3 (2013), pp. 1568–1577. ISSN: 01962892. DOI: 10.1109/TGRS.2012.2205697.

[44] Kirsty E. Hanley and Stephen E. Belcher. "Wave-Driven Wind Jets in the Marine Atmospheric Boundary Layer". In: *Journal of the Atmospheric Sciences* 65.8 (Aug. 2008), pp. 2646–2660. ISSN: 1520-0469. DOI: 10.1175/2007JAS2562.1.

[45] Kirsty E. Hanley, Stephen E. Belcher, and Peter P. Sullivan. "A Global climatology of wind-wave interaction". In: *Journal of Physical Oceanography* 40.6 (2010), pp. 1263–1282. ISSN: 00223670. DOI: 10.1175/2010JPO4377.1.

[46] J. L. Hanson and O. M. Phillips. "Automated analysis of ocean surface directional wave spectra". In: *Journal of Atmospheric and Oceanic Technology* 18.2 (2001), pp. 277–293. ISSN: 07390572. DOI: 10.1175/1520-0426(2001)018<0277:AAOOSD>2.0.CO;2.

[47] Charles R. Harris et al. "Array programming with NumPy". In: *Nature* 585.7825 (2020), pp. 357–362. ISSN: 14764687. DOI: 10.1038/s41586-020-2649-2.

[48] Charlotte B. Hasager et al. "Offshore wind climatology based on synergetic use of Envisat ASAR, ASCAT and QuikSCAT". In: *Remote Sensing of Environment* (2015). ISSN: 00344257. DOI: 10.1016/j.rse.2014.09.030.

[49] K. Hasselmann et al. "Measurements of wind-wave growth and swell decay during the joint North Sea wave project (JONSWAP)." In: July 2015 (1973).

[50] George S. Hayne. "Radar Altimeter Mean Return Waveforms from Near-Normal-Incidence Ocean Surface Scattering". In: *IEEE Transactions on Antennas and Propagation* 28.5 (1980), pp. 687–692. ISSN: 15582221. DOI: 10.1109/TAP.1980.1142398.

[51] Stephan Hoyer and Joseph J. Hamman. "xarray: N-D labeled Arrays and Datasets in Python". In: *Journal of Open Research Software* 5 (2017), pp. 1–6. ISSN: 2049-9647. DOI: 10.5334/jors.148.

[52] S. A. Hsu, Eric A. Meindl, and David B. Gilhousen. "Determining the Power-Law Wind-Profile Exponent under Near-Neutral Stability Conditions at Sea". In: *Journal of Applied Meteorology* 33.6 (June 1994), pp. 757–765. ISSN: 0894-8763. DOI: 10.1175/1520-0450(1994)033<0757:DTPLWP>2.0.CO;2.

[53] Md. Hussain and Ishtiak Mahmud. "pyMannKendall: a python package for non parametric Mann Kendall family of trend tests." In: *Journal of Open Source Software* 4.39 (July 2019), p. 1556. ISSN: 2475-9066. DOI: 10.21105/joss.01556.

[54] Paul A. Hwang et al. "A statistical comparison of wind speed, wave height, and wave period derived from satellite altimeters and ocean buoys in the Gulf of Mexico region". In: *Journal of Geophysical Research: Oceans* 103.C5 (1998), pp. 10451–10468. ISSN: 21699291. DOI: 10.1029/98jc00197.

[55] International Eletrotechnical Commision. *Wind Turbines - Part 1: Design requirements*. Tech. rep. 2019, p. 349. URL: https://webstore.iec.ch/publication/26423.

[56] A. J. Kuik, G. Ph van Vledder, and L. H. Holthuijsen. *A Method for the Routine Analysis of Pitch-and-Roll Buoy Wave Data*. 1988. DOI: 10.1175/1520-0485(1988)018<1020:amftra>2.0.co;2.

[57] John Lillibridge et al. "One-and two-dimensional wind speed models for ka-band altimetry". In: *Journal of Atmospheric and Oceanic Technology* 31.3 (2014), pp. 630–638. ISSN: 15200426. DOI: 10.1175/JTECH-D-13-00167.1.

[58] W. Timothy Liu, Kristina B. Katsaros, and Joost A. Businger. "Bulk Parameterization of Air-Sea Exchanges of Heat and Water Vapor Including the Molecular Constraints at the Interface". In: *Journal of the Atmospheric Sciences* 36.9 (Sept. 1979), pp. 1722–1735. ISSN: 0022-4928. DOI: 10.1175/1520-0469(1979)036<1722:BPOASE>2.0.CO;2.

[59] W. Timothy Liu and Xiaosu Xie. "Sea Surface Wind/Stress Vector". In: ed. by Eni G. Njoku. Encyclopedia of Earth Sciences Series. New York, NY: Springer New York, 2014, pp. 759–767. ISBN: 978-0-387-36698-2. DOI: 10.1007/978-0-387-36699-9{_}168.

[60] Alexander Loew et al. "Validation practices for satellite-based Earth observation data across communities". In: *Reviews of Geophysics* 55.3 (2017), pp. 779–817. ISSN: 19449208. DOI: 10.1002/2017RG000562.

[61] M. S. Longuet-Higgins, D. E. Cartwright, and N. D. Smith. "Observations of the directional spectrum of sea waves using the motions of a floating buoy". In: *Ocean Wave Spectra*. Prentice-Hall, Inc., Englewood Cliffs, N. J., 1963, pp. 111–136.

[62] Asle Lygre and Harald E. Krogstad. "Maximum Entropy Estimation of the Directional Distribution in Ocean Wave Spectra". In: *Journal of Physical Oceanography* 16.12 (Dec. 1986), pp. 2052–2060. ISSN: 0022-3670. DOI: 10.1175/1520-0485(1986)016<2052:MEEOTD>2.0.CO;2.

[63] Mirko Mälicke, Helge David Schneider, and Codacy Badger. *mmaelicke/scikit-gstat: Version 0.3*. 2020. DOI: 10.5281/zenodo.4065199.

[64] Wes McKinney. "Data Structures for Statistical Computing in Python". In: *Proceedings of the 9th Python in Science Conference* 1697900.Scipy (2010), pp. 51–56. ISSN: 0440877763224. URL: http://conference.scipy.org/proceedings/scipy2010/mckinney.html.

[65] F. Mertz, J. P. Dumont, and S. Urien. *Baseline-C CryoSat Ocean Processor*. Tech. rep. 2017, p. 54. URL: https://earth.esa.int/documents/10174/125272/CryoSat-Baseline-C-Ocean-Product-Handbook.

[66] Alberto Meucci et al. "Comparison of wind speed and wave height trends from twentieth-century models and satellite altimeters". In: *Journal of Climate* 33.2 (2020), pp. 611–624. ISSN: 08948755. DOI: 10.1175/JCLI-D-19-0540.1.

[67] F. Monaldo. "Expected differences between buoy and radar altimeter estimates of wind speed and significant wave height and their implications on buoy-altimeter comparisons". In: *Journal of Geophysical Research* 93.C3 (1988), pp. 2285–2302. ISSN: 01480227. DOI: 10.1029/JC093iC03p02285.

[68] Eugene C. Morgan et al. "Probability distributions for offshore wind speeds". In: *Energy Conversion and Management* 52.1 (2011), pp. 15–26. ISSN: 01968904. DOI: 10.1016/j.enconman.2010.06.015.

[69] Walter H. Munk. "ORIGIN AND GENERATION OF WAVES". In: *Coastal Engineering Proceedings* 1.1 (May 2010), p. 1. ISSN: 2156-1028. DOI: 10.9753/icce.v1.1.

[70] Benjamin Murphy, Sebastian Müller, and Roman Yurchak. *GeoStat-Framework/PyKrige v1.5.1*. 2020. DOI: 10.5281/zenodo.3991907.

[71] National Data Buoy Center. *Handbook of Automated Data Quality Control Checks and Procedures*. Tech. rep. August. 2009, pp. 1–78. URL: http://www.ndbc.noaa.gov/NDBCHandbookofAutomatedDataQualityControl2009.pdf.

[72] National Research Council. *The Meteorological Buoy and Coastal Marine Automated Network for the United States*. 17. Washington, D.C.: National Academies Press, Nov. 1998. ISBN: 978-0-309-06088-2. DOI: 10.17226/6108.

[73] Simon P. Neill and M. Reza Hashemi. "Offshore Wind". In: *Fundamentals of Ocean Renewable Energy*. Elsevier, 2018, pp. 83–106. DOI: 10.1016/B978-0-12-810448-4.00004-5.

[74] Francesco Nencioli and Graham D. Quartly. "Evaluation of Sentinel-3A wave height observations near the coast of southwest England". In: *Remote Sensing* 11.24 (2019). ISSN: 20724292. DOI: 10.3390/rs11242998.

[75] G. Neumann and W. J. Pierson. "A detailed comparison of theoretical wave spectra and wave forecasting methods". In: *Deutsche Hydrographische Zeitschrift* 10.4 (July 1957), pp. 134–146. ISSN: 0012-0308. DOI: 10.1007/BF02020059.

[76] John W. Nielsen. "The Formation of New England Coastal Fronts". In: *Monthly Weather Review* 117.7 (July 1989), pp. 1380–1401. ISSN: 0027-0644. DOI: 10.1175/1520-0493(1989)117<1380:TFONEC>2.0.CO;2.

[77] World Meteoroligcal Organization. *Guide to Wave Analysis and Forecasting*. Vol. 2018. 702. 2018, pp. 1–210. ISBN: 978-92-63-10702-2. URL: https://library.wmo.int/index.php?lvl=notice_display&id=7700.

[78] N. Picot et al. *Jason-3 Products Handbook*. Tech. rep. 2018. URL: https://www.ospo.noaa.gov/Products/documents/hdbk_j3.pdf.

[79] Willard J. Pierson and Lionel Moskowitz. "A proposed spectral form for fully developed wind seas based on the similarity theory of S. A. Kitaigorodskii". In: *Journal of Geophysical Research* 69.24 (Dec. 1964), pp. 5181–5190. ISSN: 01480227. DOI: 10.1029/JZ069i024p05181.

[80] Willard J. Pierson, G. Neumann, and R.W. James. "Practical methods for observing and forecasting ocean waves by means of wave spectra and statistics". In: *Naval Oceanographic Office Nstl Station Ms.* (1955).

[81] Jesús Portilla, Francisco J. Ocampo-Torres, and Jaak Monbaliu. "Spectral partitioning and identification of wind sea and swell". In: *Journal of Atmospheric and Oceanic Technology* 26.1 (2009), pp. 107–122. ISSN: 07390572. DOI: 10.1175/2008JTECHO609.1.

[82] Pierre Queffeulou. "Long-term validation of wave height measurements from altimeters". In: *Marine Geodesy* 27.3-4 (2004), pp. 495–510. ISSN: 01490419. DOI: 10.1080/01490410490883478.

[83] Keith R. Raney. "The delay/doppler radar altimeter". In: *IEEE Transactions on Geoscience and Remote Sensing* 36.5 PART 1 (1998), pp. 1578–1588. ISSN: 01962892. DOI: 10.1109/36.718861.

[84] Chris Ray et al. "SAR altimeter backscattered waveform model". In: *IEEE Transactions on Geoscience and Remote Sensing* 53.2 (2015), pp. 911–919. ISSN: 01962892. DOI: 10.1109/TGRS.2014.2330423.

[85] M. Raynal et al. "From conventional to Delay Doppler altimetry: A demonstration of continuity and improvements with the Cryosat-2 mission". In: *Advances in Space Research* 62.6 (Sept. 2018), pp. 1564–1575. ISSN: 02731177. DOI: 10.1016/j.asr.2018.01.006.

[86] Agustinus Ribal and Ian R. Young. "33 years of globally calibrated wave height and wind speed data based on altimeter observations". In: *Scientific Data* 6.1 (Dec. 2019), p. 77. ISSN: 2052-4463. DOI: 10.1038/s41597-019-0083-9.

[87] Ian S. Robinson. "Ocean surface waves". In: *Discovering the Ocean from Space*. Berlin, Heidelberg: Springer Berlin Heidelberg, 2010, pp. 293–332. DOI: 10.1007/978-3-540-68322-3{_}8.

[88] Hector Hito Sepulveda, Pierre Queffeulou, and Fabrice Ardhuin. "Assessment of SARAL/AltiKa Wave Height Measurements Relative to Buoy, Jason-2, and Cryosat-2 Data". In: *Marine Geodesy* 38 (2015), pp. 449–465. ISSN: 1521060X. DOI: 10.1080/01490419.2014.1000470.

[89] Stuart D. Smith. "Coefficients for sea surface wind stress, heat flux, and wind profiles as a function of wind speed and temperature". In: *Journal of Geophysical Research* 93.C12 (1988), p. 15467. ISSN: 0148-0227. DOI: 10.1029/JC093iC12p15467.

[90] Takvor Soukissian. "Use of multi-parameter distributions for offshore wind speed modeling: The Johnson SB distribution". In: *Applied Energy* 111 (Nov. 2013), pp. 982–1000. ISSN: 03062619. DOI: 10.1016/j.apenergy.2013.06.050.

[91] Takvor H. Soukissian. "Probabilistic modeling of directional and linear characteristics of wind and sea states". In: *Ocean Engineering* 91 (Nov. 2014), pp. 91–110. ISSN: 00298018. DOI: 10.1016/j.oceaneng.2014.08.018.

[92] K.E. Steele et al. "Buoy pitch and roll computed using three angular rate sensors". In: *Coastal Engineering* 35.1-2 (Oct. 1998), pp. 123–139. ISSN: 03783839. DOI: 10.1016/S0378-3839(98)00025-8.

[93] Peter K. Taylor and Margaret J. Yelland. "The Dependence of Sea Surface Roughness on the Height and Steepness of the Waves". In: *Journal of Physical Oceanography* 31.2 (2001), pp. 572–590. ISSN: 0022-3670. DOI: 10.1175/1520-0485(2001)031<0572:TDOSSR>2.0.CO;2.

[94] The WAVEWATCH Development Group (WW3DG). *User manual and system documentation of WAVEWATCH III R version 6.07*. Tech. rep. 2019. URL: https://github.com/NOAA-EMC/WW3/wiki/Manual.

[95] B. W. Timmermans et al. "Global Wave Height Trends and Variability from New Multimission Satellite Altimeter Products, Reanalyses, and Wave Buoys". In: *Geophysical Research Letters* 47.9 (2020). ISSN: 19448007. DOI: 10.1029/2019GL086880.

[96] Jean Tournadre, Juliette Lambin-Artru, and Nathalie Steunou. "Cloud and rain effects on AltiKa/SARAL ka-band radar altimeter-part I: Modeling and mean annual data availability". In: *IEEE Transactions on Geoscience and Remote Sensing* 47.6 (2009), pp. 1806–1817. ISSN: 01962892. DOI: 10.1109/TGRS.2008.2010130.

[97] Martin H. Trauth. "Spatial Data". In: *MATLAB® Recipes for Earth Sciences*. Berlin, Heidelberg: Springer Berlin Heidelberg, 2006, pp. 151–192. DOI: 10.1007/3-540-27984-9{_}7.

[98] G. Varoquaux et al. "Scikit-learn: Machine Learning in Python". In: *Journal of Machine Learning Research* 19.1 (2015), pp. 29–33. ISSN: 2375-0529. DOI: 10.1145/2786984.2786995.

[99] Jacques Verron et al. "The SARAL/AltiKa Altimetry Satellite Mission". In: *Marine Geodesy* 38.sup1 (Sept. 2015), pp. 2–21. ISSN: 0149-0419. DOI: 10.1080/01490419.2014.1000471.

[100] Pauli Virtanen et al. "SciPy 1.0: fundamental algorithms for scientific computing in Python". In: *Nature Methods* 17.3 (2020), pp. 261–272. ISSN: 15487105. DOI: 10.1038/s41592-019-0686-2.

[101] Russell S. Vose et al. "Monitoring and Understanding Changes in Extremes: Extratropical Storms, Winds, and Waves". In: *Bulletin of the American Meteorological Society* 95.3 (Mar. 2014), pp. 377–386. ISSN: 1520-0477. DOI: 10.1175/BAMS-D-12-00162.1.

[102] David W. Wang and Paul A. Hwang. "An operational method for separating wind sea and swell from ocean wave spectra". In: *Journal of Atmospheric and Oceanic Technology* 18.12 (2001), pp. 2052–2062. ISSN: 07390572. DOI: 10.1175/1520-0426(2001)018<2052:AOMFSW>2.0.CO;2.

[103] Jungang Yang and Jie Zhang. "Validation of Sentinel-3A/3B satellite altimetry wave heights with buoy and Jason-3 data". In: *Sensors* 19.13 (2019). ISSN: 14248220. DOI: 10.3390/s19132914.

[104]   I.R. Young. "Seasonal variability of the global ocean wind and wave climate". In: *International Journal of Climatology* 19.9 (July 1999), pp. 931–950. ISSN: 0899-8418. DOI: `10.1002/(SICI)1097-0088(199907)19:9<931::AID-JOC412>3.0.CO;2-O`.

[105]   "Fetch and Duration Limited Growth". In: *Wind Generated Ocean Waves*. Ed. by Ian R. Young. 1st. Elsevier, 1999. Chap. 5, pp. 83–131. DOI: `10.1016/S1571-9952(99)80007-5`.

[106]   "Ocean Wave Measurement". In: *Wind Generated Ocean Waves*. Ed. by Ian R. Young. 1st. Elsevier, 1999. Chap. 9, pp. 227–254. ISBN: 978-0-08-043317-2. DOI: `10.1016/S1571-9952(99)80011-7`.

[107]   Ian R. Young, E. Sanina, and A. V. Babanin. "Calibration and cross validation of a global wind and wave database of altimeter, radiometer, and scatterometer measurements". In: *Journal of Atmospheric and Oceanic Technology* 34.6 (2017), pp. 1285–1306. ISSN: 15200426. DOI: `10.1175/JTECH-D-16-0145.1`.

[108]   Dongliang Zhao and Moxin Li. "Dependence of wind stress across an air–sea interface on wave states". In: *Journal of Oceanography* 75.3 (June 2019), pp. 207–223. ISSN: 0916-8370. DOI: `10.1007/s10872-018-0494-9`.

[109]   S. Zieger, J. Vinoth, and I. R. Young. "Joint calibration of multiplatform altimeter measurements of wind speed and wave height over the past 20 Years". In: *Journal of Atmospheric and Oceanic Technology* 26.12 (2009), pp. 2549–2564. ISSN: 07390572. DOI: `10.1175/2009JTECHA1303.1`.